21

The Study of the Damping Characteristics of a Bimetallic Structure for the Design of Silent High-Performance Gears

by

Jung Sin Yi

Bachelor of Science in Mechanical Engineering

Massachusetts Institute of Technology (1996)

Submitted to the Department of Mechanical Engineering in partial fulfillment of the requirements for the degree of

Master of Science in Mechanical Engineering

at the

Massachusetts Institute of Technology

February 1998

© 1998 Massachusetts Institute of Technology
All Rights Reserved.

Author .....
Department of Mechanical Engineering
February 5, 1998

Certified by .....
Professor Z. C. Feng
Thesis Supervisor

Accepted by .....
Professor Ain A. Sonin
Chairman, Department Committee on Graduate Students

APR 27 1998

LIBRARIES

The Study of the Damping Characteristics of a Bimetallic Structure for the Design of Silent High-Performance Gears

by

Jung Sin Yi

Submitted to the Department of Mechanical Engineering
on February 5, 1998, in partial fulfillment of the requirements for the degree of
Master of Science in Mechanical Engineering

Abstract

Competitive pressure in the automobile industry has yielded many studies in improving the vehicle sound quality. As the complexity and the size in transmission gear systems grew, the need for quiet gear train systems has also grown, resulting in numerous research in the reduction of noise/vibration level of gears. The main source of gear noise and vibration is the transmission error, which is mainly caused by imperfect surface finish and geometric errors in gear manufacturing processes. The conventional approach is to reduce this transmission error through precision machining and finishing of gear manufacturing, the cost of which rises exponentially as the level of precision increases. Here we take a different approach by introducing bimetallic structure in gear teeth. Reduction in gear vibration and noise is achieved through increased internal damping due to the material and structural modifications in gear teeth.

As gears mesh, the gear teeth deform under the applied load. When the load is suddenly removed, vibration energy is generated, creating structure-born noise. This vibration of the gears can be reduced if the energy is dissipated by internal damping. To increase internal damping of gear teeth, design modifications are made; slots are machined in gear teeth parallel to the direction of loading and filled with a damping material (i.e., a metal with a low yield stress), which bonds the separated segments of the tooth. Since the gear teeth are not uniformly loaded, the softer damping material in the slots will undergo elastic and plastic deformations and therefore, consume more energy than conventional gears when the gear teeth are engaged. This results in the attenuation of gear noise and vibration.

Therefore, this thesis mainly focuses on the study of understanding the damping characteristics of bimetallic structure. Theoretical cyclic energy loss analysis and empirical findings of larger damping coefficient reveal that the internal damping of the bimetallic structure is higher than the conventional structure. Also two experiments on modified bimetallic gears reveal a small decrease in the vibration and noise level from original conventional gears.

By understanding the damping characteristics of the bimetallic structure, it is possible to make gears with higher internal damping which will induce a decreased level of noise and vibration.

Thesis Supervisor: Thesis Supervisor: Z. C. Feng
Title: Assistant Professor in Mechanical Engineering

Acknowledgment

First of all, I want to thank Prof. Nam Suh for providing financial support for my graduate education at MIT. I also thank Prof. Z Feng, who kindly agreed to be my thesis advisor and helped me in writing this thesis. I also want to acknowledge Mr. Insoo Suh, for his help and contribution to this project in many ways.

I thank Mr. Fredrick Cote in LMP and all the technicians at Pappalardo Laboratory as well as Mr. Dick Fenner for their help in the machining aspect of this project. I thank Ms. Patricia Sampson and Ms. Leslie Regan for their help with the administrative work. I also thank Prof. Alexander Slocum for being a great advisor during my undergraduate years.

I also want to show my appreciation to all of my fellow MIT KGSA members, especially Shinsuk Park, Hyuksang Kwon, Jungmok Bae, Junbeum Kim, and Kondong Phang for their encouragement and advice. I would also like to say thanks to all the brothers of the Delta Chapter of Theta Xi Fraternity. I especially thank Mike Evans for being a great friend and helping me always in many ways. I also want to say thanks to my fellow MIT graduate students, namely, Garauv Rohatgi who is also my pledge brother, Mike Kim, Peter Lee, and Jin Qui. Thanks for your encouragement and help. I wish the best in your studies.

I also thank the pastoral staff and members of New Covenant Presbyterian Church who have spiritually supported and guided me. I also thank my roommates, Hyoseok Yang, Jason Han, Rich Lee, Jimmy Woo, and Tom Kim for their support. I also thank Unhyi Choi for her help in writing this thesis.

My dear uncles, aunts and cousins as well as my dear grandmother also deserve recognition in supporting me to be where I am. Finally, I thank my family who have motivated, empowered, and enabled me to accomplish what I have achieved.

My greatest thankful heart goes to my dear God. Thank you for your blessings, your trials, your tests, and your love. All the glory and honor are Yours. I praise the glorious name of Jesus Christ. Amen.

Table of Contents

List of Figures

List of Tables

Chapter 1

Introduction

1.1 Project Objective

The objective of this project is to design silent high-performance gears, mainly for automobile industry applications. Due to heavy-load and high-speed operating condition in high-performance gears, the effects of gear transmission and profile errors caused by either gear manufacturing processes or by wear during operation are amplified, producing greater vibration and noise than conventional gears. Therefore, the goal of this project is to reduce the vibration and noise level of high-performance gears.

1.2 Project Motivation

Competitive pressure in the automobile industry has yielded many studies in improving the vehicle sound quality. As the quietness of vehicles has been continually improved in recent years [1], the need for quiet gear train systems has become more crucial. Lighter vehicle bodies for higher fuel efficiency provides less noise attenuation for transmission systems. Furthermore, the complexity and size in transmission has grown due to the improvement in its performance qualities, such as automatic transmission or extra gear ratio for manual transmission, raising transmission noise contribution to overall vehicle sound quality.

Numerous efforts have been made to reduce transmission gear noise. The typical approach is to minimize the transmission errors of gears through precision machining with optimized gear parameters and gear tooth profiles, reducing the excitation forces of individual gears. However, even though the gear quality is within manufacturing tolerance and design constraints, the noise level of the gear train is still unacceptable in many cases due to highly sensitive gear train dynamics [2]. Moreover, the manufacturing costs for precision gears with minimum tolerance is extremely high [3], and therefore, different approaches are contemplated for gear noise reduction.

Recent design approaches focus on the modification and improvement of overall gear train system dynamics instead of individual gears. For example, several researchers of Nissan Motor Co. Ltd., adopted a finite element method in analyzing gear train vibration in an attempt to reduce the noise of overall gear train [1]. H. Opitz of the University of Aachen proposed the sound and vibration isolation method by increasing the vibration impedance of gear blanks and gear housings

with damping material as shown in Fig. 1.1 [4]. For this project, however, the attention has been brought back to the dynamics of individual gears in reducing the vibration and noise of gears.

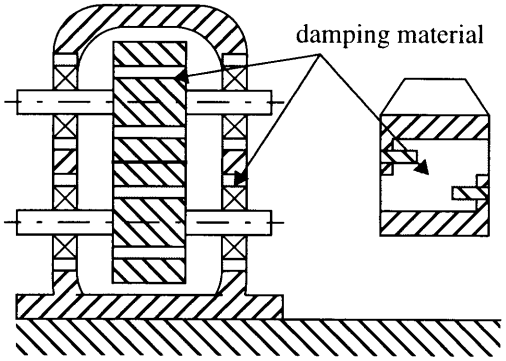

Figure 1.1: Sound and Vibration Isolation Method proposed by H. Opitz [4]

1.3 Project Description

The design concept of this project is to increase the vibration impedance near the source of vibration, at the gear teeth. Naturally, an increase in the vibration impedance in both the gears and their housing will decrease the overall gear noise, but the focus of this project is on individual gears and their teeth.

As gears mesh, the gear teeth deform under the applied load. When the load is applied and suddenly removed, vibration energy is generated, and as it is transmitted to the surrounding structures, structure-born noise is created. This vibration of gear teeth can be reduced if the vibration energy is dissipated by internal damping, decreasing the noise level of the gear system.

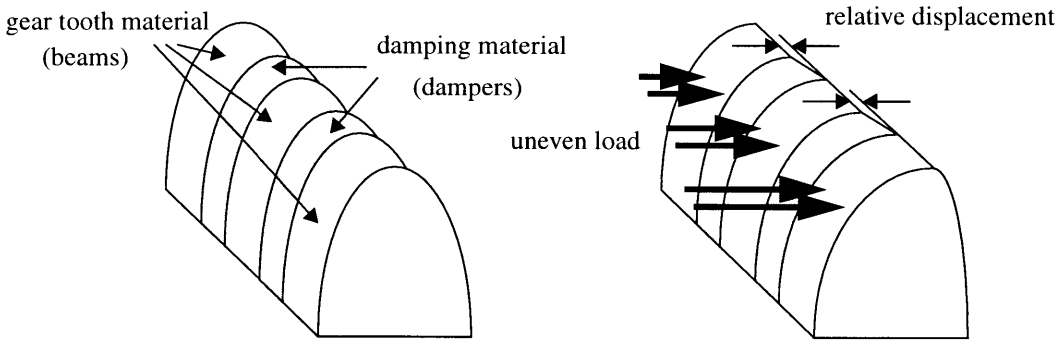

Figure 1.2: Design Concept of Bimetallic Composite Gear Tooth

Shown in Fig. 1.2 are the modified gear teeth. the modified gear teeth or *bimetallic composite gear teeth* are made by cutting thin slits in the gear teeth and filling them with damping material or

a low-strength metal alloy. This modification increases the internal damping of gears and dissipates the vibration energy during the loading and unloading cycles. Uneven loading across the width of gear teeth occurs as gears mesh due to various loading conditions, such as multiple tooth contact, different loading points across the width, and local load concentration caused by surface imperfections. The uneven loading causes relative displacements among the separated segments of gear teeth, which are referred to as *beams* throughout this paper. The vibration energy generated by gear mesh is to be dampened by the deformation of the inserted damping material, we call *dampers*. This relative displacements results in the overall reduction of vibration and noise.

1.4 Thesis Description

The objective of this thesis is to report the progress of this research in evaluating the effectiveness of the design concept in gear noise reduction, and thereby recommend future steps for the design of silent high-performance gears.

This thesis consists of six chapters. Following the project introduction in Chapter 1, Chapter 2 explains the general background informations regarding gears and their noise. The following three chapters are the main body of this thesis. Chapter 3 explains the preliminary experimental analysis performed using bimetallic composite bevel gears. The investigation on bimetallic composite helical gears follows in Chapter 4 with detailed description of the composite gear manufacturing. Theoretical analysis of the cyclic energy loss due to the partial plastic deformation of the damper is also explained in this section. Chapter 5 describes the gear tooth modeling performed using a bimetallic beam structure. Detailed explanation for the experimental damping coefficient measurement of beam structures is also presented in this section in order to understand the dynamics of gear teeth. Finally, in Chapter 6, all the chapters are summarized, and several recommendations for the future study of this project are made.

Chapter 2

Analysis on Gears and Gear Noise

2.1 Gears and their Nomenclature

A gear is defined as "a toothed machine part that meshes with another toothed part to transmit motion or to change speed or direction [5]". In general, gears may be divided into two broad classifications based on the arrangement of the axes of the gear pair: (1) parallel axes (spur, helical) or (2) nonparallel axes (straight bevel, spiral bevel, hypoid) [6].

A spur gear has its teeth parallel to the axis of the rotation. A helical gear is similar to a spur gear except that the teeth are cut on a spiral that wraps around the gear body. Helical gear teeth produce smoother action and therefore, tend to be quieter than spur gear teeth because they progressively enter the meshing zone where they mesh with the teeth of the other gear. Straight bevel gears are used in nonparallel axis applications, and their teeth are not parallel to the axis of the rotation [5]. Most of gear teeth are made in involute because it generates the most constant angular velocity. The involute is described as the curve traced by a point on a taunt string unwound from a *base circle* [7].

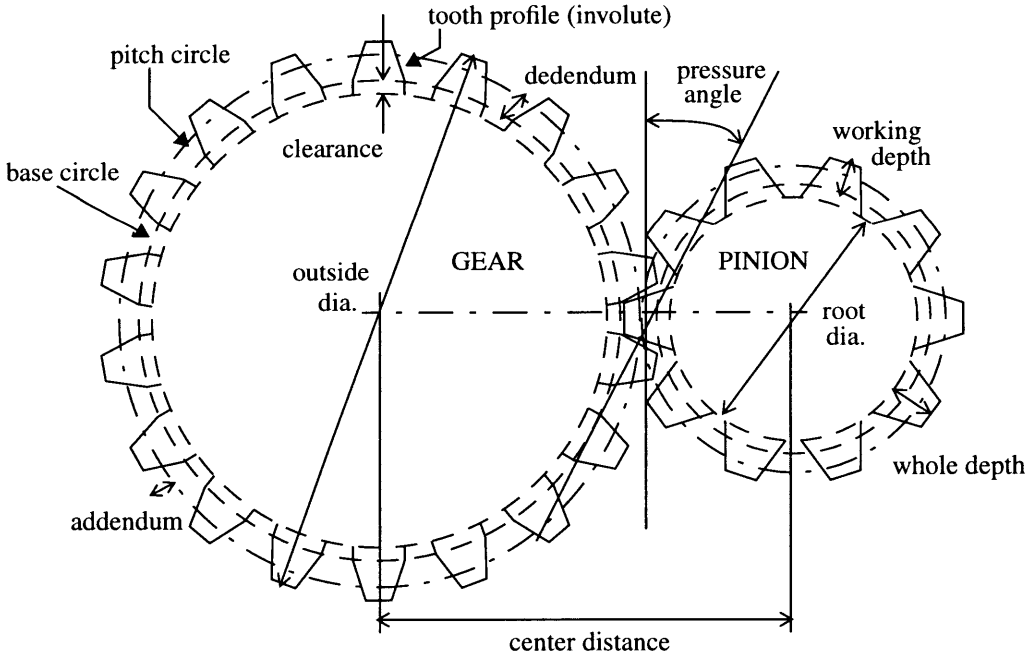

Figure 2.1: Spur Gear Nomenclature [8]

There are some key terms that need to be identified in order to understand gears. For spur gears [8],

- *addendum* is the height by which a tooth projects beyond the pitch circle or pitch line.
- *backlash* is the amount by which the width of a tooth space exceeds the thickness of the engaging tooth on the pitch circles.
- *contact ratio* is the number of angular pitches through which a tooth surface rotates from the beginning to the end of contact.
- *dedendum* is the depth of a tooth space below the pitch line. It is normally greater than the addendum of the mating gear to provide clearance.
- *gear* is a machine part with gear teeth. When two gears run together, the one with the larger number of teeth is called the gear.
- *pitch circle* is the circle derived from a number of teeth and a specified diametral or circular pitch. Circle on which spacing or tooth profiles is established and from which the tooth proportions are constructed.
- *pinion* is a machine part with gear teeth. When two gears run together, the one with the smaller number of teeth is called the pinion.
- *pressure angle* is the angle between a normal to the tooth profile in that plane and the line of intersection of that plane with the corresponding planes. In involute teeth, pressure angle is often described also as the angle between the line of action and the line tangent to the pitch circle. Standard pressure angles are established in connection with standard gear-tooth proportions.
- *root diameter* is the diameter at the base of the tooth space.
- *whole depth* is the total depth of a tooth space, equal to addendum plus dedendum, equal to the working depth plus variance.
- *working depth* is the depth of engagement of two gears; that is, the sum of their addenda.

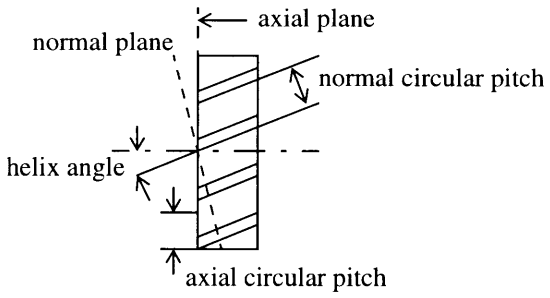

Figure 2.2: Helical Gear Nomenclature [8]

For helical gears [8],

- *helix angle* is the angle between any helix and an element of its cylinder.
- *lead* is the axial advance of a helix for one complete turn, as in the threads of cylindrical

worms and teeth of helical gears.

- *normal diametral pitch* is the diametrical pitch as calculate in the normal plane

2.2 Gear Noise

Although it is often overlooked, gear noise is a very important gear design consideration. Due to increasing consumer awareness and noise regulation, the concern has grown more pronounced over the years. Gear noise is characterized by discrete high frequency components caused by the dynamics of gear teeth, which is amplified by the gear train structure [2]. Therefore, the resulting noise mainly depends on the resonance of gear train structure and the meshing frequency (MF) of the gears. The source of the vibration is the gear contact which causes the direct air-born noise from the source. However, most of the vibration is transmitted to the surrounding structure, further resulting in structure-born noise. Part of this vibration energy passes through the base, causing floor noise-radiation, or "secondary noise" as shown in Fig. 2.3, and is not specifically related to the gear unit and depends only on its mounting and floor characteristics [4].

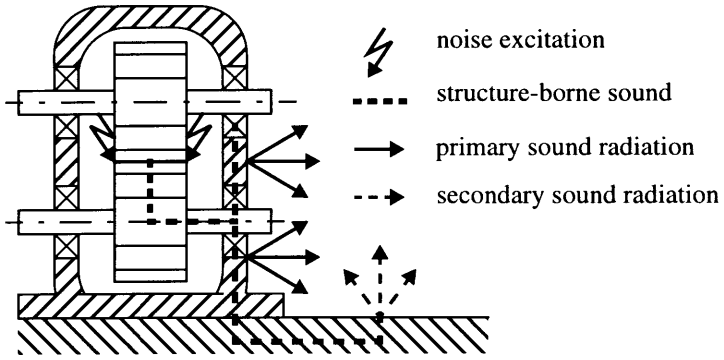

Figure 2.3: Radiation of Gear Noise [4]

In most cases the gear sound originating from the gear mesh are due to non-perfect or non-conjugate action of the gears. This non-perfect action results in dynamic forces at the gear teeth, which in turn excite vibrations of gears. As dynamic forces in the gear mesh are transmitted through the shafting and bearings to the housing panels, they serve as the "speakers" that propagate the gear noise heard by the listener [9].

2.2.1 Gear Noise Analysis

Gear noise is characterized by frequency components at the gear mesh frequency (MF) and its harmonics, and by modulations of MF or "sidebands" [9]. MF is the frequency of gear tooth

contact, and it is given by,

$$\text{mesh freqency [Hz]} = \frac{\text{rotational speed [rpm]} \cdot \text{number of teeth}}{60} . \tag{2.1}$$

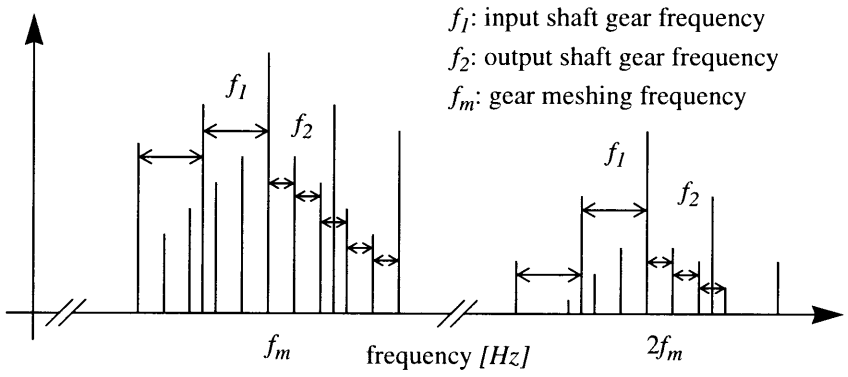

Figure 2.4: Dominant Frequency Components in Typical Gear Noise [9]

Harmonics occur at integer multiples of the MF. Side bands, which are commonly spaced at the input and output shaft frequency, occur about both the MF and its harmonics as in Fig. 2.4. Shaft frequency is the frequency of shaft rotation, and therefore it is,

$$\text{shaft freqency [Hz]} = \frac{\text{rotational speed [rpm]}}{60} . \tag{2.2}$$

2.2.2 Gear Noise Factors

There are four major factors affecting gear noise: (1) transmission error, (2) mesh stiffness, (3) frictional force, and (4) gear tooth impacts [9]. Transmission error is the most important factor in the generation of gear noise. It is "the difference between the actual position of the output gear and the position it would occupy if the gears were perfectly conjugate", and may be expressed in angular units or as a linear displacement along the line of action. There are two types of transmission error. The first is the manufactured transmission error (MTE), which is obtained for unloaded gear sets when rotated in single flank contact. The second is loaded transmission error (LTE), which is similar in principle to MTE but takes account tooth deflections due to load.

When gears are unloaded, MTE results from manufacturing inaccuracies such as profile errors, spacing errors, and gear tooth run-out, which is a "plus" amount of material added to either a pinion tooth or gear tooth which will cause a positive transmission error. When loaded, the changes in deflections due to mesh stiffness variations must be accounted for in the evaluation of LTE because tooth deflections cause the output gear to lag behind the input gear and result in

negative transmission error. The time-varying component of both MTE and LTE is periodic at tooth MF, and it has shown to be related to gear noise amplitude. In fact, it has been shown that the transmission error of spur gears, which have large changes in mesh stiffness, can be reduced significantly by applying appropriate profile modifications. Unfortunately, for spur gears these modifications are usually an optimum for one load level, and gears operating away from this design load will have increased noise.

Mesh stiffness is the ratio of the force to tooth deflection along the line of action, and it varies as the gear teeth rotate through a mesh cycle. In spur gears where tooth contact alternates between single-tooth-pair contact and double-tooth-pair contact, the mesh stiffness by alternating between the stiffness of a single-tooth-pair and the stiffness of double-tooth-pair in parallel, changes by a factor of two as gears rotate. For helical gears the mesh stiffness is roughly proportional to the sum of the lengths of the respective contact lines.

Frictional force due to gear tooth sliding provides a MF excitation as well. The meshing gear teeth is a combination of rolling and sliding; as the gear teeth enter contact as in approaching action, sliding is at a maximum. It decreases to zero when it reaches the pitch point where pure rolling exists. Then, the sliding direction reverses as contact progresses past the pitch point. This change in sliding direction at the pitch point causes a sudden reversal in the direction of the frictional force causing gear excitation.

Gear tooth impacts occur when tooth deflections and spacing errors cause tooth contact to occur prematurely at the tooth tip. This premature contact occurs off the line of action due to a velocity mismatch normal to the tooth contact, resulting in an impact at the tip of the driven tooth. This impact generates large dynamic forces, which not only can cause large MF noise levels, but can also significantly decrease gear tooth fatigue life. These impacts can be minimized by providing adequate tip and root relief and tooth crowning. Even with proper relief, however, there is a sudden shear force due to the instantaneous sliding that occurs at the initiation of contact. This can become a source of noise.

Although the applications of gears differ widely, the sources of gear noise remain more or less the same. Therefore, some general statements can be made concerning design trends that yield quieter gears. Based on the flow of acoustic and vibration energy, several approaches may be taken to reduce gear noise [9]:

1. Reduce the excitation at the gear mesh.
2. Reduce the dynamic force paths and the vibrations between the gear mesh and the housing.

3. Reduce the housing's acoustic radiation efficiency.
4. Modify the environment in which the gearbox is placed.

2.2.3 Gear Noise Measurement

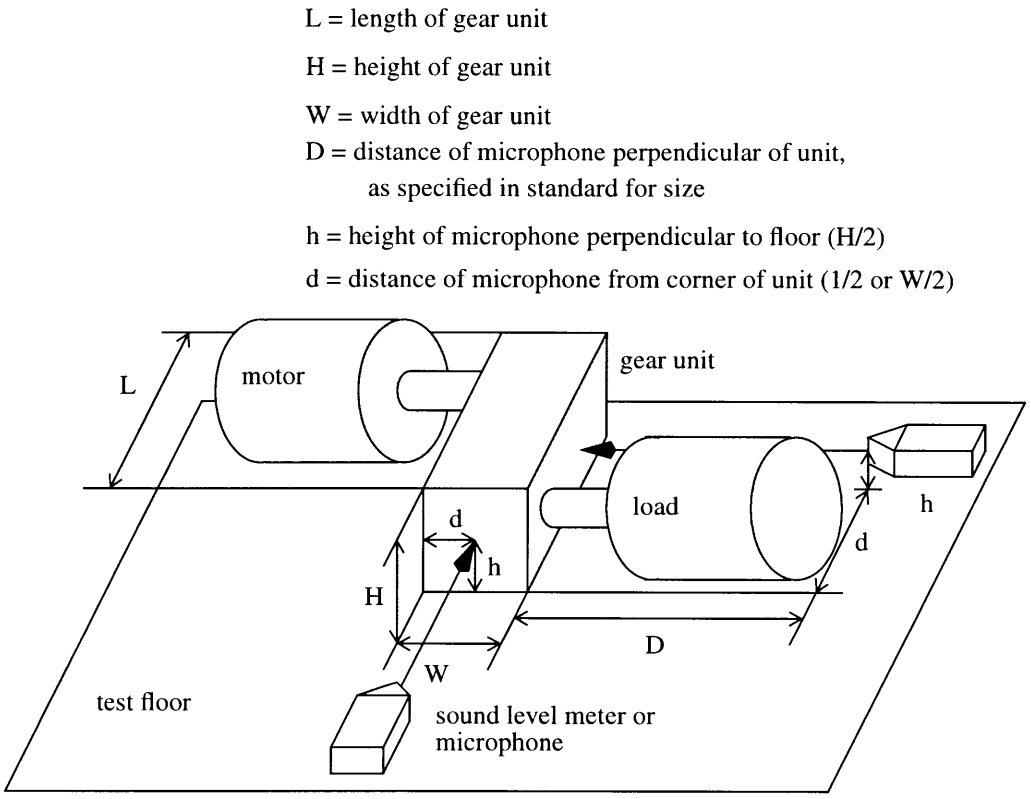

Figure 2.5: Single Microphone Location in AGMA Standards [9]

Fig. 2.5 shows a recommended location of the microphone for measurement of noise from a gearbox by the American Gear Manufacturers' Association (AGMA). Full-load experiments require quite elaborate and therefore, expensive experimental setups. The cost of the input motor and the load mechanism themselves can be quite expensive as the gear's rated horsepower gets high. Also, the drive for these motors is very expensive especially when the variable speed control is necessary[1].

1. More information on the components of the experimental apparatus is explained in Appendix A.

Chapter 3

Investigation on Bimetallic Composite Bevel Gears

3.1 Bimetallic Composite Bevel Gears

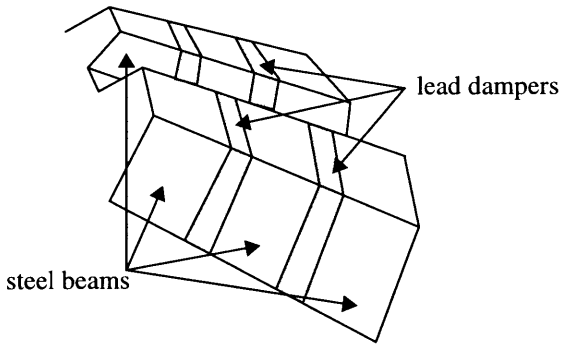

Figure 3.1: Bimetallic Composite Bevel Gear Teeth[1]

In order to verify the design idea of a low-noise bimetallic composite gear set, a preliminary test is performed using a *R1211 1.5 speed-ratio straight right-angle bevel gear drive* from Boston Gears. After full measurement of the vibration and noise level of the original gear set, it is modified to be a bimetallic composite gear set.

The housing of the test gearbox is made of fine-grained, gear-quality cast iron, providing maximum strength and durability. The gears are made of high-grade nickel chromium molybdenum steel for superior heat-treating of gears [8]. Because the surface of the gears is heat-treated or hardened for the maximum durability and stiffness, the conventional steel tools cannot penetrate through the surface, and therefore, an alternative method is used for machining.

Aluminum oxide grind wheels of 2 *mm* thickness are used to cut the slits. As a result, two slots of about 3 *mm* thickness are made in all 16 pinion teeth and 24 gear teeth along the line of loading as shown in Fig. 3.1. Then the slots are mechanically filled with a damping material, lead.

1. The pictures are shown in Appendix B.

3.2 Experimental Analysis

3.2.1 Experimental Apparatus and Procedure

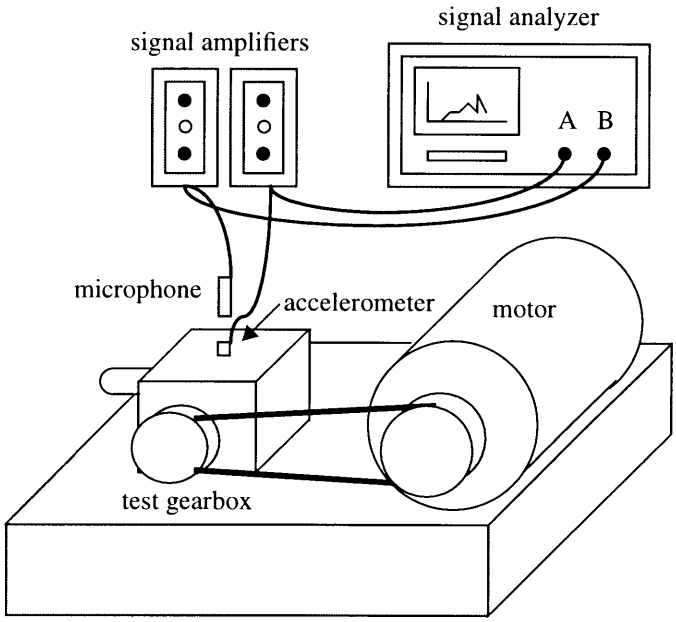

Figure 3.2: Experimental Apparatus for Bimetallic Composite Bevel Gears

Shown in Fig. 3.2, a simple experimental apparatus is set up. The test gearbox is mounted to an experimental setup with a 1 *hp* AC motor attached to the pinion of the gear set. A v-belt is used for power transmission between the motor and the gearbox.

An accelerometer and a microphone are mounted on top of the test gearbox in order to measure the vibration and noise level of the gears. The vibration signal is then amplified by an AC-powered signal amplifier, and the noise signal is amplified by a battery-operated signal amplifier. Both vibration and noise signals are then processed using an AC-powered signal analyzer.

Table 3.1: Key Frequency Components in Bevel Gear Experiment Settings

Fig.	rotational speed [*rpm*]	MF mesh frequency [*Hz*]	SF shaft frequency		BF bearing frequency[a]	
			pinion [*Hz*]	gear [*Hz*]	pinion [*Hz*]	gear [*Hz*]
3.3	300	80	5	7.5	70, 90	105, 143
3.4	600	160	15	10	140, 190	210, 285
3.5	900	240	15	22.5	210, 285	315, 428

a. one frequency for the bearing with 14 balls, the other with 19 balls

The level of both vibration and noise is measured for the input-shaft rotational speed settings of 300, 600 and 900 *rpm*. These are 80, 160, and 240 *Hz*, respectively in terms of mesh frequency (MF). Listed in Table 3.1 are the key frequency components of the experimental settings, all related to the test speed. Shaft frequency (SF) is the frequency of axis rotation, which can be calculated by dividing rotational speed in *rpm* by 60 seconds, and bearing frequency (BF) is SF times the number of balls in the bearings. Each axis of the test gearbox is supported by two ball-bearings; one has 14 balls, and the other 19 balls.

3.2.2 Experimental Results

The experimental data of the vibration/noise level of both original gears (OG) and bimetallic composite gears (CG) are presented in the following three figures, Figs. 3.3, 3.4 and 3.5, each consisting of four graphs. Graphs (a) and (c) on the left side, represent the vibration level, and graphs (b) and (d) on the right side, the noise level. Graphs (a) and (b) show the frequency components of the experimental data measured at the sampling frequency of 1 *kHz*, and graphs (c) and (d) show the components measured at a 10 *kHz* sampling frequency.

In all the graphs, the dotted line represents the data of the original gears (OG), and the solid line represents those of the modified bimetallic composite gears (CG). All of the harmonics of the MF's are indicated by the corresponding harmonic numbers, e.g., one for the fundamental MF, two for the second harmonic of the fundamental MF, and so on.

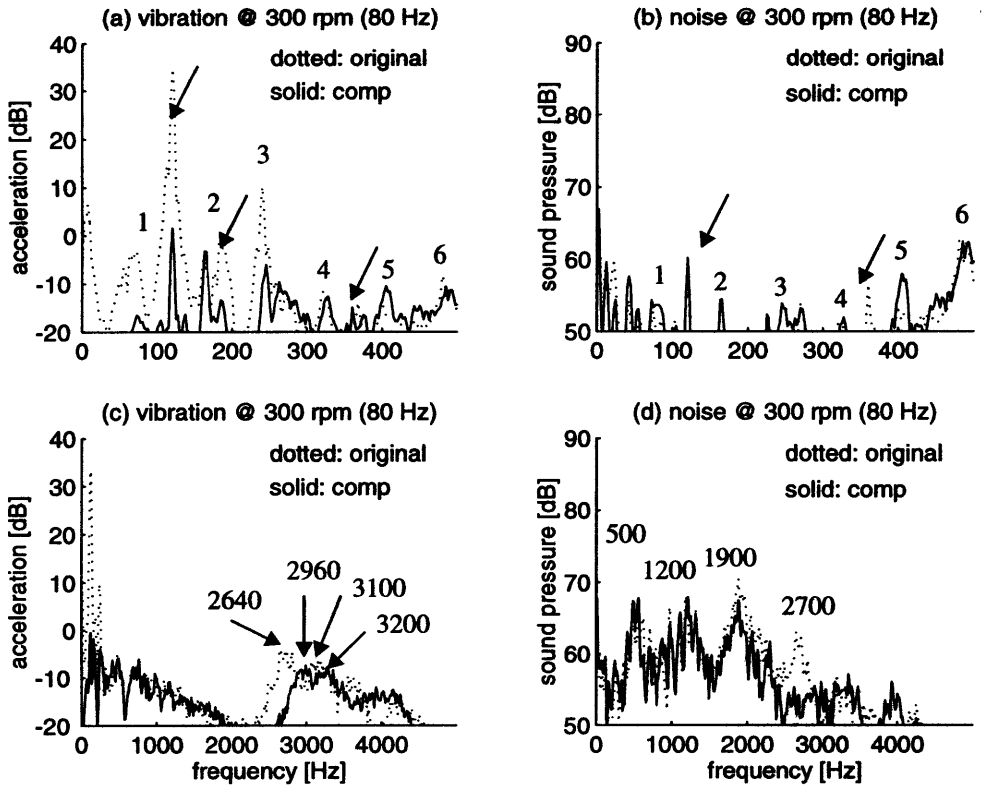

Figure 3.3: Vibration and Noise Frequency Spectra of Bevel Gears at 300 *rpm*

Fig. 3.3 shows the experimental data at 300 *rpm* or at 80 *Hz* MF. Besides the marked harmonics of the MF, graph (a) shows strong frequency components at 120, 180, and 360 *Hz* indicated by the arrows. Because they are not the harmonics of the MF, they are assessed to be the amplified harmonics of AC electrical noise at 60 *Hz*. They are most likely entered into the output signal through the AC-powered signal amplifier and signal analyzer. The fact that the vibration level is higher at the third harmonic of the MF at 240 *Hz* in OG data than at the fundamental MF also confirms the existence of strong noise in the output signal because is it also the fourth harmonic frequency of the AC electrical noise. Therefore, the frequency components below 400 *Hz* are disregarded in the data analysis.

Graph (c) shows two peaks at 2640 and 3100 *Hz* in the OG data and two peaks at 2960 and 3200 *Hz* in the CG data. Those peaks are considered to be the counterparts of one another, leading to an observation that about 3 to 5 *dB* drops are established in the vibration level due to the modification of the gear teeth.

Graph (d) shows that at 500 *Hz*, the noise level of the CG data is about 2 *dB* higher than that of the OG data, yet at 1880 *Hz*, the CG noise level is about 3 *dB* lower than the OG noise level. At

1200 *Hz*, both data indicate that they are at about the same level. At 2700 *Hz*, the CG noise level is almost 10 *dB* lower than that of the OG noise level. Therefore in terms of the noise level, the improvement of the modification is found to be negligible at or below 300 *rpm*.

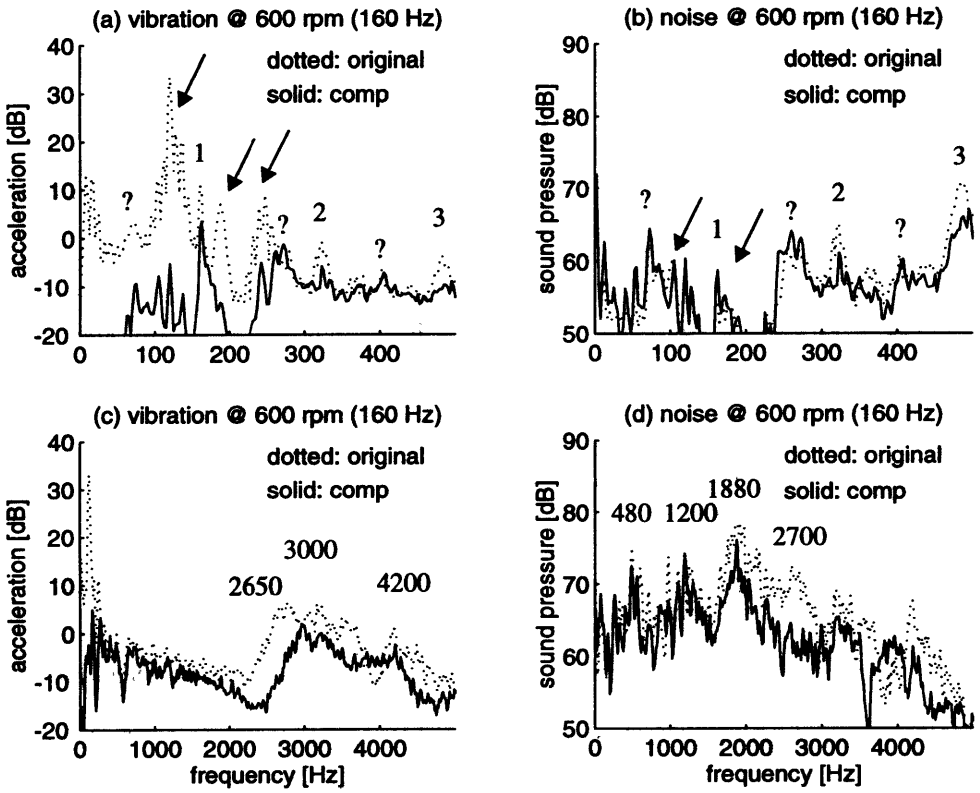

Figure 3.4: Vibration and Noise Frequency Spectra of Bevel Gears at 600 *rpm*

Fig. 3.4 shows the experimental data at 600 *rpm* or 160 *Hz*. Graph (a) confirms the strong influence of the electrical noise in the vibration signal under 400 *Hz*. There are three peculiar frequency components at 80, 270, and 410 *Hz* in both graphs (a) and (b) indicated by the question marks. The sources of these components can be several. They perhaps originates from the harmonic excitation of BF or SF. When the source of the signal is not clear, it is regarded as *ghost noise*. The ghost noise is thought to be a surface-finish-related noise [9], since it often cannot be ascertained from profile and lead measurement.

Graph (c) indicates about 2 to 5 *dB* drops in the vibration level in the CG data and graph (d) indicates about 3 *dB* drops at 480 and 1880 *Hz* frequency components.

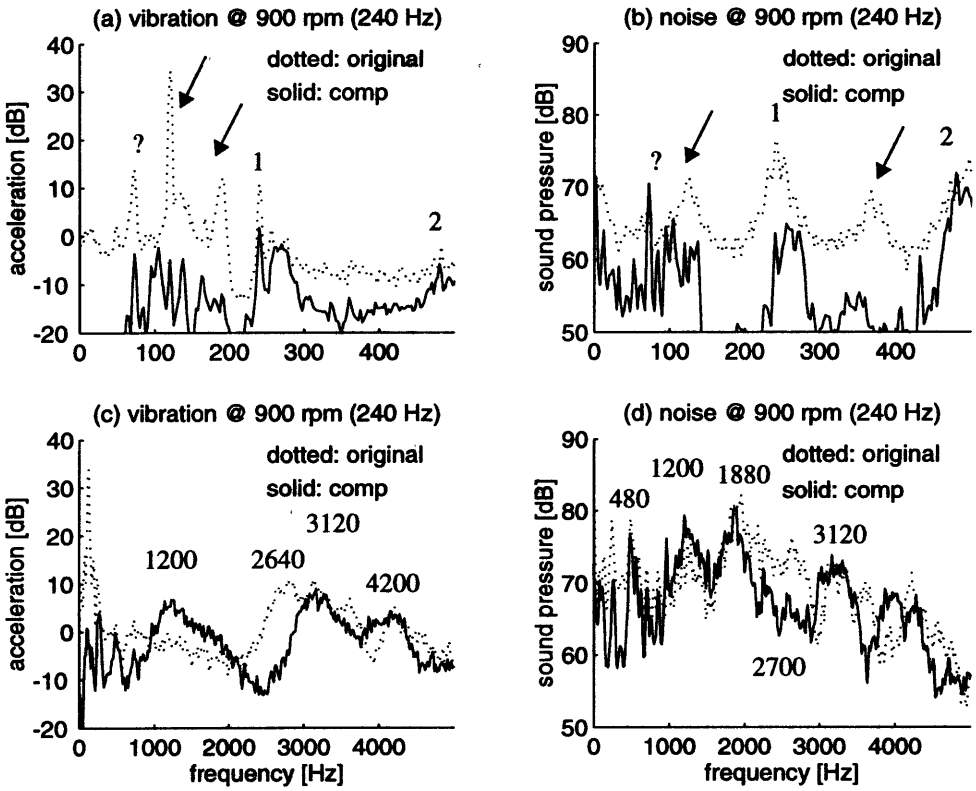

Figure 3.5: Vibration and Noise Frequency Spectra of Bevel Gears at 900 *rpm*

The experimental data at 900 *rpm* or at 240 *Hz* MF are shown in Fig. 3.5. Again, graphs (a) and (b) indicate the strong influence of the noise signal at 120 *Hz* and a ghost signal at 80 *Hz*.

The presence of a peak at 80 *Hz* at the output signals of both 160 and 240 *Hz* MF, indicates that this frequency component is independent of the test speed. Therefore, its source should be a non-moving source, most likely caused by the natural frequency of some structure in the experimental setup.

We again see about 2 *dB* drop in the vibration level of the CG data at 3102 and 4200 *Hz* in graph (c). The noise data in graph (d) show 2 *dB* drops at 480 and 1880 *Hz*, and a 10 *dB* drop at 2700 *Hz* although the noise level is raised about 1 to 3 *dB* at 1200 and 3120 *Hz*.

3.3 Conclusions

Experimental results indicate an overall vibration and noise reduction of about 1 to 3 *dB* at several dominant MF harmonics due to the modification of the gear teeth. However, the electrical noise signals at 120, 240 and 360 *Hz* are identified in the output signals, and therefore it is recommended to raise the signal-to-noise ratio by introducing a load component in the experimental setup. As the gear teeth experience the gear load, the increased vibration from the increased load force will not only amplify the signal-to-noise ratio but also it will eliminate the gear rattle noise. Furthermore, the load is expected to increase the damping effect of the bimetallic composite gear teeth due to an increased deflection difference among the beams of the gear teeth.

The choice of MF's turns out to be also important. In order to fully map out the vibration and noise response characteristics of the test gears and the experimental setup, distinctive sets of MF's are required. However, because three chosen MF's are the harmonics of one MF in this experiment, it is difficult to distinguish the sources of some frequency components.

Chapter 4

Investigation on Bimetallic Composite Helical Gears

4.1 Bimetallic Composite Helical Gears

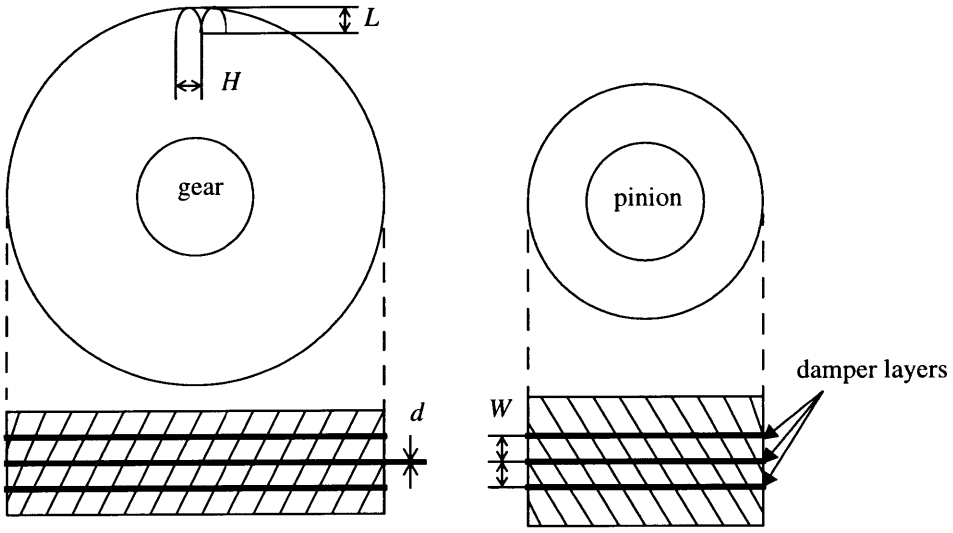

Figure 4.1: Bimetallic Composite Helical Gears.

Table 4.1: Dimensions of the Beams and the Damper

unit	length, L	height, H	width, W	thickness, d
[*mm*]	2.2	3	2.8	0.4
[*in*]	0.088	0.12	0.112	0.016

From the preliminary experiment described in Chapter 3, several improvements are recommended for the experimental setup. The recommended experimental settings of higher mesh frequency (MF) and heavier load necessitate a new apparatus consisting of an input motor, an output load, and a test gearbox.

For test gears, even though spur gears are preferred for the ease of theoretical modeling, helical gears are chosen for two reasons. One is that spur gearboxes can only be purchase through custom orders because helical gears are used in most of the gearboxes due to their advantages of quieter and smoother operation over spur gears. The other is that helical gear teeth induce larger load difference across the gear face since its teeth are angled against the load line, which may amplify the damping effect of the bimetallic structure.

A gearbox rather than a gear set is purchased for the quality of gear axis alignment. Since the gear noise and its dynamics are highly sensitive to the gear axis alignment, it is important to have precisely aligned axes for gear noise experiments in order to avoid any possible noise source other than the gear contact.

Two gearboxes of *601A 1.6 foot-mounted single-reduction non-flanged speed-reducer* from Boston Gears are chosen to be test gearboxes due to the proper size of its gears. In order to load the gears significantly, small gear teeth are preferred so that the power requirements of the input motor and the output load are easily met with a relatively small and affordable experimental setup. At the same time, if their size is too small, it becomes difficult to modify them to be bimetallic composite gear teeth, so careful consideration is given in the test gear selection. Shown in Fig. 4.1 is the helical gears[1]. Key dimensions of the beams and the damper are labeled in Fig. 4.1 and listed in Table 4.1.

Unlike the previous mechanically-filled damper in the bimetallic composite bevel gears, the damping material is soldered into the slot for the helical gears in order to ensure the solid bonding of the beams and dampers. *MG 120 Low Temperature Soft Bearing Solder*, which is composed of 95% tin and 5% of silver, is chosen as damper material for its affordability and availability as well as its low yield strength. Its technical data are listed in Table 4.2.

Table 4.2: Technical Data of MG 120 Low Temperature Soft Bearing Solder

tensile strength	up to 15,000 *psi* (10 kg/mm^2)
working temperature	430 *F* (221 *c*)
hardness (*HB*)	15

Previously, because the gear teeth are hardened by surface heat-treatment for durability and strength, aluminum oxide grind wheels were used for machining of the bevel gears. However, because the thickness of the resulting slots from the grind wheels is too wide for the chosen helical gears, a wire electro-discharge machining (wire EDM) is employed, resulting in three narrow strips of slots of about 12 to 15 *thousandth inch*, or 0.4 *mm*.

The basic principle of the wire EDM is to melt the material locally by an electrical connection between the cutting wire and the material. Therefore, only the conductible material can be cut by wire EDM. A thin electrified wire, whose size varies according to the size of the cuts to be made, is

1. Their detailed dimensions are listed in Tables B.1 and B.2 of Appendix B, the first defined by ANSI system, and the latter by international metric system.

used for the cutting. As the material gets close to the electrified wire of high voltage, sparks occur between the wire and the material, locally raising the temperature of the material to its melting point. A stream of coolant water surrounding the cutting wire washes the melted parts as the wire melts through the material. One major problem caused by wire EDM is that because the melting is followed by rapid cooling within the stream of water, oxidation occurs, resulting in rust film over the cut-surface. This film is mechanically and chemically cleaned with a wire brush and acid cleaner before the soldering process to ensure solid bonding of the beams and dampers.

It is very important not only to fill the gap, but also not to change the involute profile of the gear teeth; soldering must not cause any defects on the gear tooth surface because any defects will affect the noise of gears. First, hot-bath method is tested; the gear surface is covered with epoxy crust, which has cuts along the slots in order to prevent the oxidation and bonding of solder on unwanted gear surface. Then, the gear is heated to the solder-melting temperature and submerged to the melted solder bath. However, this method fails to fill the gap because the solder material could not flow into the slots since the melted solder does not wet the epoxy surface. Hence, direct soldering is chosen to fill the slits with solder material, and the undesirable solder material on the tooth contact surface is cleaned mechanically after the soldering.

As for the soldering, the gear is mounted on the lathe and heated by a torch. The solder is melted on the gear teeth by the raised temperature of gear teeth from the torch. Because the heat attracts the liquid solder, local heating is also applied to direct the flow of the melted solder with a small soldering gun.

Cleaning is performed with very fine sandpaper wheels to remove the excess solder material between the teeth. Also, careful hand-filing is performed to clean up the surfaces. Therefore, small changes or defects in the surface finish and/or in the profile of the involute gear tooth are unavoidable through the modification process.

4.2 Theoretical Analysis

4.2.1 Loading Condition in Helical Gears

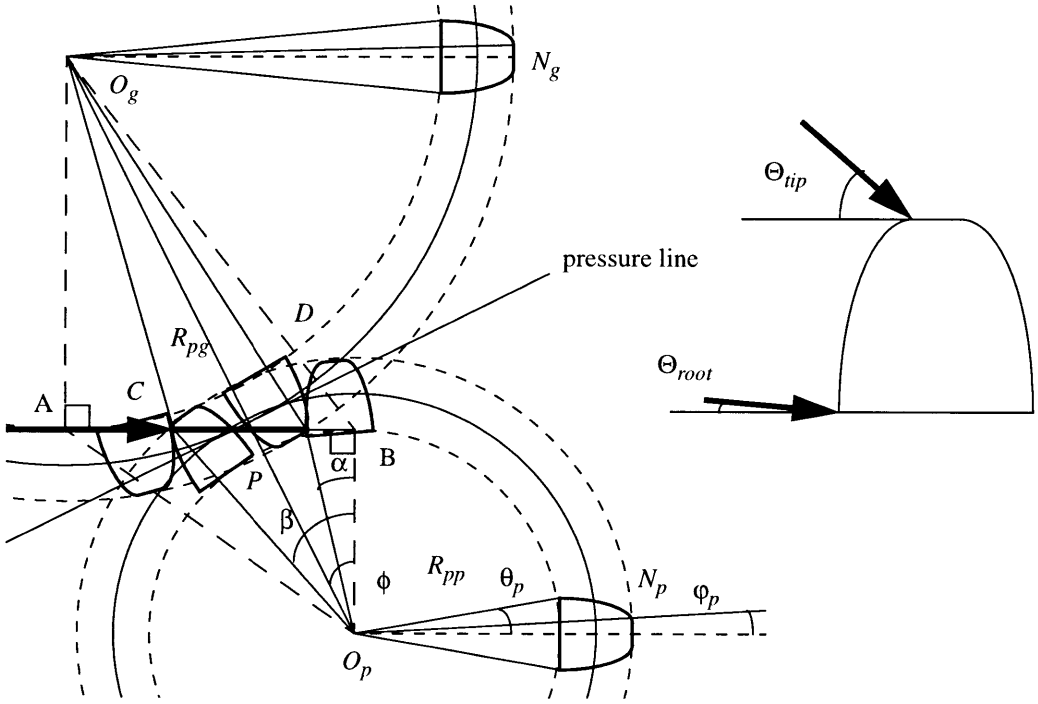

Figure 4.2: Loading Condition of Helical Gears

Table 4.3: Key Values of Loading Condition

PB	PC	PD	θ_p	φ_p	Θ_{root}	Θ_{root}
5.57 *mm*	2.47 *mm*	2.61 *mm*	6°	2°	23.7°	4.94°

First, it is necessary to understand the loading condition of helical gears, especially, the load difference among the beams in a helical gear tooth. As gears mesh, loading occurs along the contact line $\overline{CD}$, as shown in Fig. 4.2. The contact line is defined as the line where the gear contact occurs, and it partially coincides with the line $\overline{AB}$, which tangentially meets the two base circles of a gear set. For a constant torque operation, the loading force is constant along the contact line.

The orientation of the gear teeth changes as the tooth contact progresses through the contact line. Fig. 4.2 shows the loading condition of a pinion tooth when the tooth is loaded at the tip at point C and at the root of the gear tooth at point D.

In order to calculate the angle of the loading force, or *loading angle*, the orientation of the gear tooth has to be identified. Simple geometric analysis yields the loading angles with respect to the gear tooth.

First, the length of $\overline{PC}$ and $\overline{PD}$ are calculated using the second cosine law of the trigonometry [10],

$$\overline{PC} = [(R_{pp} \cdot \sin\phi)^2 + (a^2 + 2 \cdot a \cdot R_{pp})]^{1/2} - (R_{pp} \cdot \sin\phi), \tag{4.1}$$

$$\overline{PD} = [(R_{pg} \cdot \sin\phi)^2 + (a^2 + 2 \cdot a \cdot R_{pg})]^{1/2} - (R_{pg} \cdot \sin\phi). \tag{4.2}$$

Here, R_{pp} is the pitch radius of the pinion, R_{pg} is the pitch radius of the gear, ϕ is the pressure angle of the gear set, and a is the addendum of the gears. The angle between the root and the tip is approximated as one third of the overall gear angle,

$$\varphi_p \approx \frac{2\theta_p}{3}, \tag{4.3}$$

where

$$\theta_p = \frac{360}{2N_p}. \tag{4.4}$$

Here N_p is the number of the pinion teeth. With the base radius of the pinion R_{bp} and the length of $\overline{PB}$,

$$\overline{PB} = R_{pp} \cdot \sin\phi \quad , \tag{4.5}$$

the loading angles at the root Θ_{root} and at the tip Θ_{tip} can be calculated,

$$\Theta_{root} = \alpha - \theta_p = \text{atan}\left(\frac{\overline{PB} - \overline{PD}}{R_{bp}}\right) - \theta_p, \tag{4.6}$$

$$\Theta_{tip} = \beta + \varphi_p - \theta_p = \text{atan}\left(\frac{\overline{PB} + \overline{PC}}{R_{bp}}\right) + \varphi_p - \theta_p. \tag{4.7}$$

Evaluation of the above equations with the appropriate value of the helical gear dimensions[1] yields 23.7° of the tip loading angle and 4.9° of the root loading angle.

1. See Appendix C.

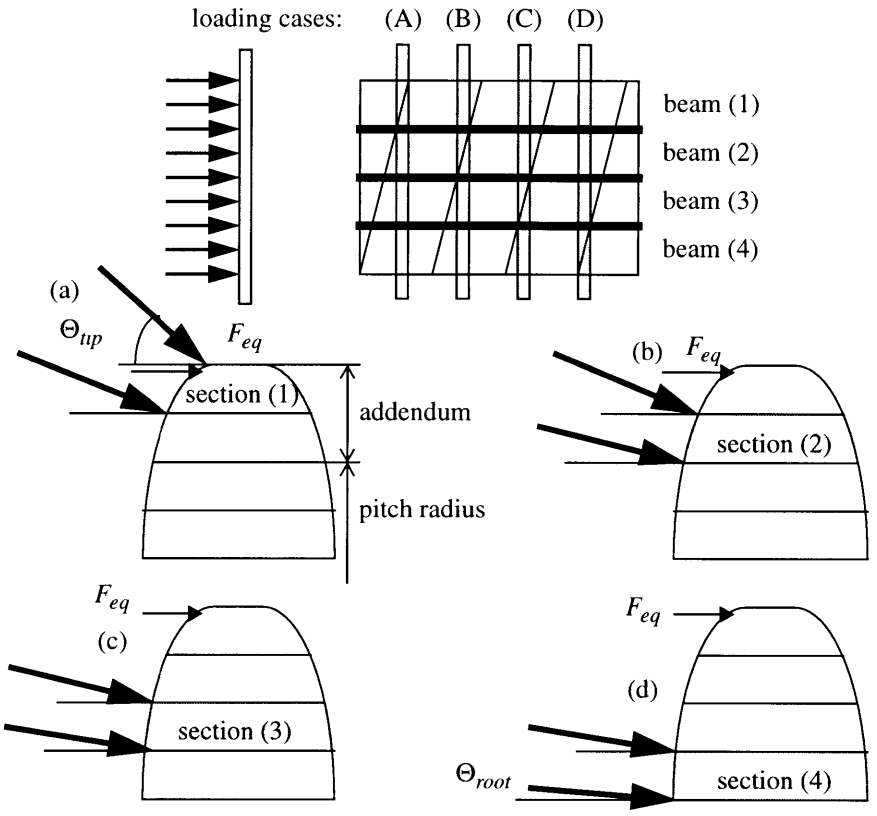

Figure 4.3: Different Loading Angles on Helical Gear Teeth

Table 4.4: Key Values of Loading Condition

PB	PC	PD	θ_p	φ_p	Θ_{root}	Θ_{root}
5.57 *mm*	2.47 *mm*	2.61 *mm*	6°	2°	23.7°	4.94°

From the discrete analysis of the loading conditions for the helical gears, the four cases of loading can be established for a gear set whose contact ratio is unity, as shown in Fig. 4.3. All the loaded area is indicated by the shaded area, and each loading case is labeled alphabetically.

Loading case (A) shows the case when the load is only applied to the first beam of the gear tooth. In this case, the load is only applied on section (1) as indicated in case (a). Loading case (B) is the case when the load is applied to the first two beams of a tooth, where beam (2) experiences the load in section (1) in case (a), and beam (2) experiences the load in section (2) in case (b), and so on. With the average value of the loading angles at the mid-point of each section, the equivalent tangential load is calculated, and they are listed in Table 4.4. Note that these tangential load are the equivalent values of the load on each corresponding sections of a beam shown in cases (a), (b), (c), and (d), when the load is assumed to be applied at the tip of the tooth profile.

According to Table 4.4, the maximum tangential load difference of about 249.76 N occurs in loading case (B) between beam (2) and (3) because beam (3) does not experience any loading. For loading case (A), the maximum difference of 246.46 N is loaded between beam (1) and (2). For loading case (C), the difference of 247 N between beam (3) and (4). For loading case (D), the maximum difference of only 3.3 N is loaded between beam (1) and (2), and between beam (2) and (3).

4.2.2 Modeling of Bimetallic Composite Beam

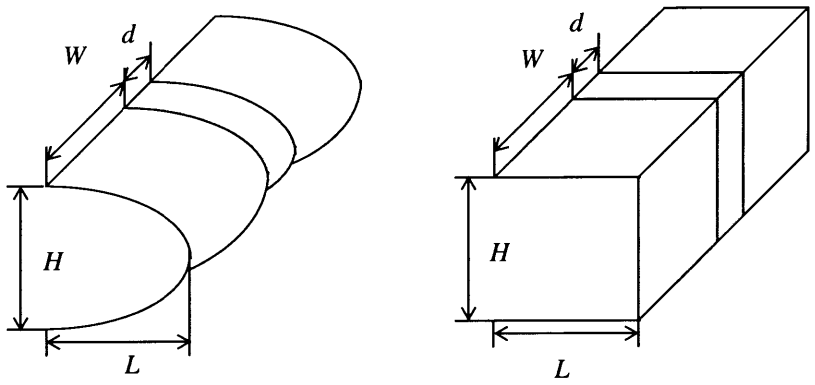

Figure 4.4: Square Beam Simplification for an Involute Composite Gear Tooth

A bimetallic composite gear tooth with an involute profile is modeled with a rectangular composite gear tooth of two steel beams and one tin damper as shown in Fig. 4.4.

Table 4.5: Dimensions of the Beams and the Damper

length, L	height, H	width, W	thickness, d
2 mm	2 mm	2 mm	0.4 mm

The deflection of a non-slender beam can be calculated with the following equation,

$$y(F,x) = \frac{FL^3}{6E_sI_b}(-x^3+3x^2) + \frac{\eta F}{A_bG_s}x, \tag{4.8}$$

where F is the load, E_s and G_s are Young's modulus and shear modulus of steel, and A_b and I_b are the cross-sectional area and the cross-sectional moment of the beam. When the beam is not slender, meaning that its height is larger than one tenth of its length, the deflection y has an extra term of $\frac{\eta F}{A_bG_s}x$ from the shear deflection of beam.

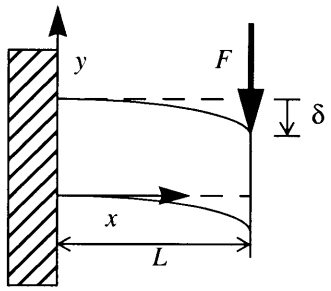

Figure 4.5: Deflection of a Non-Slender Beam

Here, η is a Timoshenko beam constant, which is 1.5 in the cases for a square cross-sectional area, and it is based on the assumption that the shear load is evenly distributed across the cross-sectional area [11].

This deflection equation can also be expressed with the deflection at the tip, δ, and the bending profile function of the beam, *f(x)*,

$$y(F,x) = \delta(F,L)\cdot f(x) = \left(\frac{FL^3}{3E_sI_b} + \frac{\eta FL}{A_bG_s}\right)\cdot\left[\frac{-A_bG_sx^3 + 3A_bG_sLx^2 + 6E_sI_bx}{2(A_bG_sL^3 + 3\eta E_sI_bL)}\right], \tag{4.9}$$

and they are,

$$\delta(F) = y(F,L) = \left(\frac{L^3}{3E_sI_b} + \frac{\eta L}{A_bG_s}\right)\cdot F\,, \tag{4.10}$$

$$f(x) = \left[\frac{-A_bG_sx^3 + 3A_bG_sLx^2 + 6\eta E_sI_bx}{2(A_bG_sL^3 + 3\eta E_sI_bL)}\right]. \tag{4.11}$$

4.2.3 Idealization of Stress-Strain Curve

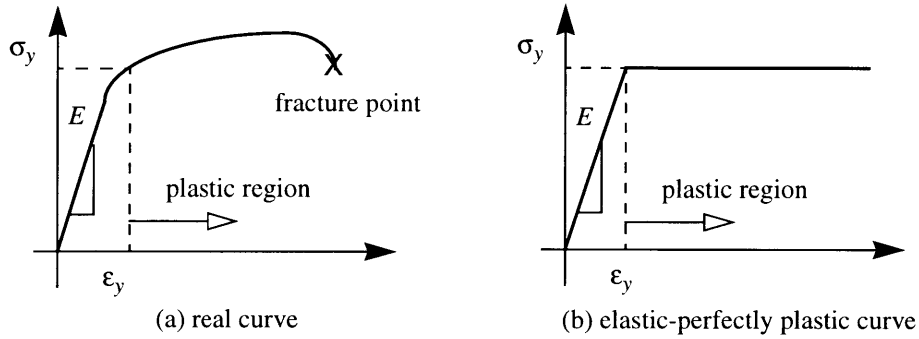

(a) real curve (b) elastic-perfectly plastic curve

Figure 4.6: Idealization of Strain and Stress Curve

As a piece of metal experiences elastic deformation, its stress rises linearly proportional to its strain. However, above a certain level of stress called *yield stress* or *yield strength*, the stress is no

longer linearly dependent on its strain, but follows the non-linear curve shown in Fig. 4.6(a) until the piece fractures at the fracture point. The region above the yield strain is called *the plastic region*, and it is very difficult to predict the deformation behavior of a material in this region. Therefore an approximation of elastic-perfectly plastic stress and strain relationship is made, as shown in Fig. 4.6(b), that the stress stays constant as the strain rises above the yielding point.

In evaluating three dimensional deformation, Mises equivalent stress $\bar{\sigma}$ is used [12],

$$\bar{\sigma} = \sqrt{\frac{(\sigma_x - \sigma_y)^2 + (\sigma_y - \sigma_z)^2 + (\sigma_z - \sigma_x)^2}{2} + 3(\tau_{xy}^2 + \tau_{yz}^2 + \tau_{zx}^2)} \tag{4.12}$$

where σ_x, σ_y, σ_z, τ_x, τ_y, and τ_z indicate the tangential and shear stresses in the x, y, z directions. Using the linear relationship between the stress and strain in the elastic region,

$$\sigma = E\varepsilon, \ \tau = G\gamma, \ G = \frac{E}{2(1+\upsilon)} \tag{4.13}$$

$$\upsilon = \text{Poissons Ratio} = 0.3$$

the equivalent strain increment $d\bar{\varepsilon}$ becomes,

$$d\bar{\varepsilon} = \sqrt{\frac{2\{(\varepsilon_x - \varepsilon_y)^2 + (\varepsilon_y - \varepsilon_z)^2 + (\varepsilon_z - \varepsilon_x)^2\}}{9} + \frac{\gamma_{xy}^2 + \gamma_{yz}^2 + \gamma_{zx}^2}{3}} \tag{4.14}$$

Table 4.6: Material Constants for Steel and Tin

items	steel		tin	
	symbol	value	symbol	value
density [kg/m^3]	ρ_s	$7.8\text{x}10^3$	ρ_t	$8.0\text{x}10^3$
Young's Modulus [N/m^2]	E_s	$200\text{x}10^9$	E_t	$50\text{x}10^9$
shear modulus [N/m^2]	G_s	$77\text{x}10^9$	G_t	$19\text{x}10^9$
yield strength [N/m^2]	$\sigma_{y,s}$	$1000\text{x}10^6$	$\sigma_{y,t}$	$14\text{x}10^6$
yield shear strength[a] [N/m^2]	$\tau_{y,s}$	$577\text{x}10^3$	$\tau_{y,t}$	$8\text{x}10^3$
yield strain	$\varepsilon_{y,s}$	$5\ \text{x}10^{-3}$	$\varepsilon_{y,t}$	$0.28\ \text{x}10^{-3}$
yield shear strain	$\gamma_{y,s}$	$7.5\ \text{x}10^{-3}$	$\gamma_{y,t}$	$0.42\ \text{x}10^{-3}$

a. yield shear strength is calculated by $\sigma_y = \sqrt{3}\tau_y$, using Mises equivalent stress formula, Eq. (4.12).

The material constants of the beam and the damper are listed in Table 4.6. Because most of the damper material consists of tin, the material constants of tin are used for those of the damper. Note

that Young's modulus of steel is about four times larger than that of tin, which means that it requires four times stronger force to elongate a steel piece to a certain amount than to elongate a tin piece. Also, the yield strength of tin, which is less then one fifth of that of steel, indicates that one fifth of force is capable of inducing plastic deformation of tin. In fact, one can easily deform a 2 *cm* by 2 *cm* tin bar plastically.

4.2.4 Damper Deformation

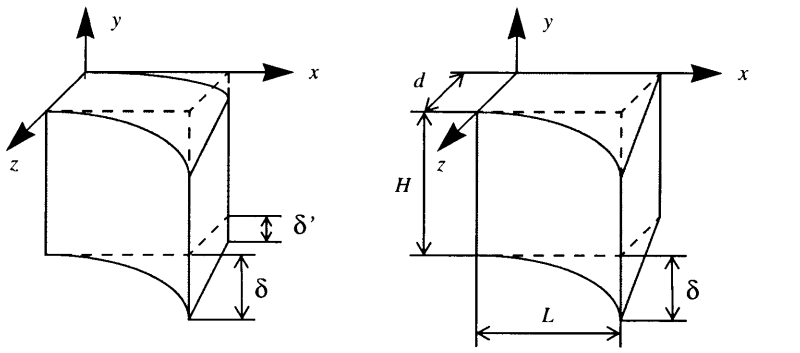

(a) real deformation of the damper (b) simplified deformation of the damper

Figure 4.7: Simplification of Damper Deformation

As one of the beams in a gear tooth experiences the input load, the damper undergoes a complicated three dimensional deformation as shown in Fig. 4.7(a). Here, δ is the resulting deflection on the side of the loaded beam, and δ' is the deflection on the side of the unloaded beam. Here we assume that δ' is very small, and therefore, the damper deformation is approximated as δ as shown in Fig. 4.7(b). Deformation profile in the z direction is approximated as straight.

Then, only v, the y directional deflection, is non-zero, and it is

$$v(F, x, z) = \frac{z}{d} y(F, x) = \frac{\delta(F)}{d} z f(x) . \tag{4.15}$$

If we apply this equation to the strain definitions,

$$\varepsilon_x = \frac{\partial u}{\partial x}, \ \varepsilon_y = \frac{\partial v}{\partial y}, \ \varepsilon_z = \frac{\partial w}{\partial z}, \ \gamma_{xy} = \frac{\partial u}{\partial y} + \frac{\partial v}{\partial x}, \ \gamma_{yz} = \frac{\partial v}{\partial z} + \frac{\partial w}{\partial y}, \ \gamma_{zx} = \frac{\partial w}{\partial x} + \frac{\partial u}{\partial z}, \tag{4.16}$$

and if we assume that the normal strain in the x direction ε_x is negligible with respect to the shear strain in the x and z directions, we find that only two components of strain become non-zero, which are,

$$\gamma_{xy} = \frac{\delta(F)}{\mathrm{d}} z \frac{d}{dx} f(x), \ \gamma_{yz} = \frac{\delta(F) f(x)}{\mathrm{d}} . \tag{4.17}$$

Therefore, the equivalent strain of the three-dimensional damper deformation can be evaluated with the following equation,

$$\bar{\varepsilon}(F, x, z) = \sqrt{\frac{\gamma_{xy}^2 + \gamma_{yz}^2}{3}} = \frac{\delta(F)}{d\sqrt{3}} \cdot \sqrt{(f(x))^2 + (zf'(x))^2}\,. \tag{4.18}$$

In above equations, δ is the deflection at the tip and $f'(x)$ is the first derivative of $f(x)$, which is the bending profile function, and they are previously defined in Eqs. (4.10) and (4.11).

4.2.5 Load Limits

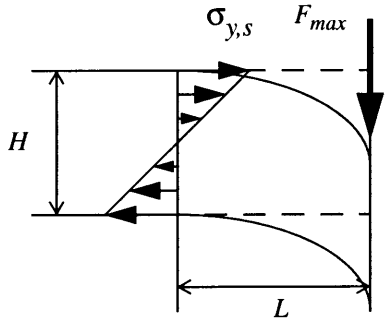

Figure 4.8: Stress Distribution of a Steel Beam at the Maximum Loading

The amounts of the maximum and the minimum load can be established by the load assumption that no part of the steel beam experiences plastic deformation, and a part of the damper has to experience plastic deformation. As shown in Fig. 4.8, the maximum load is calculated by considering the critical bending of the beam, where at the root of the beam, the top and bottom stress reaches the yield strength of the beam material. From the moment equilibrium equation,

$$\frac{F_{max} \cdot L}{W} = 2 \cdot \int_0^{H/2} \frac{2\sigma_{y,s}}{H} y^2 dy\,, \tag{4.19}$$

the maximum input load F_{max} can be calculated,

$$F_{max} = \frac{WH^2\sigma_{y,s}}{6L}\,. \tag{4.20}$$

The beam has to deflect a certain minimum amount in order for a part of the damper to undergo plastic deformation. This minimum deflection condition yields the minimum load limit. At minimum loading, the strain at the tip of the damper, that is when $x = L$ and $z = d$, has to be the same as the yield strain of the damper,

$$\frac{\sigma_{y,t}}{E_t} = \varepsilon_{y,t} = \bar{\varepsilon}_t(F_{min}, L, d) = \frac{\delta(F_{min})}{d\sqrt{3}} \cdot \sqrt{(f(L))^2 + (df'(L))^2}. \tag{4.21}$$

Therefore, the minimum force is,

$$F_{min} = d\sqrt{3} \cdot \frac{\sigma_{y,t}}{E_t} \cdot \frac{1}{\sqrt{(f(L))^2 + (df'(L))^2}} \cdot \left(\frac{L^3}{3E_sI_b} + \frac{\eta L}{A_bG_s}\right)^{-1}. \tag{4.22}$$

From above Eqs. (4.20) and (4.22), the maximum of 667 N and minimum load of between 7 to 50 N depending on the thickness of the damper, is calculated and graphed on Fig. 4.9[1]. Note that the maximum load is independent of the damper thickness and the minimum load is dependent on the thickness of the damper.

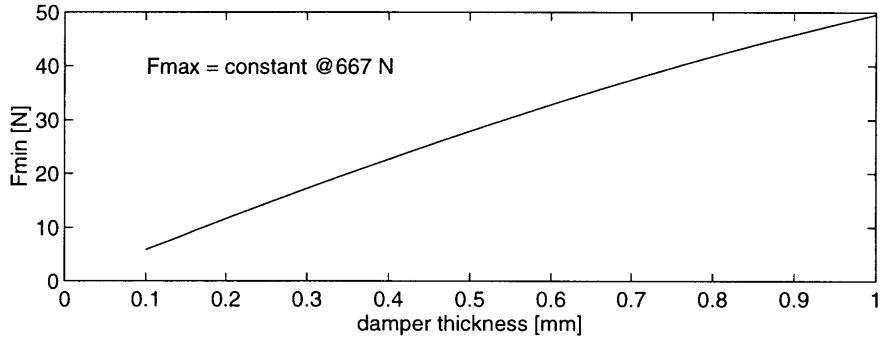

Figure 4.9: Maximum and Minimum Load

4.2.6 Cyclic Energy Loss Analysis

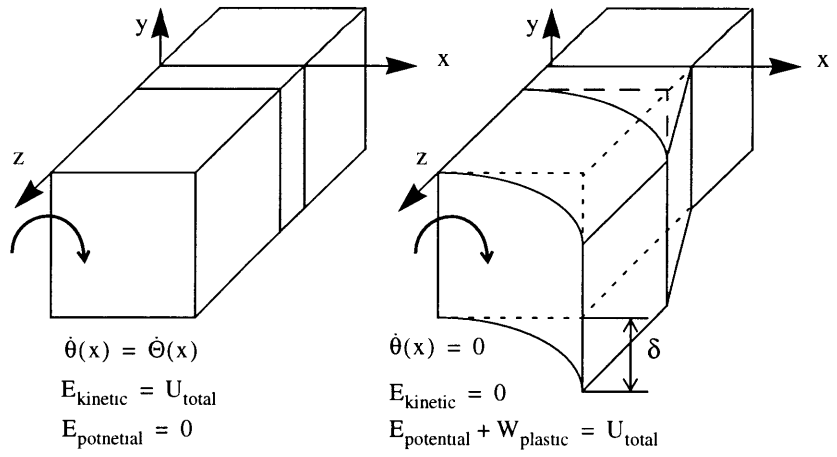

Figure 4.10: Vibration of a Steel Beam

1. For the calculation, refer to the Matlab program in Appendix C.

As one of the beams experiences loading and unloading cycles of heavy loads, energy loss occurs due to the partial plastic deformation of the damper. An analysis is performed to calculate the energy loss amount of a gear tooth as one of the beams undergoes one cycle of vibration from the initial position of zero deflection to the final position of zero deflection.

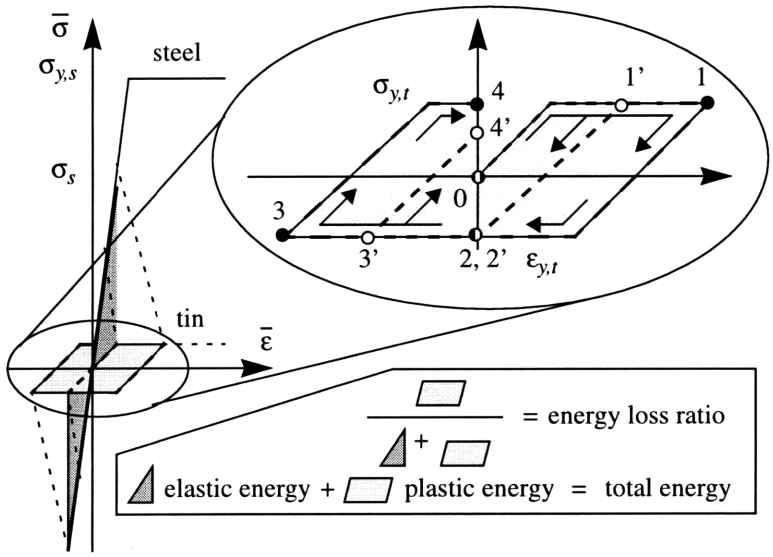

Figure 4.11: Stress and Strain of the Cyclic Energy Loss Analysis

We assume that there are certain amount of mechanical energy at the initial stage all in the form of kinetic energy. As the steel beam deforms, the existing kinetic energy turns into the potential energy, stored at the deflected steel beam and the deformed damper. However, due to the partial plastic deformation of the damper, some of the energy is lost, and therefore, the total energy of the system at the deflected stage is less than the initial energy at the initial stage.

The energy loss due to damper's plastic deformation continues as the steel beam bounces back to the initial position, after the deflection to the opposite side of the initial deflection. After one cycle of the vibration, the strain and the stress of the steel beam and the strain of the damper are zero, but the stress of the damper is not zero as shown in Fig. 4.11, resulting in *residual stress* in the damper.

Two Matlab programs, *rundamp.m* and *damp.m* are written in order to calculate the energy loss of the system over one cycle of the steel beam vibration[1]. Here, the initial energy is also calculated by multiplying the input force with the resulted deflection, if we assume a static loading of the beam from the initial position.

1. For the programs, see Appendix C.

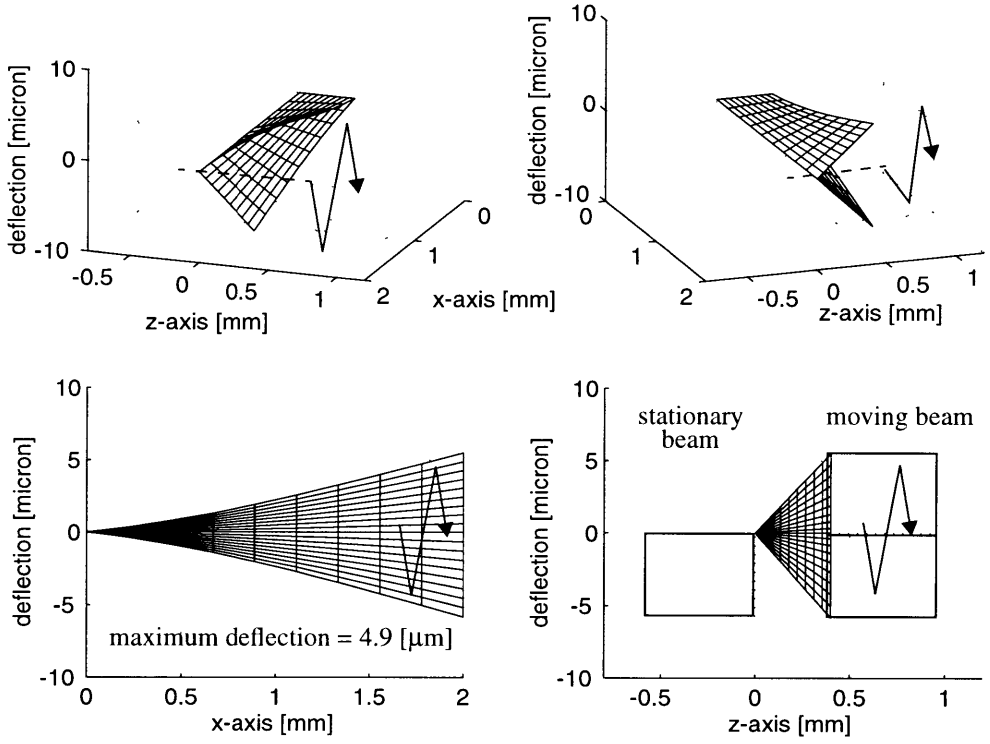

Figure 4.12: Damper Surface Deformation at 247 *N* Load

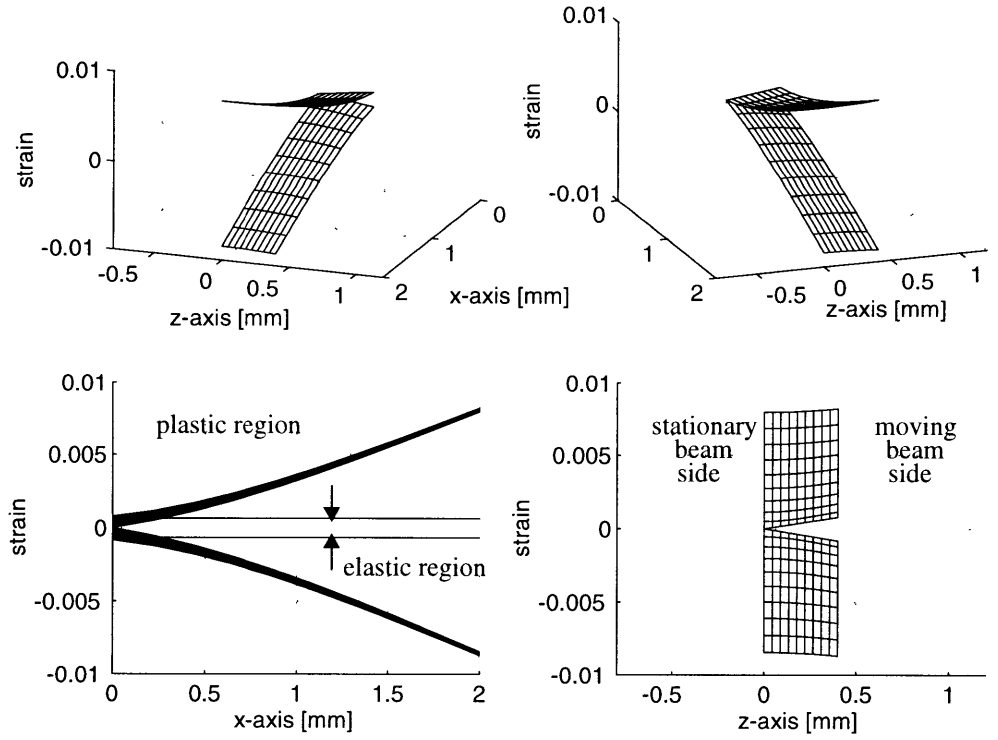

Figure 4.13: Damper Equivalent Strain at 247 *N* Load

First, shown in Figs. 4.12 and 4.13 are the surface deformation shape and corresponding strain value, calculated from Eqs. (4.15) and (4.18), with the damper thickness of 4 *mm* and the input load of 247 N[1]. According to Fig. 4.12, The maximum deflection of 4.9 μm occurs at the tip of the damper in the first downward deflection. The maximum deflection of 4.6 μm occurs at the same point in the second upward deflection.

As for the strain, according to Fig. 4.13, maximum strain of 0.0087, and 0.0082, is calculated at the tip of the damper in the cases of the downward and upward maximum deflection positions. The two lines in Fig. 4.13 indicates the critical elastic strain amount of 0.00067, and it is clear that most parts of the damper experiences plastic deformation, resulting in the energy loss of 22.6% per one cycle.

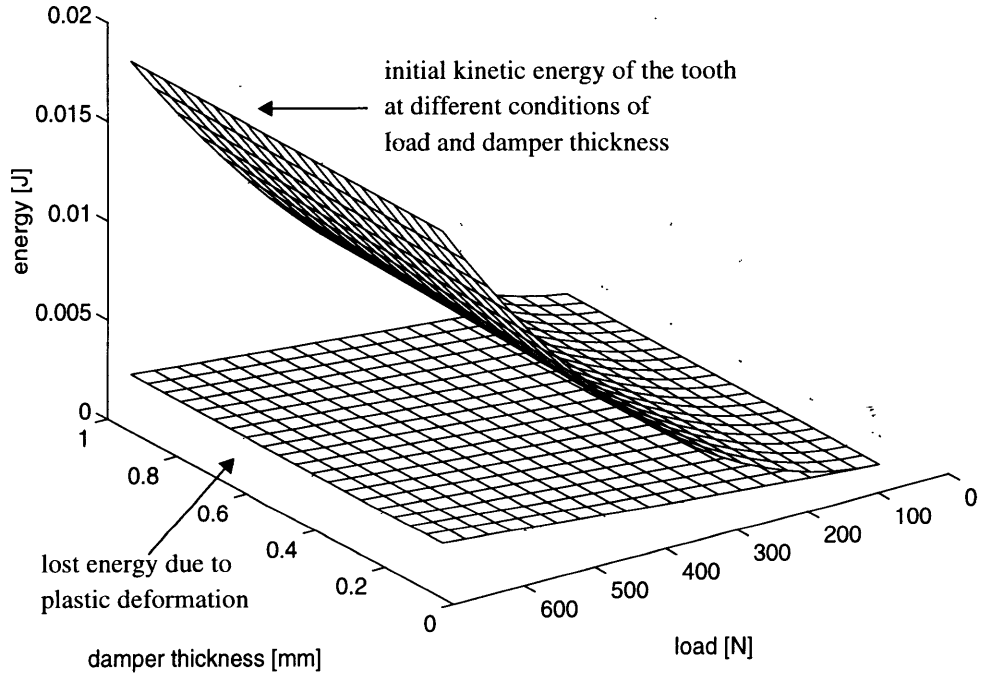

Figure 4.14: Input Energy and Energy Loss due to the Plastic Deformation

Shown in Fig. 4.14 is the input energy and energy loss due to the plastic deformation of the damper in various settings of the damper thickness and the input load. The maximum damper

1. This is drawn by another Matlab program, deflect247.m which is also presented in Appendix C. There are other figures of the damper surface deformation and strain graphs in Appendix C, for the cases when the damper thickness is 0.4 *mm* and the input force is 80 and 150 *N*.

thickness is chosen to be 1 *mm* or 50% of the gear beam thickness, and the minimum, 0.1 *mm* or 5%. The load varies between the maximum and minimum load calculated previously in Fig. 4.9.

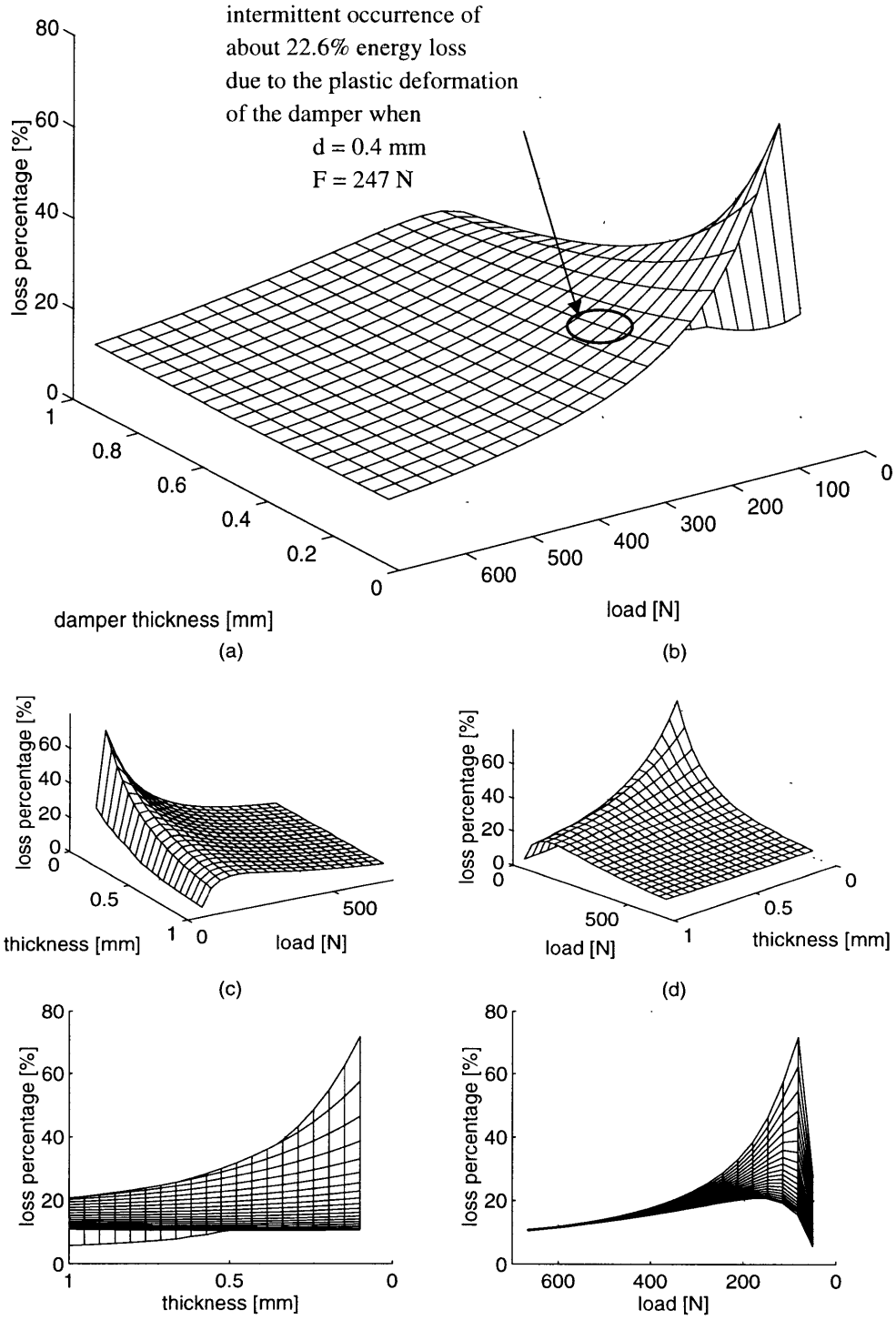

Figure 4.15: Energy Loss Percentage due to the Plastic Deformation of the Damper

Fig. 4.15 shows the energy loss percentage at different damper thicknesses and the input loads in different view points. Fig. 4.15 (c) shows the loss percentage versus the damper thickness, and Fig. 4.15 (d) shows the loss percentage versus the load.

The smaller the damper thickness, the more percentage of the input energy is lost during the deformation cycles according to Fig. 4.15. Although heavier loads induce more plastic energy to be lost, the lighter loads induce higher percentage of energy loss due to the non-linear stiffness of the steel beam.

One major weakness of this analysis lies in the assumption that the neighboring beam does not deflect at all, or in other terms, it does not experience any load from the input load. In reality, the load is carried to the neighboring beam through the deformation of the damper, resulting in less amount of the damper deformation than previously calculated. Therefore, the theoretical result of 22.6% energy loss is somewhat unrealistic. Yet, the analysis provides the general damping characteristics of bimetallic composite gear teeth, especially, the relationship among the damper thicknesses, the input loads, and the energy loss percentage

Therefore, the improvement of this analysis is to model the deflection of the beam more accurately. The first step would be to actually calculate the resistance force of the damper against the deflection of the loaded beam. This can be done iteratively by assuming a certain profile of deflection, and then calculating the resisting force of the damper using the strain values from the first assumed deflection. Then, a more accurate profile can be calculated with the revised loading conditions of the input load and resistant force. This method can be iterated to find the most realistic profile of the beam bending.

The same iterative method can be used in calculating the resulting deflection of the unloaded steel beam, and from these revised deflection profiles of the two neighboring steel beams, a more accurate estimation of plastic deformation, and therefore the energy loss can be calculated.

4.3 Experimental Analysis

4.3.1 Experimental Apparatus and Procedure

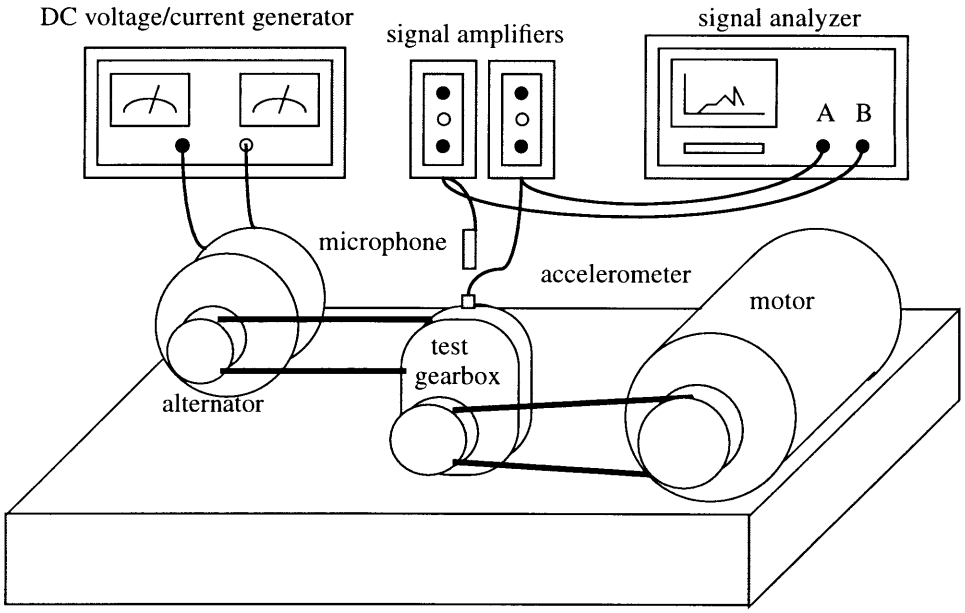

Figure 4.16: Experimental Apparatus for Bimetallic Helical Gears

Shown in Fig. 4.16, is the new experimental apparatus. A 1 *hp* DC motor is chosen for the input motor. V-belts are again used for all the power transmission among the components because they do not require precise alignments of the axes of the components.

An automobile alternator is used as the output load. Instead of generating electrical power from the mechanical motion, it is used as a mechanical brake. By supplying direct current into the stator of the alternator, magnetic fields are induced which resists any kind of rotational motion of the axis. Therefore, the load size is controlled by the input current supplied by a DC current generator.

The test gear has 49 teeth, and the pinion, 30 teeth. The input motor is connected to the gear of the test gears, and the loading alternator is connected to the pinion of the test gears, so that the gearbox is used as a speed increaser, which is the opposite of its intended use as a speed reducer.

Three pairs of gears are used for the experiment: one pair consisting of the original gear and the original pinion (OGOP), another of the composite gear and the composite pinion (CGCP), and the last of the original gear and the composite pinion (OGCP).

The vibration of the test gearbox is measured on top of the gearbox with an accelerometer, and the output signal is amplified by an AC-powered signal amplifier. The noise is measured using a microphone above the gearbox, and its output signal is amplified by a battery-powered signal amplifier. All the data are recorded using an Ono Sokki spectrum analyzer.

Table 4.7: Gear Rating for 601A Helical Gears

input speed	max input power	max input torque	max input tangential load on pinion	operating radius	
				gear	pinion
[*rpm*]	[*hp*]	[*lbf in*]	[*lbf*]	[*in*]	[*in*]
1750	4.3	157	245	1.05	0.64
1150	2.95	163	255		
[*Hz*]	[*Watt*]	[*Nm*]	[*N*]	[*mm*]	[*mm*]
29.17	3207	17.74	1090	26.7	16.3
19.17	2200	18.42	1134		

According to the specifications provided by Boston Gears in Table 4.7, the maximum torque that can be applied to the chosen 601A helical gears is about 160 *lbf in* or 18 *Nm*. With a 1 *hp* input motor, the maximum torque that can be applied to the gears is about 37 *lbf in* or 4.2 *Nm*, which is about 23% of the maximum rated torque; in terms of the tangential load, the rated maximum load is 1090 *N*, and the maximum load that can be applied to the test gears is about 57.5 *lbf* or 256 *N*.

This tangential load on the gear teeth is coupled to the running speed of the test by the proportional relationship according to DC motor characteristics[1]. Therefore, rotational speed are used for the experiment settings.

Seven different settings are used in the experiment. The gears are run in 610, 850, 1100, 1350, 1600, 1850, and 2100 *rpm*, with corresponding mesh frequencies (MF's) at, 500, 700, 900, 1100, 1300, 1500, and 1700 *Hz*. In terms of the percentile with respect to the maximum tangential load of 1090 N, or maximum load percentile (MLP), the settings are 6.1, 8.5, 11, 13.5, 16, 18.5, 21%, and they are 67, 94, 121, 149, 176, 204, and 231 *N*, respectively.

Shown in Table 4.8 is the key frequency components of the experimental settings of MF, SF and BF. Both gear and pinion axes have two ball bearings each with 7 balls.

1. For more explanation on DC motor characteristic, see Appendix A.2 Motor Drive.

Table 4.8: Key Frequency Components in the Experimental Results

Fig.	max load percentage (MLP) [%]	mesh frequency (MF) [Hz]	shaft frequency (SF) [Hz]		bearing frequency (BF) [Hz]	
			Pinion	Gear	Pinion	Gear
4.17	6.1	500	10.2	16.3	71.2	113.9
4.18	8.5	700	11.7	18.7	99.2	158.7
4.19	11	900	15	24	128.3	205.3
4.20	13.5	1100	18.3	29.3	157.5	252
4.21	16	1300	21.7	34.7	186.7	299
4.22	18.5	1500	25	40	215.8	345.3
4.23	21	1700	28.3	45.3	245	392

4.3.2 Experimental Results

The experimental data are presented in seven figures for each setting of MF and MLP, each consisting of four graphs. For all seven figures, from Figs. 4.17 to 4.23, the vibration and the noise data of OGOP and CGCP are presented in graphs (a) and (b). Graphs (c) and (d) show those of OGOP and OGCP. All the OGOP data are represented with dotted lines, and those of CGCP and OGCP are indicated in solid lines. Graphs (a) and (c) on the left side are the vibration data, and graphs (b) and (d) on the right side show the noise data. Again, throughout the graphs, the harmonics of the MF are indicated by integers corresponding to the harmonic numbers, and the known noise is indicated with the arrows.

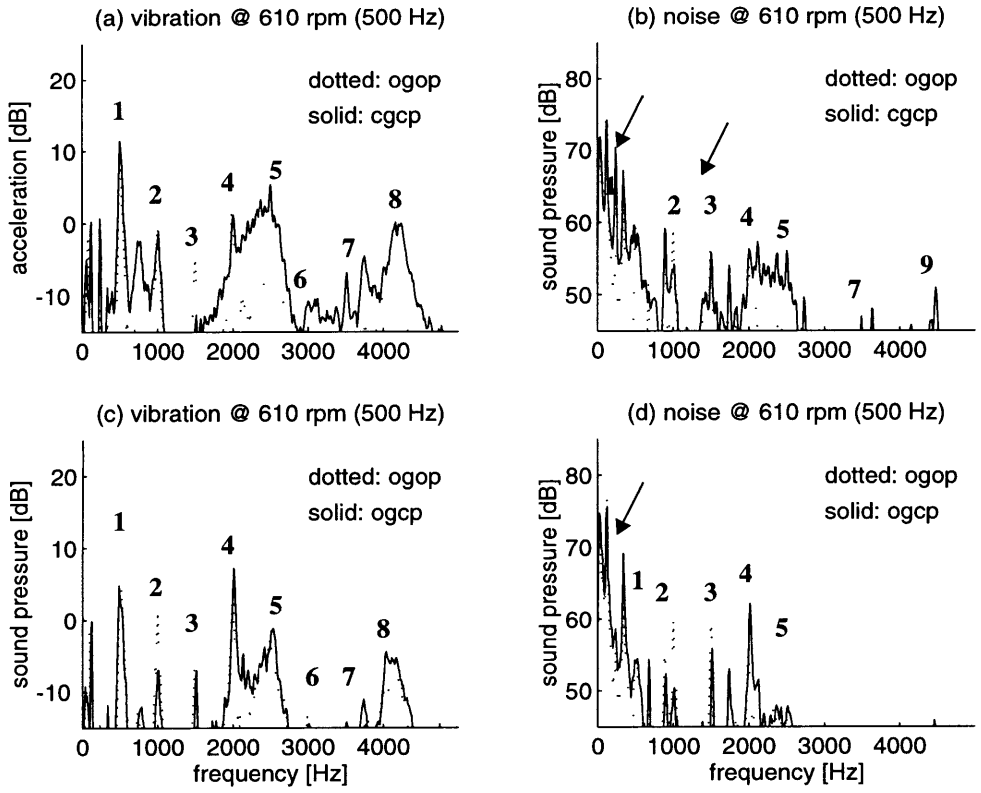

Figure 4.17: Vibration and Noise Frequency Spectra of Helical Gears at 6.1% MLP

Fig. 4.17 shows the vibration and noise frequency spectra of helical gears of all three gear sets of OGOP, CGCP, and OGCP at the load setting of 6.1% MLP, running at 610 *rpm* with 500 *Hz* MF. The tangential load that is applied to the gear teeth is 67 *N*. Both the vibration and noise data show clear MF components of 500 *Hz* and their harmonics. The comparison of the OGOP data with both CGCP and OGCP shows that OGOP has much more distinctive frequency signals. This is because the surface finish of OGOP is better than that of CGCP or OGCP due to the unavoidable surface refinish process after the soldering is performed for CGCP and OGCP.

Comparison between the data of CGCP and OGOP in graphs (a) and (b) indicates that the vibration and noise level of CGCP is higher than that of OGOP, implying that there is no damping advantage of using CGCP. This is because CGCP has slits on both the gear and the pinion; the slits of the pinion and gears are supposed to match one another, yet, mismatch among them is unavoidable due to the modification error, resulting in discrete gear impacts across the gear face, raising vibration and noise level.

However, OGCP shows a damping effect on both vibration and noise level from OGOP. The first three harmonics of MF of graph (c) shows the vibration level drop of 3 to 6 dB. Also the noise

data of graph (d), shows again 3 to 8 dB drop in sound pressure level at the first three harmonics of MF.

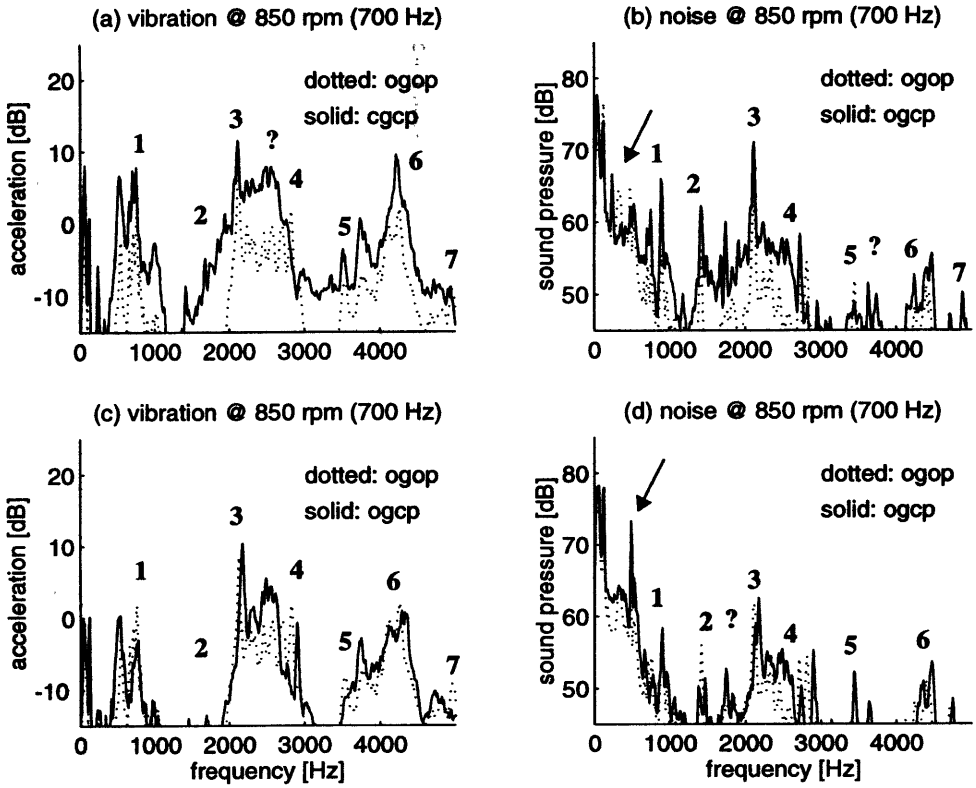

Figure 4.18: Vibration and Noise Frequency Spectra of Helical Gears at 8.5% MLP

Shown in Fig. 4.18 is the frequency and noise spectra of test gear sets of at 8.5% MLP, running at 700 *Hz* MF. Again indicated in graphs (a) and (b), the vibration and noise level of CGCP is greater than those of both OGOP and OGCP. The reduction level of OGCP is smaller compared to the previous case, showing small damping effect only at the fundamental MF of graph (c). As for the noise level, only the second harmonic frequency of MF shows about 6 dB drop in graph (d). There are some other peculiar peaks that exist at around 500, 2500, and 4300 *Hz*.

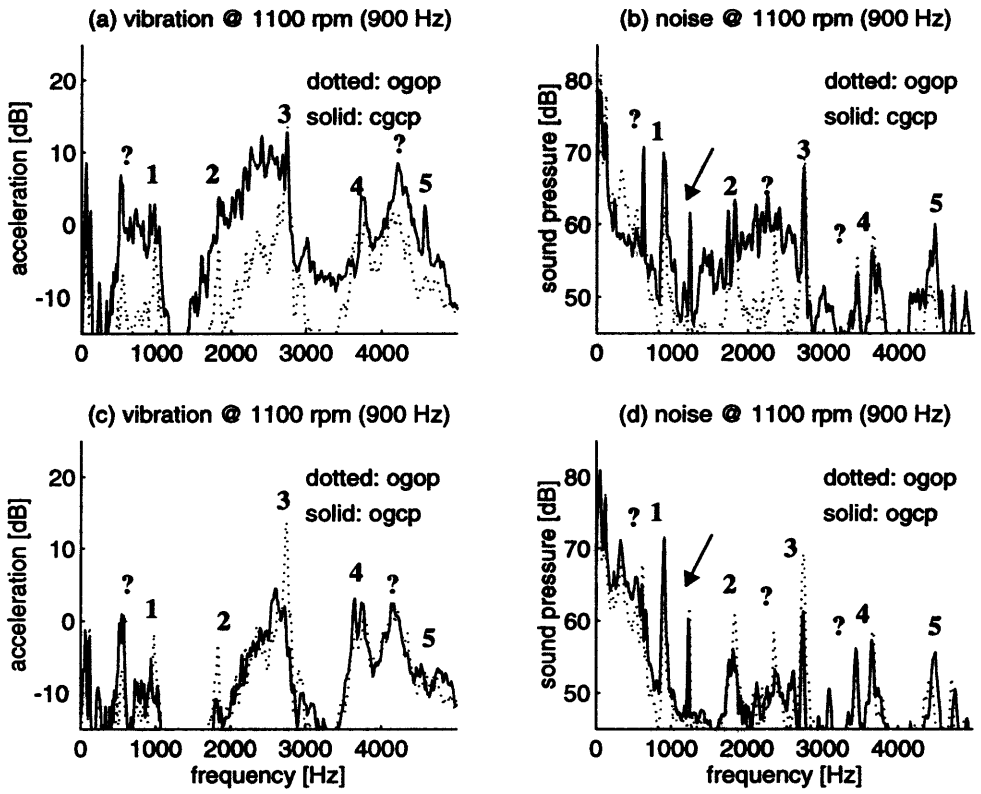

Figure 4.19: Vibration and Noise Frequency Spectra of Helical Gears at 11% MLP

Fig. 4.19 shows the resulting vibration and noise frequency spectra of all the gear sets at 11% MLP at 900 *Hz* MF. OGCP does indicate some improvements in the vibration damping especially at the third harmonic of MF in graph (c). Again, it is shown that there exist peaks at near 500, 2500, and 4300 *Hz*.

The following Figs. 4.20, 4.21, 4.22, and 4.23 shows the frequency spectra of the test gear sets at 13.5, 16, 18.5, and 21% MLP. There exist strong frequency response in the ranges of between 200 and 1000 *Hz*, between 2000 and 3400 *Hz*, and between 3500 and 4500 *Hz*, which are most likely originated from the selective frequency filtering by the resonance characteristics of the experimental setup itself.

Other signals originating from the axis rotation of motor, gears, and the alternator as well as the vibration of the rubber v-belts are expected to be in the experimental data, which might be the causes of the dominant peaks at 500, 2700, and 4200 Hz.

In summary, OGCP shows drops in both vibration and noise level of 3 to 5 *dB* harmonic frequencies of MFls.

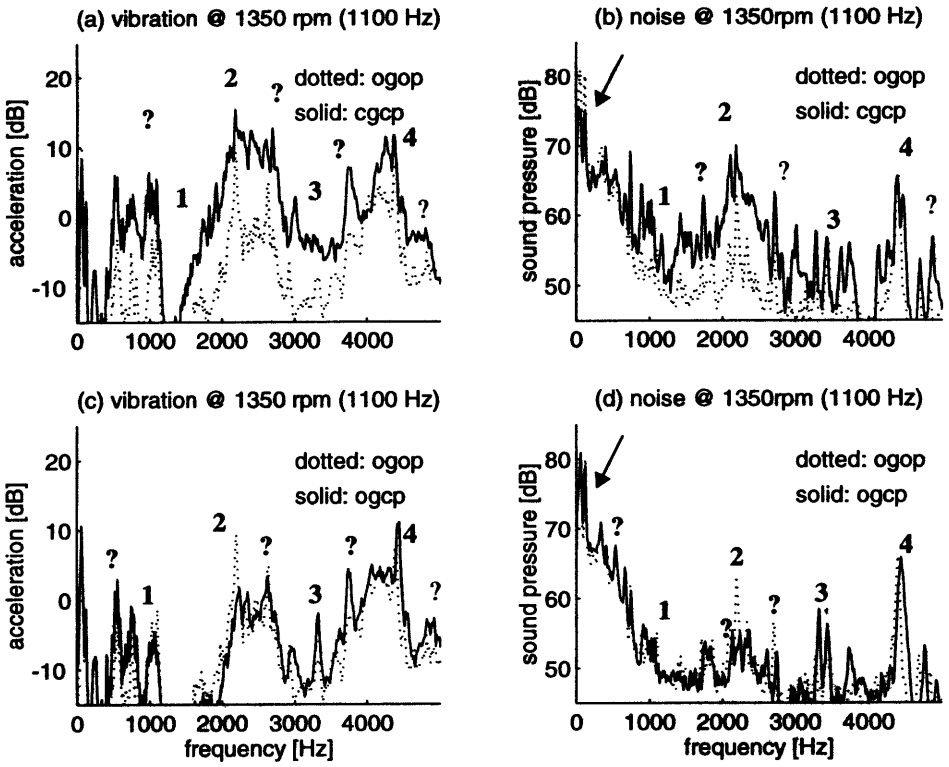

Figure 4.20: Vibration and Noise Frequency Spectra of Helical Gears at 13.5% MLP

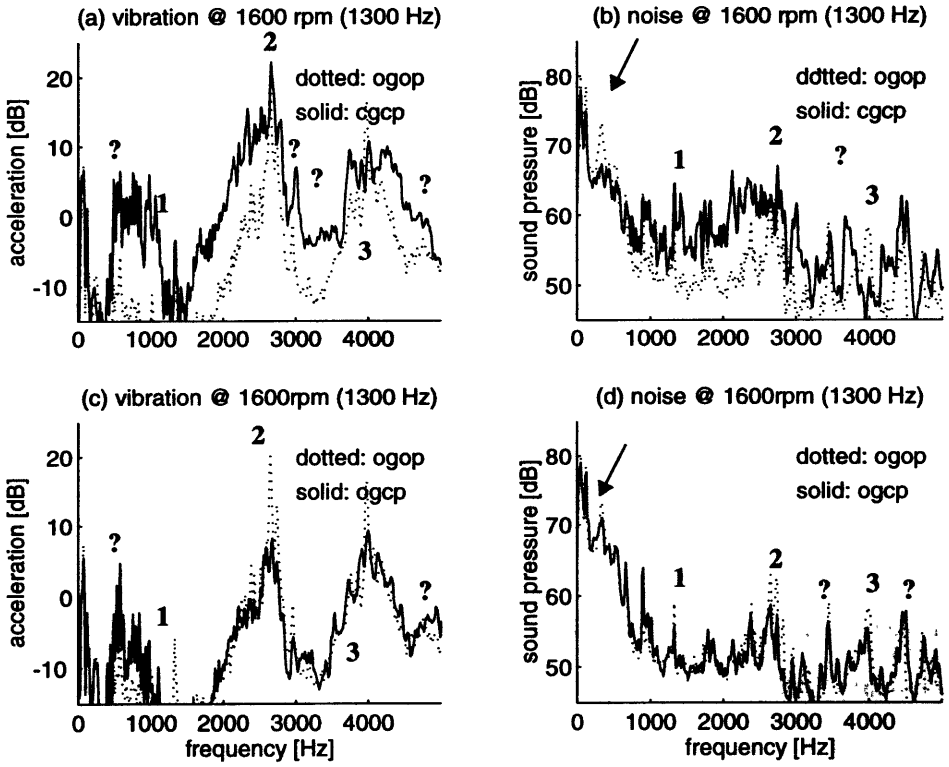

Figure 4.21: Vibration and Noise Frequency Spectra of Helical Gears at 16% MLP

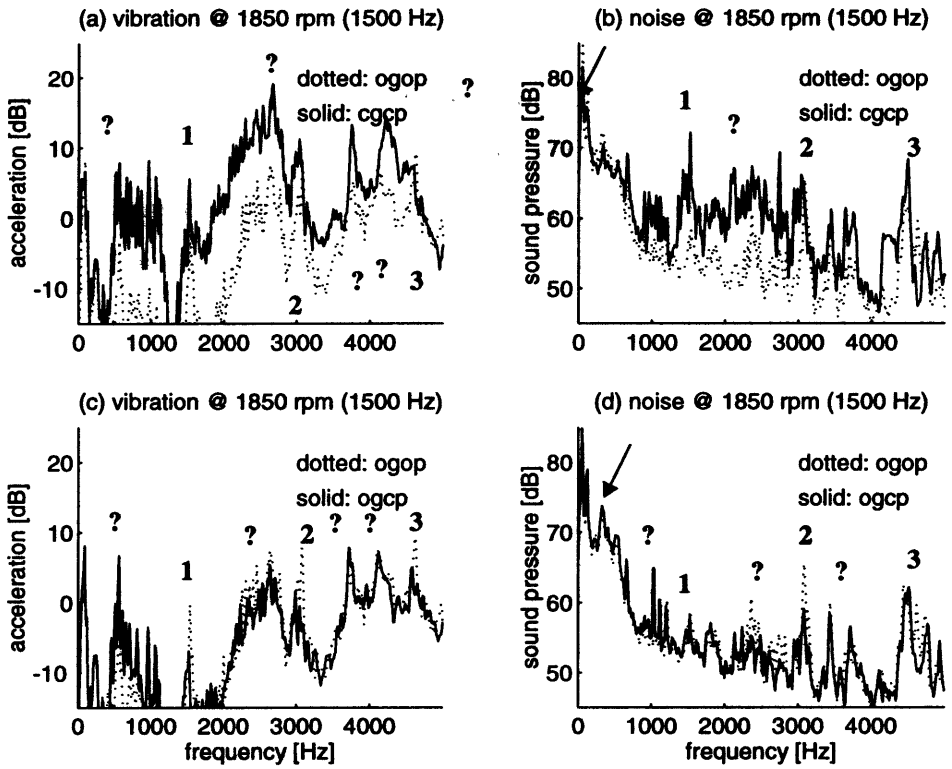

Figure 4.22: Vibration and Noise Frequency Spectra of Helical Gears at 18.5% MLP

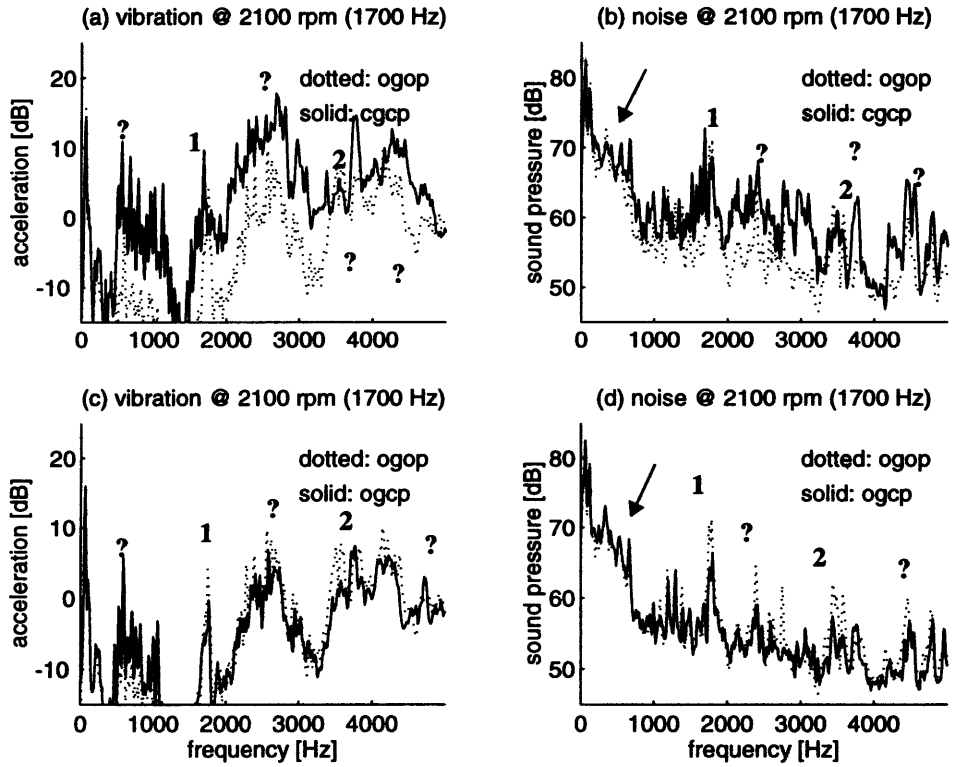

Figure 4.23: Vibration and Noise Frequency Spectra of Helical Gears at 21% MLP

4.4 Conclusions

Theoretically, energy loss per one deflection cycle is calculated using a basic theory of beam bending and stress/strain analysis. 22.5% of energy loss is calculated for the modeled case of the damper of 2 *mm* by 2 *mm* by 0.4 *mm*. This energy loss percentage is accessed as very high due to the assumption that the neighboring unloaded beam does not experience any load from the deflection of the damper. If we consider the deflection of the neighboring beam, the deflection difference between the two steel beams is smaller than the theoretical value.

However, a basic damping characteristic is defined by the analysis that the energy loss percentage is inversely proportional to the size of the damper thickness and the amount of the load on gears.

As for the experimental analysis, the vibration and noise level of CGCP turns out to be worse than that of OGOP due to the mismatches of the slits as gears mesh. Nevertheless, the data of OGCP indicates about 3 to 5 dB damping effect in both vibration and noise level at certain harmonics of the fundamental MF's.

Throughout all the experiments, there exist several frequency components, which is not related to MF's. These components are possibly from SF's and/or BF's or even from the surface finish or other sources which are unknown at this point. Also, the selective frequency filtering of the experimental setup makes the source identification difficult, indicating that more rigorous investigation on the dynamics of experimental setup is need.

Chapter 5

Investigation on Bimetallic Composite Beam

5.1 Bimetallic Composite Beam

In the previous cyclic energy-loss analysis, plastic deformation of the damper was assumed, based on the premise that the stiffness of the tin layer is negligible; however, the stiffness of the tin layer does carry the load to the neighboring unloaded beam. This reduces the amount of the damper deformation, and therefore the damper may not experience any plastic deformation. Yet, even in the elastic region, hysteresis damping occurs due to the internal friction as the material deforms, and it is expected that the high internal hysteretic damping of the tin damper layer will reduce the vibration energy.

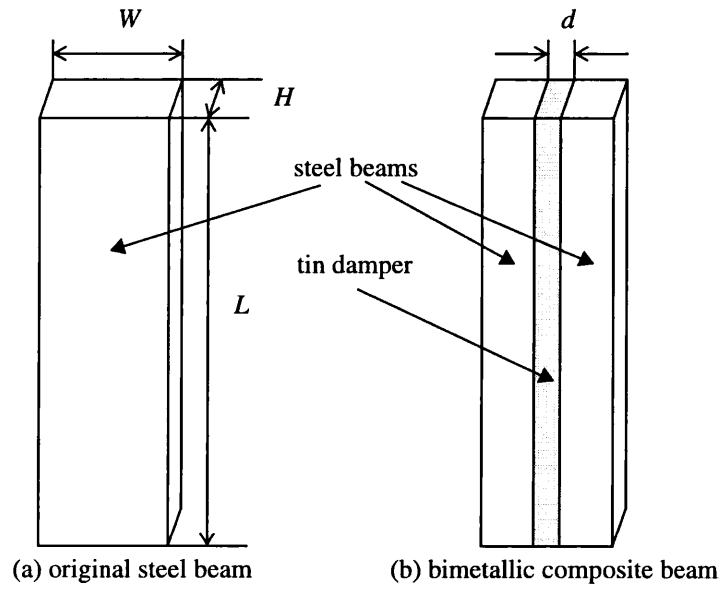

Figure 5.1: The Original Steel Beam and the Composite Bimetallic Beam

Hence, two beam structures are made in order to model the gear teeth. One structure is a steel beam, representing the original, conventional gear tooth, and the other consists of two steel beams soldered by one narrow strip of tin layer, representing a composite bimetallic gear tooth as shown in Fig. 5.1[1].

1. For the picture of the beam, see Appendix D.

Table 5.1: Dimensions of the Bimetallic Composite Beam

item	symbol	value
length [m]	L	$177.8\text{x}10^{-3}$
height [m]	H	$9.398\text{x}10^{-3}$
width [m]	W	$29.5\text{x}10^{-3}$
width of Gap [m]	d	$5.46\text{x}10^{-3}$

5.2 Theoretical Analysis

5.2.1 Vibration of Non-Slender Beam

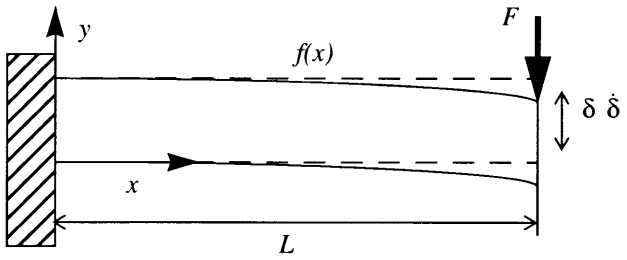

Figure 5.2: Vibration of a Non-Slender Beam

First, the vibration of the test beam structure needs to be identified. From the previous discussion in Chapter 4, the deflection y of a non-slender beam structure can be calculated by Eq. (4.9),

$$y(F,x) = \delta(F)\cdot f(x) = \left(\frac{FL^3}{3EI_b} + \frac{\eta FL}{A_bG}\right)\cdot\left[\frac{-A_bGx^3 + 3A_bG_sLx^2 + 6E_sI_bx}{2(A_bG_sL^3 + 3\eta E_sI_bL)}\right] \quad .$$

where $\delta(F)$ is the deflection at the tip, and $f(x)$ is the profile function which describes the bending shape of the beam. Even though the test beams are slender beams, the bending equation of a non-slender beam is used in future applications of the analysis to the non-slender gear teeth.

If we assume that the velocity profile is the same as the displacement profile $f(x)$, the velocity $\frac{\partial y}{\partial t}$ becomes,

$$\frac{\partial}{\partial t}y(F,x) = \dot{\delta}(F)\cdot f(x) = \dot{\delta}(F)\cdot\left[\frac{-A_bG_sx^3 + 3A_bG_sLx^2 + 6E_sI_bx}{2(A_bG_sL^3 + 3\eta E_sI_bL)}\right], \tag{5.1}$$

where $\dot{\delta}$ is the velocity of the beam at its tip. Then, the kinetic energy of the system can be calculated [13],

$$T^* = \frac{\dot{\delta}^2}{2} \cdot m_{orig} = \frac{\rho_s A_b}{2}\int_0^L \left(\frac{\partial y}{\partial t}\right)^2 dx = \frac{\dot{\delta}^2}{2} \cdot \frac{\rho_s A_b\left\{\frac{33}{35}A_b^2 G_s^2 L^7 - \frac{33}{5}A_b G_s \eta E_s I_b L^5 + 12\eta^2 E_s^2 I_b^2 L^3\right\}}{4(A_b G_s L^3 + 3\eta E_s I_b)^2}. \quad (5.2)$$

The potential energy of the system can also be calculated,

$$V = \frac{\delta^2}{2} \cdot k_{orig} = \frac{E_s I_b}{2}\int_0^L \left(\frac{\partial \delta}{\partial x}\right)^2 dx = \frac{\delta^2}{2} \cdot \frac{E_s I_b (12 A_b^2 G_s^2 L^3)}{4(A_b G_s L^3 + 3\eta E_s I_b)^2}, \quad (5.3)$$

And applying Eqs. (5.1) and (5.2) to the Lagrange's Equation,

$$\Pi = T^* - V; \frac{d}{dt}\left(\frac{\partial \Pi}{\partial \dot{\delta}}\right) - \frac{\partial \Pi}{\partial \delta} = \Xi, \quad (5.4)$$

with the non-conservative generalized force Ξ of friction force, $c\dot{\delta}$, and harmonic input force, $F_o \cos \omega t$ at the input frequency of ω,

$$\Xi = -c\dot{\delta} + F_o \cos \omega t, \quad (5.5)$$

the equation of the motion is established,

$$m\ddot{\delta} + c\dot{\delta} + k\delta = F_o \cos \omega t, \quad (5.6)$$

where m and k are equivalent mass and equivalent stiffness of the system defined in Eqs. (5.2) and (5.3). Here c is the damping constant, and it is related to the damping coefficient ζ, as follows [13],

$$\frac{c}{\zeta} = 2\sqrt{mk}. \quad (5.7)$$

For the composite beam structure, because it consists of two narrow steel beams and one tin damper, the equivalent Young's modulus E_{eq} and equivalent shear modulus G_{eq} should be used for the analysis. This can be calculated by the following equations,

$$E_{eq} = \frac{E_s I_s + E_t I_t}{I_b}; A_{eq} = \frac{G_s A_s + G_t A_t}{A_b}, \quad (5.8)$$

$$I_s = \frac{(W-d)H^3}{12}, I_t = \frac{dH^3}{12}, I_b = \frac{WH^3}{12}, \quad (5.9)$$

$$A_s = (W-d)H, A_t = dH, A_b = WH, \quad (5.10)$$

where E_t and G_t are Young's modulus and shear modules of the tin damper[1], and I_t and A_t, the moment and the cross-sectional area of the tin damper, and I_s and A_s are the moment and the cross-sectional area of the steel beams of the composite beam.

1. All the material constants of tin and steel are listed previous in Table 4.6.

Therefore, the equivalent mass m_{comp} and the stiffness k_{comp} for the composite beam are,

$$m_{comp} = \frac{\rho_{eq}A_b\left\{\frac{33}{35}A_b^2G_{eq}^2L^7 - \frac{33}{35}A_bG_{eq}\eta E_{eq}I_bL^5 + 12\eta^2E_{eq}^2I_b^2L^3\right\}}{4(A_bG_{eq}L^3 + 3\eta E_{eq}I_b)^2}, \text{ and} \tag{5.11}$$

$$k_{comp} = \frac{E_{eq}I_b(12A_b^2G_{eq}^2L^3)}{4(A_bG_{eq}L^3 + 3\eta E_{eq}I_b)^2}. \tag{5.12}$$

where ρ_{eq} is the equivalent density of the composite beam structure, which can be calculated,

$$\rho_{eq} = \frac{\rho_sA_s + \rho_tA_t}{A_b}. \tag{5.13}$$

Also, using the above equations, the resonant frequency or the natural frequency of the beams can be calculated,

$$f^2{}_{resonant} = \frac{1}{(2\pi)^2}\cdot\frac{k}{m} = \frac{1}{(2\pi)^2}\cdot\frac{E_{eq}I_b(12A_b^2G_{eq}^2L^3)}{\rho_{eq}A_b\left\{\frac{33}{35}A_b^2G_{eq}^2L^7 - \frac{33}{35}A_bG_{eq}\eta E_{eq}I_bL^5 + 12\eta^2E_{eq}^2I_b^2L^3\right\}}, \tag{5.14}$$

and all the values of this analysis are listed in Table 5.2.

Table 5.2: Key Values for the Equations of Motion

item	symbol	value
total area	A_b	277.2x10^{-6} [m^2]
total moment	I_b	2.04x10^{-9} [m^4]
steel area	A_s	225.9x10^{-6} [m^2]
steel moment	I_s	1.66x10^{-9} [m^4]
tin area	A_t	51.3x10^{-6}[m^2]
tin moment	I_t	0.38x10^{-9} [m^4]
equivalent density	ρ_{eq}	7.84x10^3 [kg/m^3]
equivalent Young's modulus	E_{eq}	172x10^9[N/m^2]
equivalent shear modulus	G_{eq}	66.3x10^9 [N/m^2]
equivalent mass	m_{orig}	87.4x10^{-3} [kg]
	m_{comp}	87.8x10^{-3} [kg]
equivalent stiffness	k_{orig}	211x10^3 [N/m]
	k_{comp}	182x10^3 [N/m]

Table 5.2: Key Values for the Equations of Motion

item	symbol	value
$\frac{\text{damping constant}}{\text{damping coefficient}}$	$\frac{c_{orig}}{\xi_{orig}}$	271.3 [*Ns/m*]
	$\frac{c_{comp}}{\xi_{comp}}$	252.7 [*Ns/m*]
resonant frequency	$f_{resonant,\ orig}$	248 [*Hz*]
	$f_{resonant,\ comp}$	229 [*Hz*]

5.2.2 Vibration Response of Beam under Harmonic Force

If the harmonic forcing $F(t) = F_0 \cos wt$ is applied to the equation of motion, as in Eqs. (5.6), the particular solution of deflection X_p is also expected to be harmonic,

$$x_p(t) = X\cos(\omega t - \phi), \tag{5.15}$$

where X and ϕ are

$$X = \frac{F_0}{[(k - m\omega^2)^2 + c^2\omega^2]^{1/2}};\ \phi = \tan^{-1}\left\langle \frac{c\omega}{k - m\omega^2} \right\rangle. \tag{5.16}$$

Then, the undamped natural frequency and the damping coefficient become

$$\omega_n = 2\pi f_{resonant} = \sqrt{\frac{k}{m}};\ \zeta = \frac{c}{c_c} = \frac{c}{2m\omega_n} = \frac{c}{2\sqrt{mk}};\quad \frac{c}{m} = 2\zeta\omega_n. \tag{5.17}$$

Using the static deflection under the static force F_0,

$$\delta_{st} = \frac{F_0}{k}, \tag{5.18}$$

and the frequency ratio of

$$r = \frac{\omega}{\omega_n}, \tag{5.19}$$

we obtain the following equations

$$\frac{X}{\delta_{st}} = M = \frac{1}{\left\{\left[1 - \left(\frac{\omega}{\omega_n}\right)^2\right]^2 + \left[2\zeta\frac{\omega}{\omega_n}\right]^2\right\}^{1/2}} = \frac{1}{\sqrt{(1 - r^2)^2 + (2\zeta r)^2}}; \tag{5.20}$$

$$\phi = \tan^{-1}\left\{\frac{2\zeta\frac{\omega}{\omega_n}}{1-\left(\frac{\omega}{\omega_n}\right)^2}\right\} = \tan^{-1}\left\langle\frac{2\zeta\frac{\omega}{\omega_n}r}{1-r^2}\right\rangle, \tag{5.21}$$

where the quantity M is called the *magnification factor, amplification factor,* or *amplitude ratio.*

For $0 < \zeta < \frac{1}{\sqrt{2}}$, the maximum value of M occurs when

$$r = \sqrt{1-2\zeta^2} \text{ or } \omega = \omega_n\sqrt{1-2\zeta^2}, \tag{5.22}$$

which can be seen to be lower than the undamped natural frequency ω_n and the damped natural frequency $\omega_d = \omega_n\sqrt{1-2\zeta^2}$. The maximum value of X (when $r = \sqrt{1-2\zeta^2}$) is given by

$$\left(\frac{X}{\delta_{st}}\right)_{max} = \frac{1}{2\zeta\sqrt{1-\zeta^2}}, \tag{5.23}$$

and the value of X at $\omega = \omega_n$ by

$$\left(\frac{X}{\delta_{st}}\right)_{\omega=\omega_n} = \frac{1}{2\zeta}, \tag{5.24}$$

which means that, in a vibration test, if the maximum amplitude of the response and static deflection under the static load are measured, the damping ratio of the system can be found using Eq. (5.24).

For small values of damping ($\zeta < 0.05$), we can assume,

$$\left(\frac{X}{\delta_{st}}\right)_{max} \cong \left(\frac{X}{\delta_{st}}\right)_{\omega=\omega_n} = \frac{1}{2\zeta} = Q. \tag{5.25}$$

The value of the amplitude ratio at resonance is also called Q factor or quality factor of the system. The points R_1 and R_2, where the amplification factor falls to $Q/\sqrt{2}$, are called half power points because the power absorbed (ΔW) by the damper, responding harmonically at a given frequency, is proportional to the square of the amplitude:

$$\Delta W = \pi c\omega X^2. \tag{5.26}$$

To obtain the difference between the frequencies associated with the half power points R_1 and R_2, we set $X/\delta_{st} = Q/\sqrt{2}$ so that

$$\frac{1}{\sqrt{(1-r^2)^2+(2\zeta r)^2}} = \frac{Q}{\sqrt{2}} = \frac{1}{2\sqrt{2}\zeta} \text{ or } r^4 - r^2(2-4\zeta^2) + (1-8\zeta^2) = 0. \tag{5.27}$$

Then, the solution gives

$$r_{1,2}^2 = 1 - 2\zeta^2 \pm 2\zeta\sqrt{1+\zeta^2}, \tag{5.28}$$

and for small values of ζ, it can be approximated as

$$r_{1,2}^2 = R_{1,2}^2 = \left(\frac{\omega_{1,2}}{\omega_n}\right)^2 = 1 \pm 2\zeta, \tag{5.29}$$

where $\omega_{1,2} = \omega|_{R_1,R_2}$. Using the relation

$$\omega_2^2 - \omega_1^2 = (\omega_2 + \omega_1)(\omega_2 - \omega_1) = (R_2^2 - R_1^2) \cong 4\zeta\omega_n^2, \text{ and} \tag{5.30}$$

$$\omega_2 + \omega_1 = 2\omega_n, \tag{5.31}$$

we can find the bandwidth $\Delta\omega$ given by

$$\Delta\omega = \omega_2 - \omega_1 \cong 2\zeta\omega_n \tag{5.32}$$

Combining Eqs. (5.25) and (5.32), we obtain

$$Q \cong \frac{1}{2\zeta} \cong \frac{\omega_n}{\omega_2 - \omega_1} \tag{5.33}$$

It can be seen that the quality factor Q can be used for estimating the equivalent viscous damping in a mechanical system, which is the natural frequency divided by the bandwidth of the half power points.

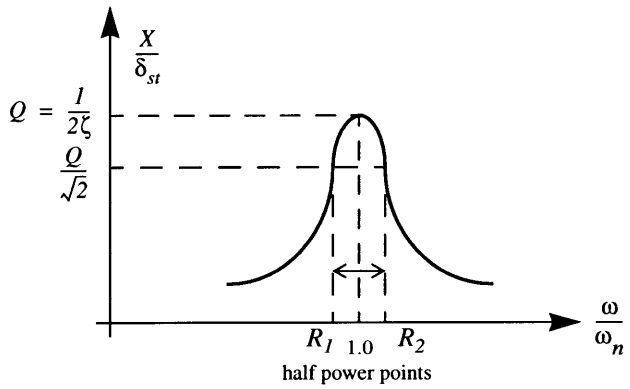

Figure 5.3: Harmonic Response Curve showing Half Power Points and Bandwidth [13]

Therefore, from the half power points of the harmonic response curve, or the *transmissibility curve*, the damping coefficient of each beam can be evaluated using Eq. (5.33). With Eqs. (5.7), (5.11), and (5.12), the equation of motion of both beam can be defined.

5.3 Experimental Analysis

5.3.1 Experimental Apparatus and Procedure

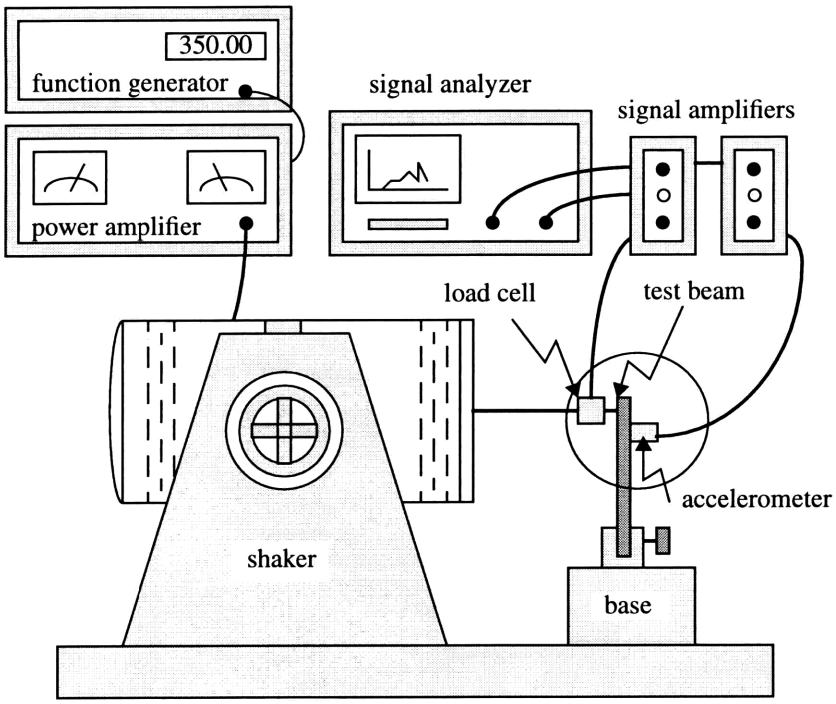

Figure 5.4: Shaker Experimental Apparatus

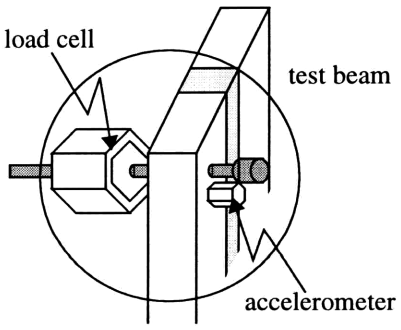

Figure 5.5: Magnified View of the Test Beam Connection to the Shaker

Shown in Fig. 5.4 is the experimental apparatus to measure the damping coefficients of the test beams. Each of the beams are connected to the shaker through a load cell or a force transducer for the measurement of the input force, and an accelerometer is attached to each beam as shown in Fig. 5.5 to measure the output displacement.

The shaker is run by a signal generator. However, before the shaker experiment, a hammer experiment is performed in order to locate the approximate range of the resonant frequency of each

beam. Then, the response of the frequency range above and below 100 *Hz* are measured near the recorded resonant frequency.

5.3.2 Experimental Results

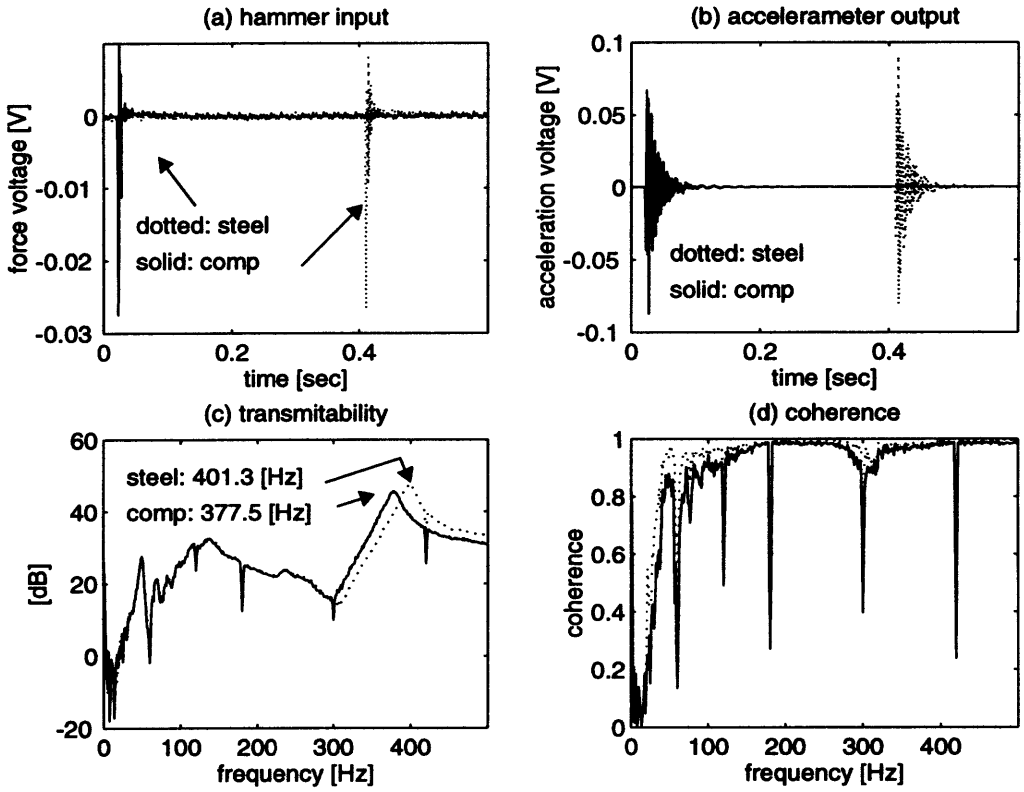

Figure 5.6: Hammer Result for Steel Beam and Bimetallic Beam

First, shown in Fig. 5.6 is the result of the hammer experiment. The steel beam data are plotted with dotted lines and the composite beam data are plotted with solid lines. Graph (a) shows the input impact force from the force transducer which is attached to the hammer head. According to the graph, the impact occurs at time 0.02 second for the steel beam and at 0.41 second for the bimetallic beam. The response signals of the accelerometer output in graph (b) also agree on the timing of the impact. In graph (c), the transmissibility curve shows that the resonant frequency of steel beam lies at around 400 *Hz* and that of the bimetallic composite beam, at 380 *Hz*. Therefore, the shaker experimental frequency range has been set between 300 *Hz* and 400 *Hz* considering the fact that the hammer experiment tends to bring up the natural frequency.

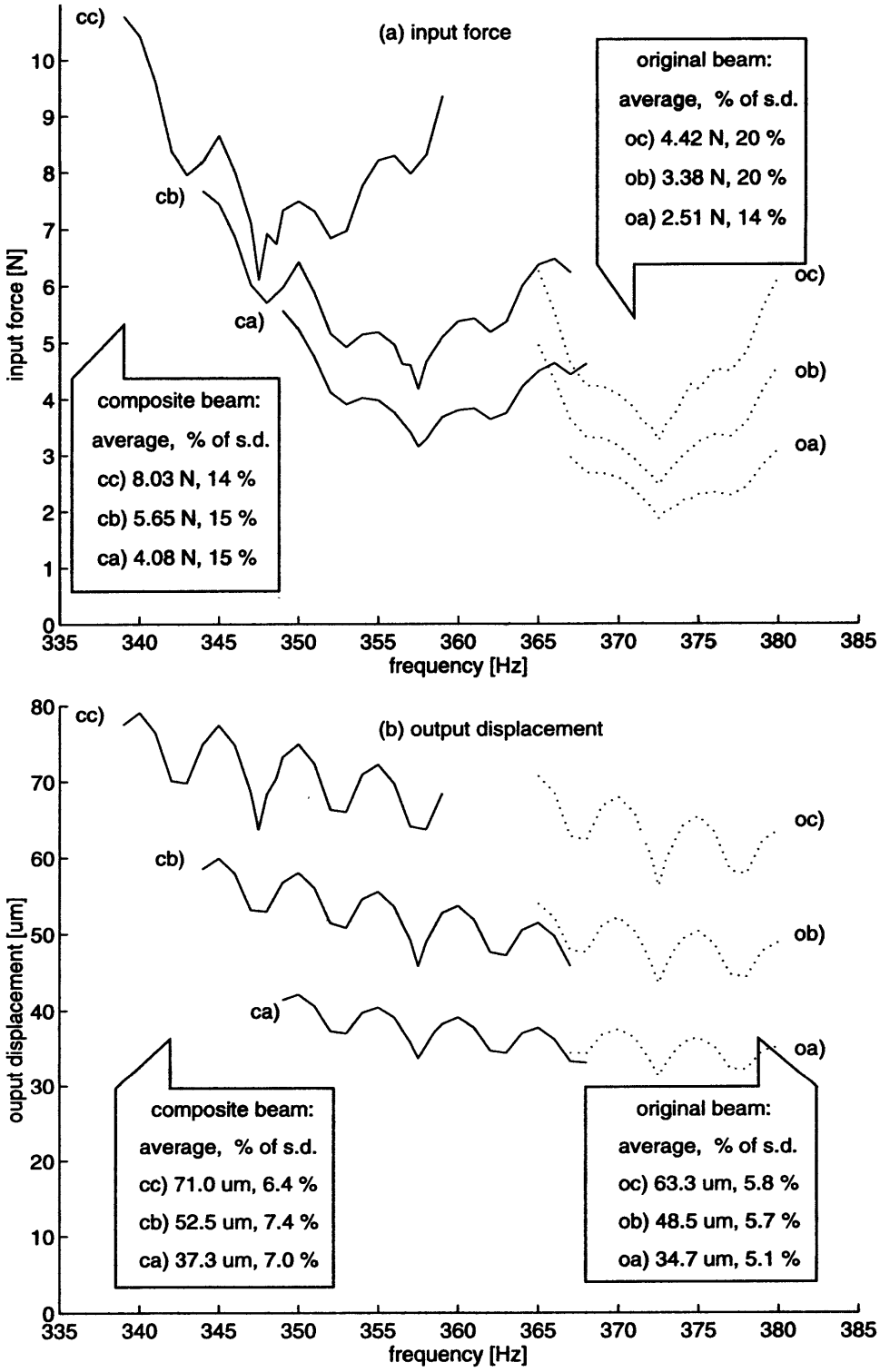

Figure 5.7: Input Force and Output Displacement of the Vibration of Test Beams

Shown in Fig. 5.7 is the input force and the output displacement of the shaker experiment. Three different force settings are used for each beam; the dotted lines indicate the input force of the steel beam, and the solid lines, that of the bimetallic beam. Note that about 2 to 5 N force are applied to the steel beam, and 4 to 8 N of force is applied to the composite beam with a standard deviation of 15 to 20% of the average force, as shown in graph (a). If we compare the input force data with the displacement data in graph (b) of the 5 to 8% standard deviation, it is clear that the displacement is fixed at around 35 to 65 μm for the steel beam and at 75 μm for the composite beam, and the size of the input force has been changed as forcing frequency changes.

Even though the displacement is about the same for the steel and bimetallic beams, nearly one half of the input force amount is recorded for the composite beam. This indicates that the stiffness of the composite beam is much weaker than that of the steel beam. Also, a large frequency shift of the force and displacement of the composite beam as the size of the load changes, indicates a non-linear relationship between the load and the resonant frequency.

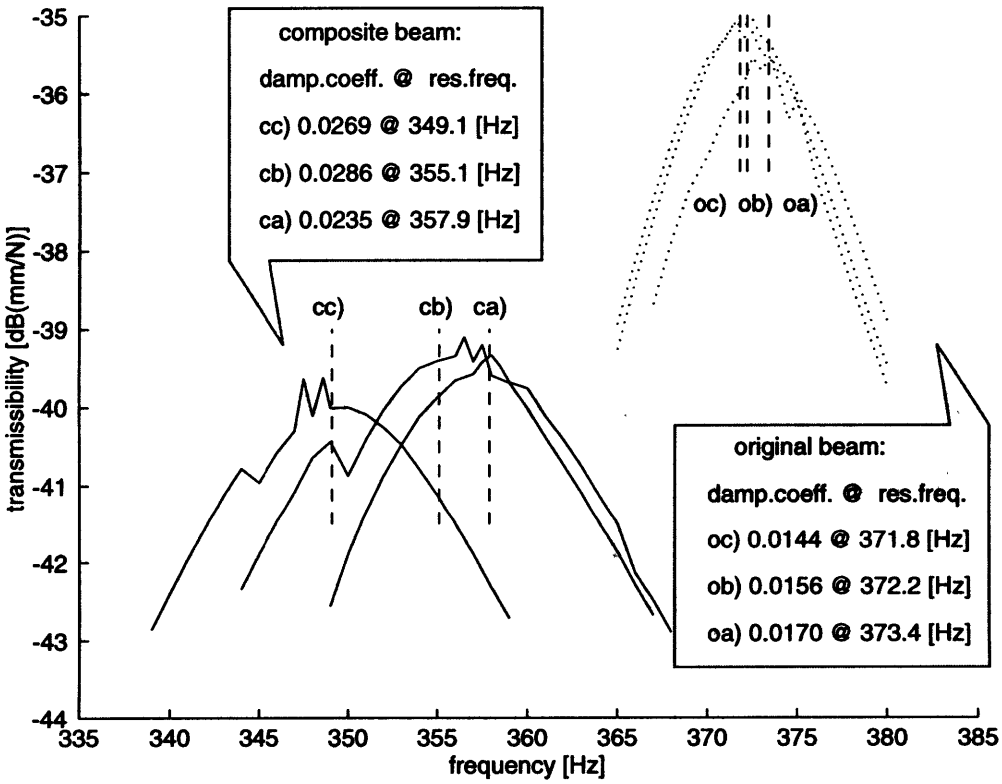

Figure 5.8: Transmissibility Curves of the Test Beams

Fig. 5.8 shows the transmissibility curves for the test beams in the neighborhood of their resonant frequencies. Due to the differences in the inertia and the stiffness of the two beams, their resonant frequencies differ by about 20 Hz, which is expected from the theoretical analysis. From

the above graphs, half power points are all identified, and with the measured resonant frequencies, the damping coefficient is calculated using Eq. (5.33),

$$Q \cong \frac{1}{2\zeta} \cong \frac{\omega_n}{\omega_2 - \omega_1},$$

and they are listed in Table 5.3.

Table 5.3: Summary of the Experimental Result

	resonant frequency [*Hz*]	damping coefficient
steel beam	371.8	0.0144
	372.2	0.0156
	373.4	0.0170
composite beam	349.1	0.0269
	355.1	0.0286
	337.9	0.0235

Comparison of the damping coefficients of the two beams reveals that the damping coefficient of the composite beam is about twice as great as that of the steel beam. This indicates that indeed the damper layer reduces the vibration energy even from the elastic deformation. The frequency shift of each loading case of the composite beam also indicates a non-linear relationship among input load, resonant frequency and the damping coefficient as noted before.

5.4 Further Development of Theoretical Analysis

5.4.1 Vibration of Beam

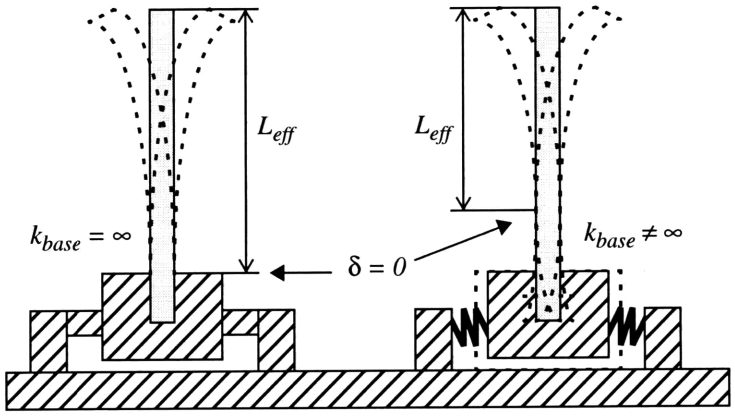

Figure 5.9: Effective Length Decrease due to the Vibration of the Base

There exists a discrepancy of about 100 Hz between the resonant frequency of the theoretical prediction and that of the experimental result. From a number of experiments with various other clamping devices, it is verified that the boundary condition of the experimental setup above is not a free-clamped condition because of the base vibration. The vibration of the base raises the resonant frequency of the vibration because it shortens the effective length, L_{eff} as shown in Fig. 5.9.

Table 5.4: Recalculated Values for the Equations of Motion

item	symbol	value
effective length $[mm]$	$L_{eff,\ orig}$	145
	$L_{eff,\ comp}$	143
equivalent mass $[kg]$	m_{orig}	$69.2\text{x}10^{-3}$
	m_{comp}	$68.7\text{x}10^{-3}$
equivalent stiffness $[N/m]$	k_{orig}	$379\text{x}10^{3}$
	k_{comp}	$340\text{x}10^{3}$
$\frac{\text{damping constant}}{\text{damping coefficient}}$ $[Ns/m]$	$\frac{c_{orig}}{\xi_{orig}}$	324
	$\frac{c_{comp}}{\xi_{comp}}$	305
resonant frequency $[Hz]$	$f_{resonant,\ orig}$	373
	$f_{resonant,\ comp}$	355

Listed in Table 5.4 are the new values for the equations of the motion in the theoretical analysis with the calculated new effective length of each beam[1] from the experimental resonant frequency. From the above values and the measured damping coefficients from the experimental analysis in Table 5.3, transmissibility curves are calculated[2], and are plotted in Fig. 5.10. The solid lines indicate the transmissibility curve of the theoretical analysis, and the dotted lines indicate that of the experimental data, showing good agreement with each other.

1. L_{eff} of each beam is different because each beam has different mass and stiffness.
2. See Eq. (5.16).

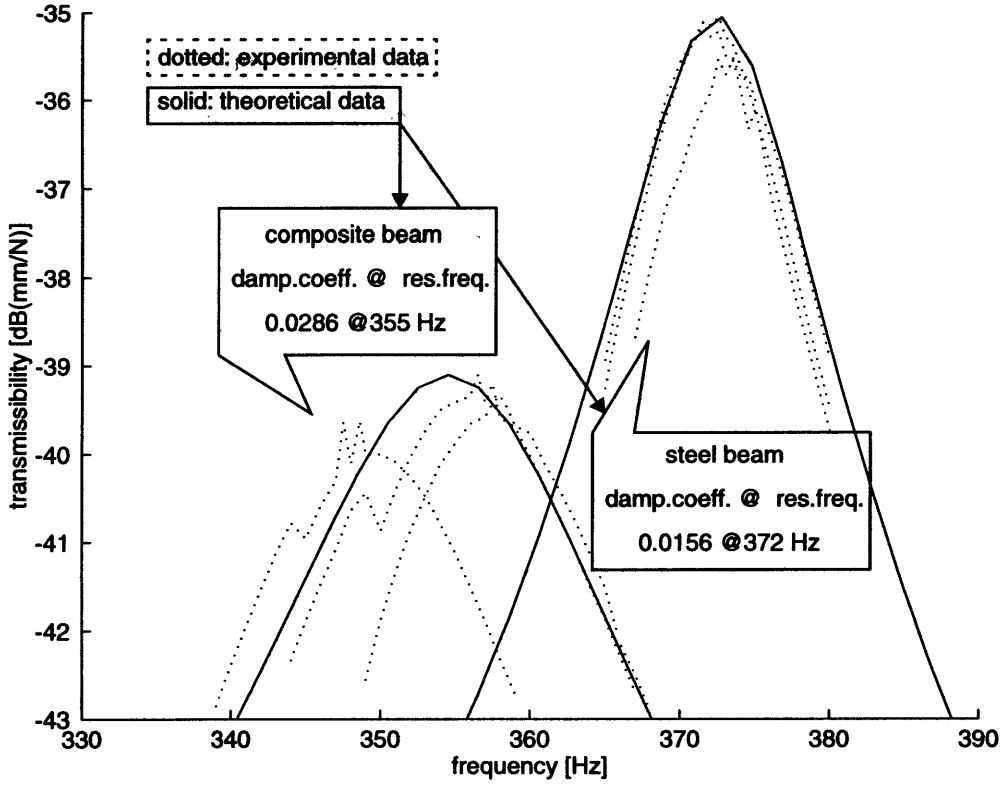

Figure 5.10: Transmissibility Curve of Experimental and Theoretical Analysis

5.4.2 Vibration of Gear Tooth from the Cyclic Energy Loss Analysis

Further development of the cyclic energy loss analysis of Chapter 4 can be pursued with Eqs. (5.11) and (5.12) of equivalent mass and equivalent stiffness.

Also, using Eq. (5.34),

$$\Delta W = \pi c \omega X^2,$$

it is possible to complete the equation of motion for the composite gear tooth. From the previous analysis, the lost energy per cycle, ΔW turned out to be $0.584 \times 10^{-3} J$, which is 22.6% of the total energy, 2.5×10^{-3} J for the case of 247 N load and 0.4 mm damper thickness. The deflection, X, is about 4.74 μm, which is the average value of the first deflection and that of the second.

Hence, the damping constant c and damping coefficient f can be calculated, and they are listed in Table 5.5. It turns out that with 22% cyclic energy loss, the beam does not oscillate at all.

Table 5.5: Dynamic Constants of Bimetallic Composite Helical Gears

m_{eq}	k_{eq}	$f_{resonant}$	c_{eq}	ζ
4.29×10^{-12} *kg*	336 *N/m*	145×10^{3} *Hz*	5.7 *Ns/m*	N/A[a]

a. $\zeta > 1$, therefore it is not defined, meaning no oscillation in the system.

5.5 Conclusions

The damping characteristics of the bimetallic composite gear teeth is investigated using a bimetallic beam structure for the cases of elastic deformation. Experimental results show that the damping coefficient of the bimetallic beam is about twice larger than that of the steel beam. From the measured damping coefficient, the equations of motion and the transmissibility of the bimetallic beam are established. The transmissibility curve from the theoretical calculation agrees well with that of the empirical data, indicating the successful modeling of the bimetallic beam structure.

Also, the connection between the cyclic energy loss analysis of Chapter 4 and the dynamic damping analysis is made using some of the developed equations.

Chapter 6

Summary of Results and Future Studies

6.1 Summary of Research

Two experimental investigations are reported: one with bimetallic composite bevel gears and the other with bimetallic composite helical gears. The experimental results show that the vibration and the noise level of the bimetallic gears are about 1 to 3 *dB* lower than that of the original conventional gears at the harmonics of the mesh frequencies.

In order to understand the dynamics of gear teeth, an experimental model of a simple beam is used. The results from this modeling show that the damping coefficient of the bimetallic beam structure is about as twice as that of the steel beam.

The cyclic energy loss of the bimetallic composite gear teeth is calculated using a beam bending equations and the assumed elastic-perfectly plastic stress-strain relationship. This analysis reports that about 22% of the vibration energy is lost due to the plastic deformation of a damper of 2 *mm* by 2 *mm* by 0.4 *mm*, when the tangential load is about 40% of the maximum loading. With the theoretical maximum load of 667 *N*, about 10% energy loss is calculated from the deformation of the same damper. Also, this analysis indicates that the energy loss percentage is inversely related to the thickness of the damper and the amount of the load.

The dynamic damping analysis is also performed to complete the equation of the motion for the test beams. With the measured damping coefficient, the transmissibility curve of the bimetallic beam is identified, and it agrees well with that of the experimental data.

In conclusion, the internal damping of the bimetallic beam structure is higher than that of the conventional beam structure, and the application of the bimetallic beam structure in gear teeth indeed lowers the vibration and noise level of gears

6.2 Future Works

From the above studies, the basic dynamic analysis of the gear teeth are established. The next step is to understand the significance of the gear teeth damping effect due to the existence of damper layers with respect to the overall vibration and noise of the gear blanks.

Experimentally, clearer evidence of the damping effects due to the bimetallic structure should be established from the rigorous analysis on the dynamic of each component of the experimental apparatus. Full-load experiments are also recommended in the gear noise testing, where the vibration and noise are measured when the gears are running at the maximum load. The increased load will not only increase the vibration and the noise level of the test gears, but also increase the damping effect of the bimetallic structure due to the larger damper deformation.

After the full understanding of the damping effect of the bimetallic structure in gears, the design optimization should be followed in order to maximize the damping effect, yet minimize the power transmission efficiency loss, which occurs due to the compensated stiffness from the application of the bimetallic structure.

And finally, an improvement in the manufacturing method of the bimetallic gears should be studied for economical production of the bimetallic gears.

Appendix A

Experimental Components

A.1 Measuring Devices

A.1.1 Accelerometer and Force Transducer

The most widely used transducer for vibration measurements is the piezoelectric accelerometer. It exhibits better all-round characteristics than any other type of vibration transducer. It has very wide frequency and dynamic ranges with good linearity throughout the ranges, and because there are no moving parts to wear out, it is very robust and reliable so that its characteristics remain stable over a long period of time. Additionally, the piezoelectric accelerometer is self-generating, so that it does not need a power supply. Its acceleration proportional output can be integrated to give velocity and displacement proportional signals as shown below equations.

$$\text{displacement} = \frac{\text{acceleration}}{(\text{frequency})^2}, \quad \text{velocity} = \frac{\text{acceleration}}{\text{frequency}} \tag{A.1}$$

The heart of a piezoelectric accelerometer is the slice of piezoelectric material, usually an artificially polarized feroelectric ceramic, which exhibits the unique piezoelectric effect. When it is mechanically stressed, either in tension, compression or shear, it generates an electrical charge across its pole faces which is proportional to the applied force. In practical accelerometer designs, the piezoelectric element is arranged so that when the assembly is vibrated the mass applied a force to the piezoelectric element which is proportional to the vibratory acceleration [15].

Force transducers or "load cells" are used in mechanical-dynamics measurement together with accelerometers to determine the dynamic forces in a structure and the resulting vibratory motions, in order to describe the mechanical impedance of the structure. The force transducer also uses a piezoelectric element, which when compressed gives an electrical output proportional to the force transmitted through it. The force signals can be processed and measured with exactly the same instrumentation used with accelerometers [15].

A.1.2 Sound Pressure Level and Microphone

In theoretical investigations of sound, it is convenient to express sound pressures in N/m^2 and sound intensities in $Watts/m^2$. However, in experimental work it is customary to describe these

qualities through the use of logarithmic scales known as sound pressure levels (SPL). The use of a logarithmic scale compresses the range of numbers required to describe this wide range of intensities, which is often encountered in acoustical environment; audible intensities range from approximately 10^{-12} to 10 *Watts/m*^{2}. Also, the human ear subjectively judges the relative loudness of two sounds by the ratio of their intensities, which is a logarithmic behavior.

The sound pressure level (SPL), then, can be expressed as,

$$SPL = 20 \cdot \log\left(\frac{P_e}{P_0}\right) \tag{1.2}$$

where P_e is the measured effective pressure of the sound wave, and P_0 is the reference effective pressure. A reference pressure of $P_0 = 0.00002$ *N/m*^{2}, or the equivalent pressures of 0.0002 *dyne/ cm*^{2} or 0.0002 *microbar*, is commonly used for computing sound pressure levels in air [14].

Piezoelectric microphones employ crystals or dielectrics which upon being distorted by the action of incident sound waves become electrically polarized and produce voltages linearly related to the mechanical strains. The acoustic signals also can be processed and measured with the same instrumentation used with accelerometers. [15]

A.2 Motor Drive

A.2.1 AC and DC Motor Drive Comparison

There are two kinds of drives: alternating-current (AC) drives and direct-current (DC) drives. Both offer unique benefits and features that may make one type or other better suited for certain applications. [16] However comparing their benefits in applications, AC drives may be better because,

- They use conventional, low cost, three phase AC induction motors for most applications.
- AC motors require virtually no maintenance and are preferred for applications where the motor is mounted in an area not easily reached for servicing and replacement.
- AC motors are smaller, lighter, more commonly available, and less expensive than DC motors.
- AC motors are better suited for high speed operation (over 2500 *rpm*) since there are no brushes, and commutation is not a problem.
- Whenever the operating environment is wet, corrosive or explosive and special motor enclosures are required. Special AC motor enclosure types are more readily available at lower price.

- When multiple motors in a system must operate simultaneously at a common frequency and therefore, speed.
- When the application load varies greatly and light loads may be encountered fir a prolonged periods. DC motor commutators and brushes may wear rapidly under this condition.
- When low cost electronic motor reversing is required.

However, DC drives may be better because

- DC drives are less complex with a single power conversion from AC to DC.
- DC drives are normally less expensive for most horsepower ratings.
- DC motors have a long tradition of use as adjustable speed machines and a wide range of options have evolved for this purpose.
- Cooling blowers and inlet air flanges provide cooling air for a wide speed range at constant torque.
- DC regenerative drives are available for applications requiring continuous recrimination for overhauling loads. AC drives with this capability would be more complex and expensive.
- DC motors are capable of providing starting and accelerating torques in excess of 400% of rated.
- Some AC drive may produce audible motor noise which is undesirable in some applications.

Comparing the cost and application conditions, DC drives are recommended for gear testing especially when the rated power has to be more than one horse power.

A.2.2 DC Motor Characteristics

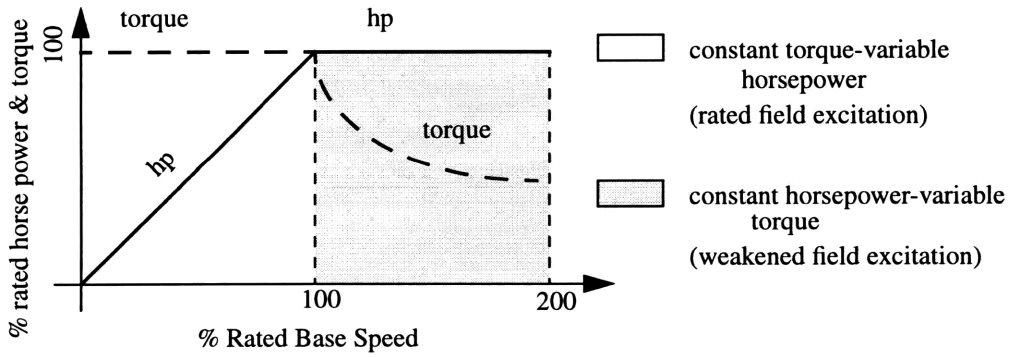

Figure A.1: DC Motor Characteristics [16]

A shunt-wound motor is a DC motor in which the field windings and the armature may be connected in parallel across a constant-voltage supply. In adjustable speed applications, the field is connected across a constant-voltage supply and the armature is connected across an independent adjustable-voltage supply. Permanent magnet motors have similar control characteristics but differ

primarily by their integral permanent magnet field excitation.

The speed of a DC motor is proportional to its armature voltage; the torque is proportional to armature current, and the two quantities are independent. Armature voltage controlled DC drives are constant torque drives. They are capable of providing rated torque at any speed between zero and the base speed of the motor as shown in Fig. 2.6. Horsepower varies in direct proportion to speed, and 100% rated horsepower is developed only at 100% rated motor speed with rated torque.

Most of motors are rated with power unit of horsepower (*hp*), and the rotational speed is rated with speed unit of rotational per minute (*rpm*), which are related to each other with the following equation,

$$\text{horse power [HP]} = \frac{\text{torque [lbf in]} \cdot \text{rotational speed [RPM]}}{63025} \tag{A.3}$$

Therefore, a 1 *hp* motor with the base speed of 1750 *rpm* exerts the torque of 245 lbf in.

A.2.3 DC Motor Drive Types

There are two kinds of drives for DC motors: nonregenerative and regenerative DC drives. Nonregenerative DC drive controllers are the most conventional type in common usage. In their most basic form they are able to control motor speed and torque in one direction only. The addition of an electromechanical (magnetic) armature reversing contractor or manual switch permits reversing the controller output polarity and therefore the direction of rotation of the motor armature. In both cases toque and rotational direction are the same.

Nevertheless, regenerative adjustable speed drives, also known as four-quadrant drives, are capable of controlling not only the speed and direction of motor rotation, but also the direction of motor torque. The term regenerative describes the ability of the drive under braking conditions to convert the mechanical energy of the motor and connected load into electrical energy which is regenerated to the AC power source, working as a generator.

Shown in Fig. 2.7 is the mechanism of regenerative drives. When the drive is operating in quadrants I and III, both motor rotation and torque are in the same direction and it functions as a conventional nonregenerative unit. The unique characteristics of a regenerative drive are apparent only in Quadrants II and IV, where the motor torque opposes the direction of motor rotation which provides a controlled barking or retarding force. A high performance regenerative drive, is able to switch rapidly from motoring to braking modes while simultaneously controlling the direction of motor rotation.

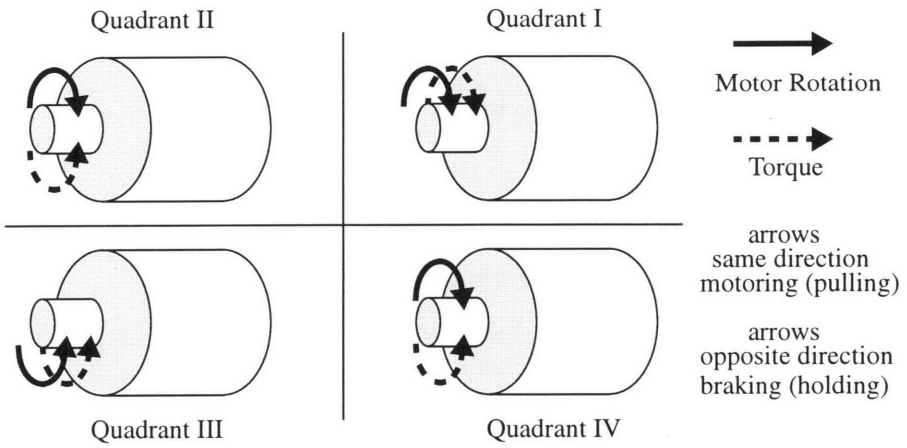

Figure A.2: Regenerative DC Motor Drive [16]

A regenerative DC drive is essentially two coordinate DC drives integrated within a common package. One drive operates in Quadrants I and IV, the other operates in Quadrants II and III. Sophisticated electronic control circuits provide interlocking between the two opposing drive sections for reliable control of the direction of motor torque and/or direction of rotation. [16]

Appendix B

Bimetallic Composite Bevel Gears

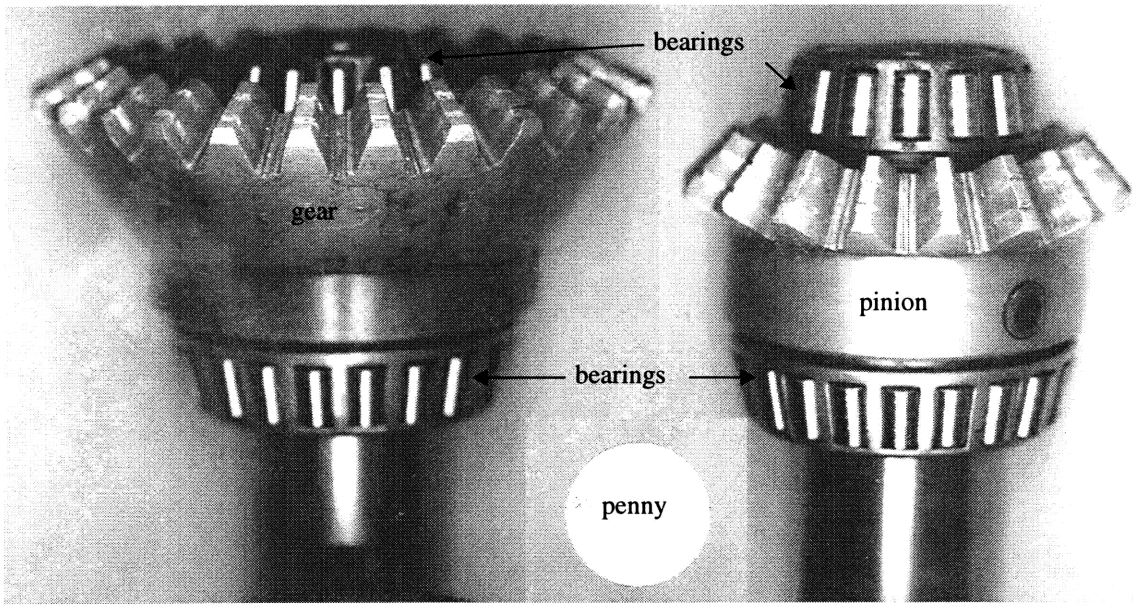

Figure B.1: Picture of Bimetallic Composite Bevel Gears

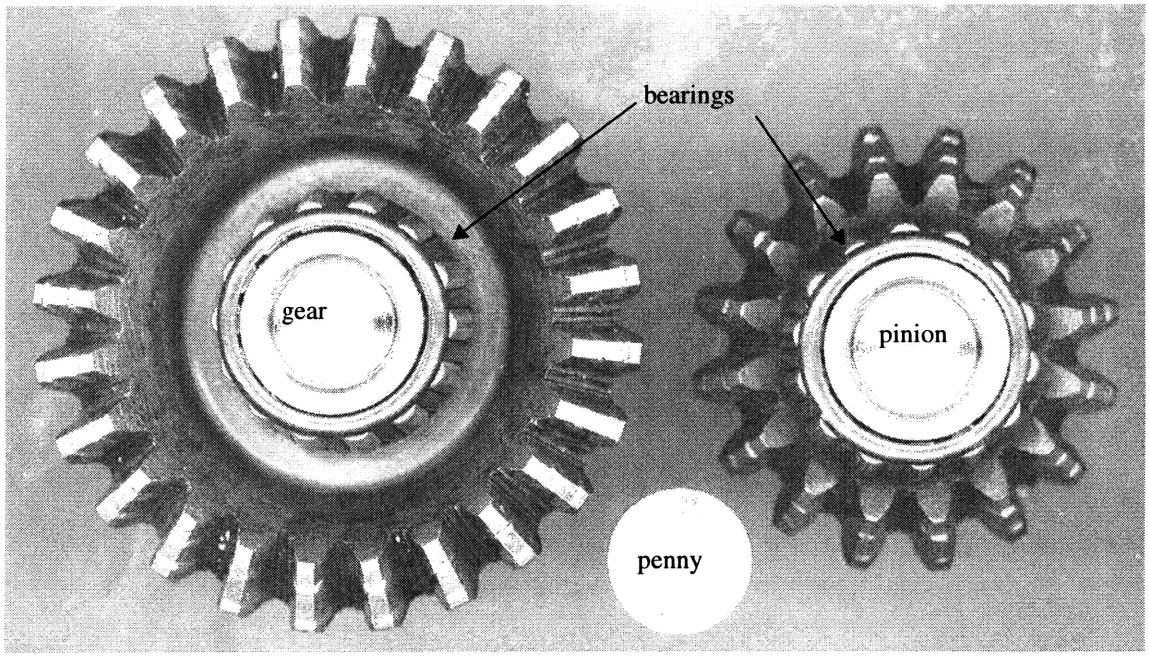

Figure B.2: Picture of Bimetallic Composite Bevel Gear Teeth

Appendix C

Bimetallic Composite Helical Gears

C.1 Helical Gear Dimensions

Although the vender is Boston Gears, only the housing is made by Boston Gears, but the gears are made by a supplier from Germany, who uses metric system for gear manufacturing and refuses to submit the dimensions of their gears. Therefore, two different calculations are performed.

Table C.1: Gear Dimensions according to the ANSI System

	Symbol	[in]	[mm]	Formula*
Speed Ratio		1.633		Ng/Np
Pressure Angle	f	21.17°		$\text{atan}\left(\frac{\tan\phi}{\cos\psi}\right)$
Normal Pressure Angle	f_n	20°		*given*
Helix Angle	y	20°		*given*
Base Helix Angle	y_b	18.75°		$\text{atan}(\tan\psi \cdot \cos\phi)$
Diametral Pitch	P	23.868	-	$P_n cos\psi$
Circular Pitch	P_c	0.132	-	π/P
Base Pitch	P_b	0.063	-	$2\pi R_b/N$
Normal Diametral Pitch	P_n	25.4	-	*given*
Normal Circular Pitch	P_{cn}	0.124	-	$P_c cos\psi$
Center Distance	C	1.69	42.93	*given*
Face Contact Ratio	m_f	1.095		$\frac{W}{P_c}\tan\psi$
Module	m	0.021	-	Dp/N
Addendum	a	0.021	0.54	m
Dedendum	d	0.025	0.63	$1.15m$
Path of Contact		0.103	2.62	pt_g+pt_p

*Formula is valid for the ANSI system only

Table C.2: Gear Dimensions according to the Metric System

Item	Symbol	Formula*	Metric	
			Gear	Pinion
Normal Module	m_n		1	
Normal Pressure Angle	f_n	[°]	20	
Helix Angle	y	[°]	20	
Teeth Number	n_g, n_p		49	30
Radial Pressure Angle	f	$\text{atan}\left\{\frac{\tan\phi_n}{\cos\psi}\right\}$ [°]	21.2	
Center Distance	C	$\frac{(n_g + n_p)m_n}{2\cos\psi}$ [mm]	42.0	1.65
Standard Pitch Diameter	d_{pg}, d_{pp}	$\frac{n}{\cos\psi}m_n$ [mm]	52.1	2.05
Base Diameter	d_{bg}, d_{bp}	$d_p\cos\phi$ [mm]	48.6	1.91
Addendum	a	m_n [mm]	1	0.04
Whole Depth	h	$2.25m_n$ [mm]	2.2	0.09
Outside Diameter	d_{og}, d_{op}	$d_p + 2h_a$ [mm]	54.1	2.13
Root Diameter	d_{rg}, d_{rp}	$d_o - 2h$ [mm]	49.6	1.95

*Formula is valid for the metric system only

C.2 Bimetallic Composite Helical Gears

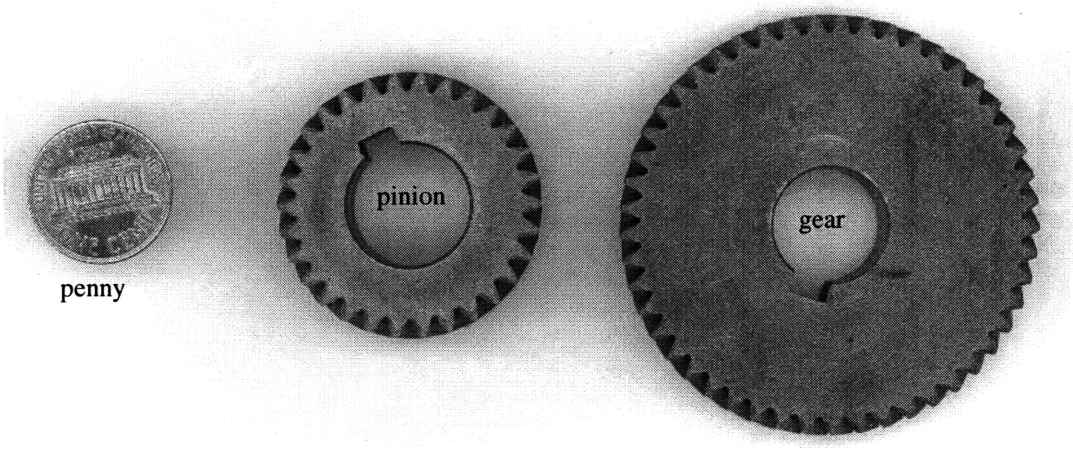

Figure C.1: Picture of Helical Pinion and Gear

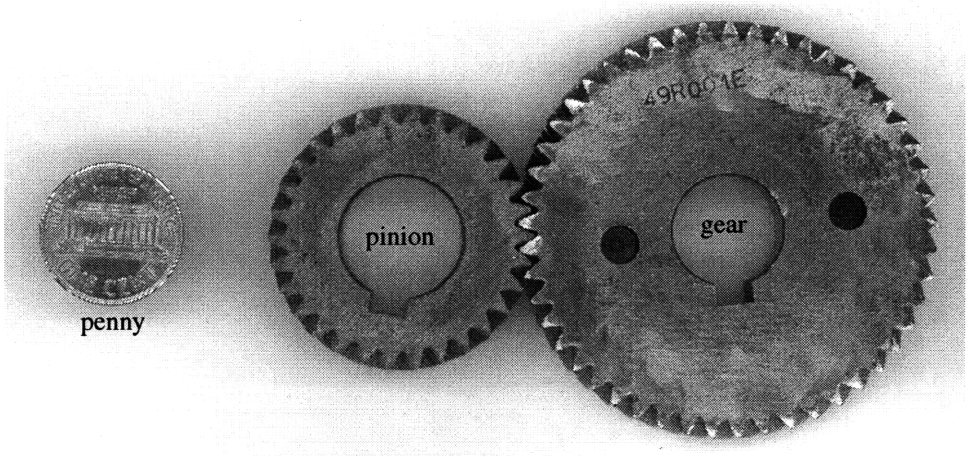

Figure C.2: Picture of the Meshing of Helical Pinion and Gear

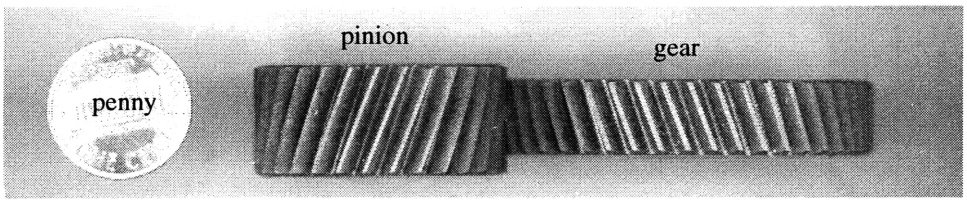

Figure C.3: Picture of Original Helical Gear Teeth

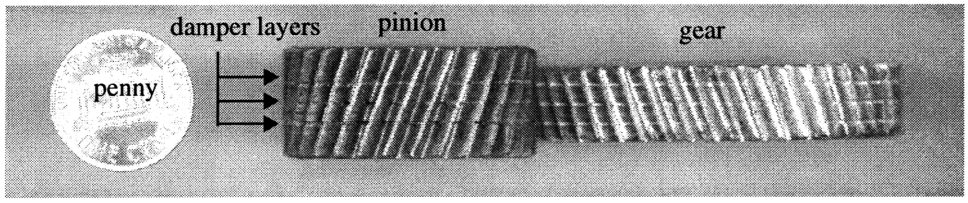

Figure C.4: Picture of Bimetallic Composite Helical Gear Teeth

C.3 Matlab Programs for Cyclic Energy Loss Analysis

C.3.1 rundamp.m

This is the matlab program used in the cyclic energy loss analysis. It consists of two parts; the first part calculates and graphs the relationship among the damper thickness vs. load force vs. energy loss, and the second part calculates and graphs the deflection of the beam when the damper thickness is 4 mm, and load is 247 N, which results in 10.4585% energy loss.

```
clear
N=20;

%%%%% MATERIAL CONSTANT

E_s=200e9;% 200 [GPa]
G_s=E_s/2.6;% 76.923 [GPa]
Y_s=1e9;% 1 [GPa]

E_t=45e9;% 45 [GPa]
G_t=E_t/2.6;% 17.308 [GPa]
Y_t=30e6;% 30 [MPa]

%%%%% GEAR DIMENSION

eta=1.5;
L=2e-3;  % 2 [mm]
H=2e-3;  % 2 [mm]
W=2e-3;  % 2 [mm]

A_b=W*H;
I_b=W*L^3/12;
%%%%%
```

```
Fmax=Y_s*H^2/6; % 666.6667 [N]

d=linspace(L/20,L/2,N);
for p=1:N
    Fmin(p)=d(p)*sqrt(3)*Y_t/E_t*(6*E_s*I_b*A_b*G_s)/
    sqrt((2*A_b*G_s*L^3+6*eta*E_s*I_b*L)^2+d(p)^2*(3*A_b*G_s*L^2+6*eta*E_s*I_b)^2);
    F=linspace(Fmax,Fmin(p),N);
    for q=1:N
        [loss_percentage(q,p),initial_energy(q,p),plastic_energy(q,p)]=damp(F(q),d(p));
    end
end

figure(1),clg
    subplot(2,1,1), plot(1e3*d,Fmin)
        xlabel('damper thickness [mm]')
        ylabel('Fmin [N]')
        text(0.1,40,'Fmax = constant @ 667 N')
        axis([0,1,0,50])
    subplot(2,1,2), plot(1e3*d,Fmin)
        xlabel('damper thickness [m]')
        ylabel('Fmin [N]')
        text(0.1,40,'Fmax = constant @ 667 N')
        axis([0,1,0,50])
    print -deps helical01.eps

figure(2),clg,hold on
    mesh(d*1e3,F,initial_energy)
    mesh(d*1e3,F,plastic_energy),grid
    xlabel('damper thickness [mm]')
    ylabel('load [N]')
    zlabel('energy [J]')
    axis([0,1,0,700,0,0.02])
    view(235,30)
    print -deps helical02.eps

figure(3),clg,hold on
    mesh(d*1e3,F,loss_percentage),grid
    xlabel('damper thickness [mm]')
    ylabel('load [N]')
    zlabel('loss percentage [%]')
    axis([0,1,0,700,0,80])
    view(235,30)
    print -deps helical03.eps

figure(4),clg
    subplot(2,2,1),mesh(d*1e3,F,loss_percentage),grid
        title('(a)')
        xlabel('thickness [mm]')
        ylabel('load [N]')
        zlabel('loss percentage [%]')
        axis([0,1,0,700,0,80])
        view(60,30)
    subplot(2,2,2),mesh(d*1e3,F,loss_percentage),grid
        title('(b)')
        xlabel('thickness [mm]')
        ylabel('load [N]')
        zlabel('loss percentage [%]')
        axis([0,1,0,700,0,80])
```

```
        view(135,30)
    subplot(2,2,3),mesh(d*1e3,F,loss_percentage),grid
        title('(c)')
        xlabel('thickness [mm]')
        %ylabel('load [N]')
        zlabel('loss percentage [%]')
        axis([0,1,0,700,0,80])
        view(180,0)
    subplot(2,2,4),mesh(d*1e3,F,loss_percentage),grid
        title('(d)')
        %xlabel('thickness [mm]')
        ylabel('load [N]')
        zlabel('loss percentage [%]')
        axis([0,1,0,700,0,80])
        view(-90,00)
    print -deps helical04.eps
```

C.3.2 damp.m

```
function[loss_percentage04,total_energy0,d_p_energy]=damp(F1,d)

%%%%% MESH SIZE

N=10;

%%%%% MATERIAL CONSTANT

E_s=200e9;% 200 [GPa]
G_s=E_s/2.6;% 76.923 [GPa]
Y_s=1e9;% 1 [GPa]

E_t=45e9;% 45 [GPa]
G_t=E_t/2.6;% 17.308 [GPa]
Y_t=30e6;% 30 [MPa]

%%%%% GEAR DIMENSION

eta=1.5;
L=2e-3;  % 2 [mm]
H=2e-3;  % 2 [mm]
W=2e-3;  % 2 [mm]

A_b=W*H;
I_b=W*L^3/12;

%%%%% DAMPER DIMENSION

%d=.4e-3;% 0.4 [mm]

%%%%% COORDINATES

x=linspace(0,L,N);
z=linspace(0,d,N);

%%%%% FORCE

%F1=70;
k=1/(L^3/(3*E_s*I_b)+eta*L/(A_b*G_s));
```

```
delta1=F1/k;

%%%%% STRAIN & DEFORMATION

for i=1:N
    f(i)=(-A_b*G_s*x(i)^3+3*A_b*G_s*L*x(i)^2+6*eta*E_s*I_b*x(i))/(2*(A_b*G_s*L^3+2*eta*E_s*I_b*L));
    fp(i)=(-3*A_b*G_s*x(i)^2+6*A_b*G_s*L*x(i)+6*eta*E_s*I_b)/(2*(A_b*G_s*L^3+2*eta*E_s*I_b*L));
    st_deform1(i)=delta1*f(i);
    st_strain1(i)=delta1*fp(i)/sqrt(3);
    st_e_energy_d1(i)=E_s*st_strain1(i)^2/2;
    for j=1:N
        d_deform1(j,i)=delta1/d*z(j)*f(i);
        d_strain1(j,i)=delta1*sqrt(f(i)^2+(z(j)*fp(i))^2)/d/sqrt(3);
        if d_strain1(j,i) > (Y_t/E_t)
            d_p_strain1(j,i)=d_strain1(j,i)-(Y_t/E_t);
            d_e_energy_d1(j,i)=Y_t^2/E_t;
            if d_strain1(j,i) > 2*(Y_t/E_t)
                d_p_energy_d2(j,i)= (d_strain1(j,i)-2*(Y_t/E_t))*Y_t;
            else
                d_p_energy_d2(j,i)=0;
            end
        else
            d_p_strain(j,i)=0;
            d_e_energy_d1(j,i)=E_t*d_strain1(j,i)^2/2;
        end
    end
end

%%%%% EVALUATION OF ENERGY

st_e_energy1=sum(sum(st_e_energy_d1))*H*L/N*W;
d_e_energy1=sum(sum(d_e_energy_d1))*H*L/N*d/N;
d_p_energy1=Y_t*sum(sum(d_p_strain1))*H*L/N*d/N;
d_p_energy2=sum(sum(d_p_energy_d2))*H*L/N*d/N;

total_energy0=st_e_energy1+d_e_energy1+d_p_energy1;
total_energy1=st_e_energy1+d_e_energy1;
total_energy2=total_energy1-d_p_energy2;
loss_percentage01=100*(total_energy0-total_energy1)/total_energy0;
loss_percentage12=100*d_p_energy2/total_energy1;
loss_percentage02=100*(total_energy0-total_energy2)/total_energy0;

%%%%% New Force

F3=F1*(100-(loss_percentage01+loss_percentage12)/2)/100;
delta3=F3/k;

%%%%% STRAIN & DEFORMATION

for i=1:N
    st_deform3(i)=delta3*f(i);
    st_strain3(i)=delta3*fp(i)/sqrt(3);
    st_e_energy_d3(i)=E_s*st_strain3(i)^2/2;
    for j=1:N
        d_deform3(j,i)=delta3/d*z(j)*f(i);
        d_strain3(j,i)=delta3*sqrt(f(i)^2+(z(j)*fp(i))^2)/d/sqrt(3);
        if d_strain3(j,i) > 2*(Y_t/E_t)
            d_p_energy_d4(j,i)=Y_t*(d_strain3(j,i)-2*(Y_t/E_t));
            d_e_energy_d4(j,i)=Y_t^2/E_t;
```

```
            else
                if d_strain3(j,i) > (Y_t/E_t)
                    d_e_energy_d4(j,i)=Y_t^2/E_t/2+(Y_t-d_strain3(j,i))^2*E_t/2;
                else
                    d_e_energy_d4(j,i)=Y_t^2/E_t/2-(Y_t-d_strain3(j,i))^2*E_t/2;
                end
            end
            if d_strain1(j,i) > 2*(Y_t/E_t)
                d_p_strain3(j,i)=d_strain3(j,i);
            else
                if d_strain1(j,i) > (Y_t/E_t)
                    d_p_strain3(j,i)=d_strain3(j,i)+d_strain1(j,i)-2*(Y_t/E_t);
                    d_e_energy_d3(j,i)= Y_t^2/E_t/2-(d_strain1(j,i)-(Y_t/E_t))^2*E_t/2;
                else
                    d_p_strain3(j,i)=0;
                    d_e_energy_d3(j,i)=E_t*d_strain3(j,i)^2/2;
                end
            end
        end
    end

    st_e_energy3=sum(sum(st_e_energy_d3))*H*L/N*W;
    d_e_energy3=sum(sum(d_e_energy_d3))*H*L/N*d/N;
    d_p_energy3=Y_t*sum(sum(d_p_strain3))*H*L/N*d/N;
    d_e_energy4=sum(sum(d_e_energy_d3))*H*L/N*d/N;
    d_p_energy4=sum(sum(d_p_energy_d4))*H*L/N*d/N;

    %total_energy2=st_e_energy3+d_e_energy3+d_p_energy3;
    total_energy3=st_e_energy3+d_e_energy3;
    total_energy4=total_energy3-d_p_energy4;
    loss_percentage23=100*d_p_energy3/(st_e_energy3+d_e_energy3+d_p_energy3);
    loss_percentage03=100*(total_energy0-total_energy3)/total_energy0;
    loss_percentage34=100*d_p_energy4/total_energy3;
    loss_percentage04=100*(total_energy0-total_energy4)/total_energy0;

    d_p_energy=d_p_energy1+d_p_energy2+d_p_energy3+d_p_energy4;
```

C.3.3 deflect247.m

```
clear

%%%%% MESH SIZE

N=10;

%%%%% MATERIAL CONSTANT

E_s=200e9;% 200 [GPa]
G_s=E_s/2.6;% 76.923 [GPa]
Y_s=1e9;% 1 [GPa]

E_t=45e9;% 45 [GPa]
G_t=E_t/2.6;% 17.308 [GPa]
Y_t=30e6;% 30 [MPa]

%%%%% GEAR DIMENSION

eta=1.5;
```

```
L=2e-3;  % 2 [mm]
H=2e-3;  % 2 [mm]
W=2e-3;  % 2 [mm]

A_b=W*H;
I_b=W*L^3/12;

%%%%% DAMPER DIMENSION

d=.4e-3;% 0.4 [mm]

%%%%% COORDINATES

x=linspace(0,L,N);
z=linspace(0,d,N);

%%%%% FORCE

F1=247;
k=1/(L^3/(3*E_s*I_b)+eta*L/(A_b*G_s));
delta1=F1/k; % 4.8782e-06 [m]

%%%%%  STRAIN & DEFORMATION

for i=1:N
    f(i)=(-A_b*G_s*x(i)^3+3*A_b*G_s*L*x(i)^2+6*eta*E_s*I_b*x(i))/(2*(A_b*G_s*L^3+2*eta*E_s*I_b*L));
    fp(i)=(-3*A_b*G_s*x(i)^2+6*A_b*G_s*L*x(i)+6*eta*E_s*I_b)/(2*(A_b*G_s*L^3+2*eta*E_s*I_b*L));
    st_deform1(i)=delta1*f(i);
    st_strain1(i)=delta1*fp(i)/sqrt(3);
    st_e_energy_d1(i)=E_s*st_strain1(i)^2/2;
    for j=1:N
        d_deform1(j,i)=delta1/d*z(j)*f(i);
        d_strain1(j,i)=delta1*sqrt(f(i)^2+(z(j)*fp(i))^2)/d/sqrt(3);
        if d_strain1(j,i) > (Y_t/E_t)
            d_p_strain1(j,i)=d_strain1(j,i)-(Y_t/E_t);
            d_e_energy_d1(j,i)=Y_t^2/E_t;
            if d_strain1(j,i) > 2*(Y_t/E_t)
                d_p_energy_d2(j,i)= (d_strain1(j,i)-2*(Y_t/E_t))*Y_t;
            else
                d_p_energy_d2(j,i)=0;
            end
        else
            d_p_strain(j,i)=0;
            d_e_energy_d1(j,i)=E_t*d_strain1(j,i)^2/2;
        end
    end
end

%%%%% EVALUATION OF ENERGY

st_e_energy1=sum(sum(st_e_energy_d1))*H*L/N*W;
d_e_energy1=sum(sum(d_e_energy_d1))*H*L/N*d/N;
d_p_energy1=Y_t*sum(sum(d_p_strain1))*H*L/N*d/N;
d_p_energy2=sum(sum(d_p_energy_d2))*H*L/N*d/N;

total_energy0=st_e_energy1+d_e_energy1+d_p_energy1; % 0.0025
total_energy1=st_e_energy1+d_e_energy1;
total_energy2=total_energy1-d_p_energy2
loss_percentage01=100*(total_energy0-total_energy1)/total_energy0;
```

```
loss_percentage12=100*d_p_energy2/total_energy1;
loss_percentage02=100*(total_energy0-total_energy2)/total_energy0;

%%%%% New Force

if loss_percentage12==0
    loss_percentage01
    loss_percentage12
    loss_percentage02
    return
end

F3=F1*(100-(loss_percentage01+loss_percentage12)/2)/100;
delta3=F3/k; %  4.5919e-06 [m]

%%%%%  STRAIN & DEFORMATION

for i=1:N
    st_deform3(i)=delta3*f(i);
    st_strain3(i)=delta3*fp(i)/sqrt(3);
    st_e_energy_d3(i)=E_s*st_strain3(i)^2/2;
    for j=1:N
        d_deform3(j,i)=delta3/d*z(j)*f(i);
        d_strain3(j,i)=delta3*sqrt(f(i)^2+(z(j)*fp(i))^2)/d/sqrt(3);
        if d_strain3(j,i) > 2*(Y_t/E_t)
            d_p_energy_d4(j,i)=Y_t*(d_strain3(j,i)-2*(Y_t/E_t));
            d_e_energy_d4(j,i)=Y_t^2/E_t;
        else
            if d_strain3(j,i) > (Y_t/E_t)
                d_e_energy_d4(j,i)=Y_t^2/E_t/2+(Y_t-d_strain3(j,i))^2*E_t/2;
            else
                d_e_energy_d4(j,i)=Y_t^2/E_t/2-(Y_t-d_strain3(j,i))^2*E_t/2;
            end
        end
        if d_strain1(j,i) > 2*(Y_t/E_t)
            d_p_strain3(j,i)=d_strain3(j,i);
        else
            if d_strain1(j,i) > (Y_t/E_t)
                d_p_strain3(j,i)=d_strain3(j,i)+d_strain1(j,i)-2*(Y_t/E_t);
                d_e_energy_d3(j,i)= Y_t^2/E_t/2-(d_strain1(j,i)-(Y_t/E_t))^2*E_t/2;
            else
                d_p_strain3(j,i)=0;
                d_e_energy_d3(j,i)=E_t*d_strain3(j,i)^2/2;
            end
        end
    end
end

st_e_energy3=sum(sum(st_e_energy_d3))*H*L/N*W;
d_e_energy3=sum(sum(d_e_energy_d3))*H*L/N*d/N;
d_p_energy3=Y_t*sum(sum(d_p_strain3))*H*L/N*d/N;
d_e_energy4=sum(sum(d_e_energy_d3))*H*L/N*d/N;
d_p_energy4=sum(sum(d_p_energy_d4))*H*L/N*d/N;

%total_energy2=st_e_energy3+d_e_energy3+d_p_energy3
total_energy3=st_e_energy3+d_e_energy3;
total_energy4=total_energy3-d_p_energy4;
loss_percentage23=100*d_p_energy3/(st_e_energy3+d_e_energy3+d_p_energy3);
loss_percentage03=100*(total_energy0-total_energy3)/total_energy0;
```

```
loss_percentage34=100*d_p_energy4/total_energy3;
loss_percentage04=100*(total_energy0-total_energy4)/total_energy0;%22.6038 [%]
d_p_energy=d_p_energy1+d_p_energy2+d_p_energy3+d_p_energy4; % 5.8403e-04 [J]

figure(5),clg
    subplot(2,2,1),hold on
        mesh(x*1e3,z*1e3,-d_deform1*1e6)
        mesh(x*1e3,z*1e3,d_deform3*1e6)
        axis([0,2,-0.8,1.2,-10,10])
        xlabel('x-axis [mm]')
        ylabel('z-axis [mm]')
        zlabel('deflection [micron]'),grid
        view(110,25)
    subplot(2,2,2),hold on
        mesh(x*1e3,z*1e3,-d_deform1*1e6)
        mesh(x*1e3,z*1e3,d_deform3*1e6)
        axis([0,2,-0.8,1.2,-10,10])
        xlabel('x-axis [mm]')
        ylabel('z-axis [mm]')
        zlabel('deflection [micron]'),grid
        view(70,25)
    subplot(2,2,3),hold on
        mesh(x*1e3,z*1e3,-d_deform1*1e6)
        mesh(x*1e3,z*1e3,d_deform3*1e6)
        axis([0,2,-0.8,1.2,-10,10])
        xlabel('x-axis [mm]')
        %ylabel('z-axis [mm]')
        zlabel('deflection [micron]'),grid
        view(360,0)
    subplot(2,2,4),hold on
        mesh(x*1e3,z*1e3,-d_deform1*1e6)
        mesh(x*1e3,z*1e3,d_deform3*1e6)
        axis([0,2,-0.8,1.2,-10,10])
        %xlabel('x-axis [mm]')
        ylabel('z-axis [mm]')
        zlabel('deflection [micron]'),grid
        view(90,0)
print -deps helical05.eps
figure(6),clg
    subplot(2,2,1),hold on
        mesh(x*1e3,z*1e3,-d_strain1)
        mesh(x*1e3,z*1e3,d_strain3)
        axis([0,2,-0.8,1.2,-10e-3,10e-3])
        xlabel('x-axis [mm]')
        ylabel('z-axis [mm]')
        zlabel('strain'),grid
        view(110,25)
    subplot(2,2,2),hold on
        mesh(x*1e3,z*1e3,-d_strain1)
        mesh(x*1e3,z*1e3,d_strain3)
        axis([0,2,-0.8,1.2,-10e-3,10e-3])
        xlabel('x-axis [mm]')
        ylabel('z-axis [mm]')
        zlabel('strain'),grid
        view(70,25)
    subplot(2,2,3),hold on
        mesh(x*1e3,z*1e3,-d_strain1)
        mesh(x*1e3,z*1e3,d_strain3)
        mesh(x*1e3,z*1e3,-Y_t/E_t*ones(size(d_strain1)))
```

```
        mesh(x*1e3,z*1e3,Y_t/E_t*ones(size(d_strain1)))
        axis([0,2,-0.8,1.2,-10e-3,10e-3])
        xlabel('x-axis [mm]')
        %ylabel('z-axis [mm]')
        zlabel('strain'),grid
        view(360,0)
    subplot(2,2,4),hold on
        mesh(x*1e3,z*1e3,-d_strain1)
        mesh(x*1e3,z*1e3,d_strain3)
        axis([0,2,-0.8,1.2,-10e-3,10e-3])
        %xlabel('x-axis [mm]')
        ylabel('z-axis [mm]')
        zlabel('strain'),grid
        view(90,0)
print -deps helical06.eps
```

C.4 Damper Deformation Graphs

Figs. C.5 and C.6 are the surface deformation and the strain of the damper of 4 *mm* thickness when the load of 80 *N* is applied to one of the neighboring beam. Figs. C.7 and C.8 are the surface deformation and the strain of the damper of 4 *mm* thickness when the load of 150 *N* is applied to one of the neighboring beam.

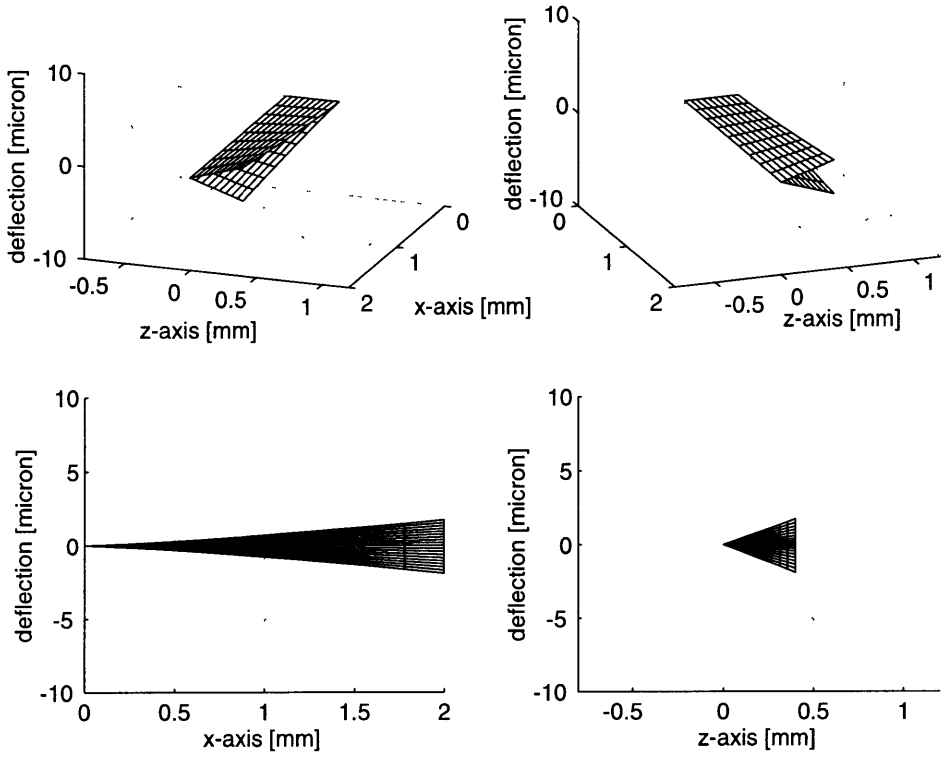

Figure C.5: Damper Surface Deformation at 80 *N* Load

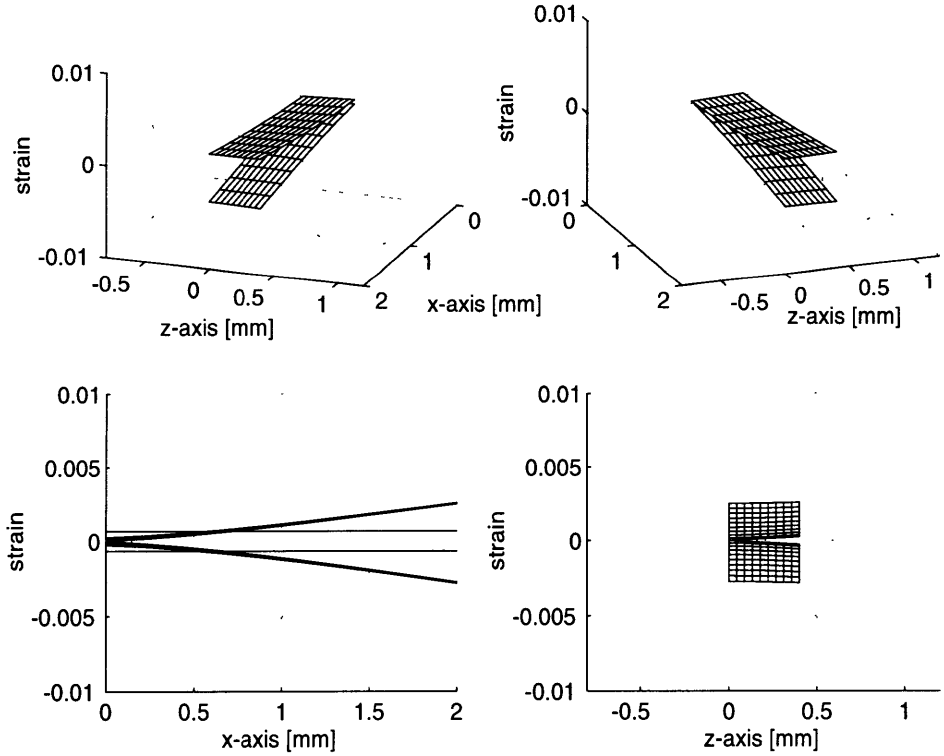

Figure C.6: Damper Equivalent Strain at 80 *N* Load

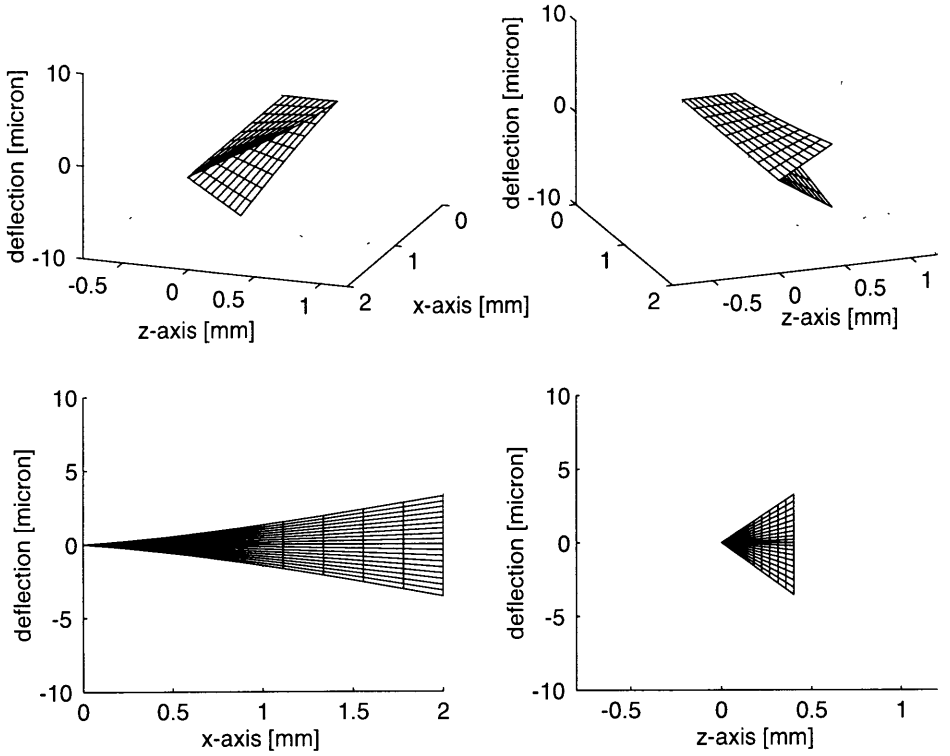

Figure C.7: Damper Surface Deformation at 150 *N* Load

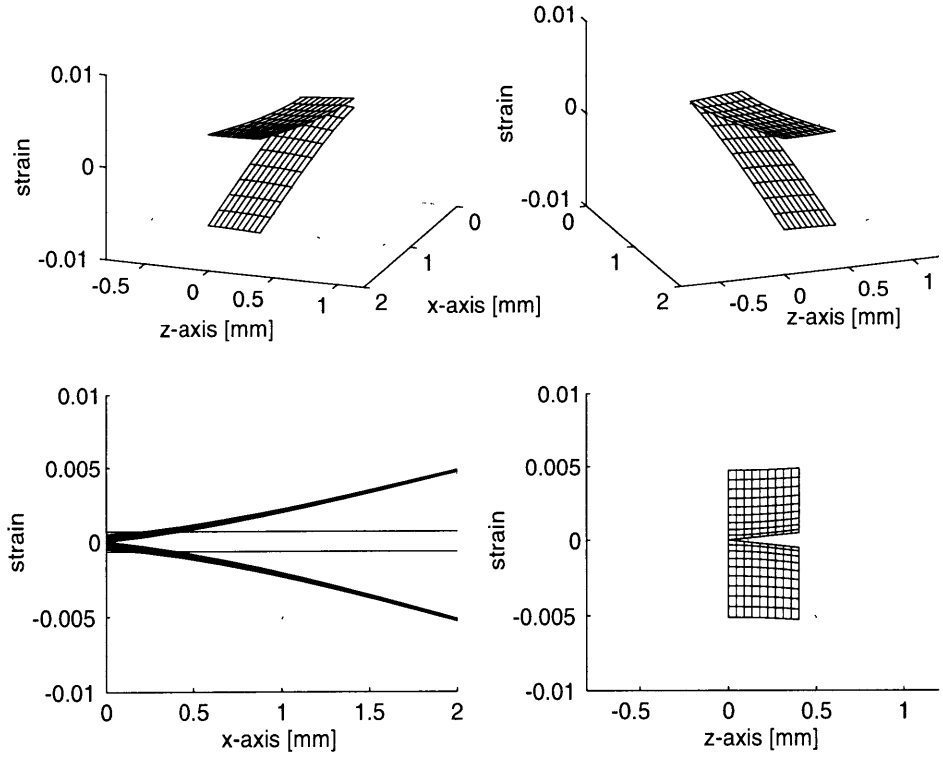

Figure C.8: Damper Equivalent Strain at 150 *N* Load

Appendix D

Bimetallic Composite Beams

D.1 Beam Dimensions

Table D.1: Dimensions of Test Beams

item	symbol	value
length	L	177.8×10^{-3} [m]
height	H	9.398×10^{-3} [m]
width	W	29.5×10^{-3} [m]
width of gap	d	5.46×10^{-3} [m]

D.2 Bimetallic Composite Beam

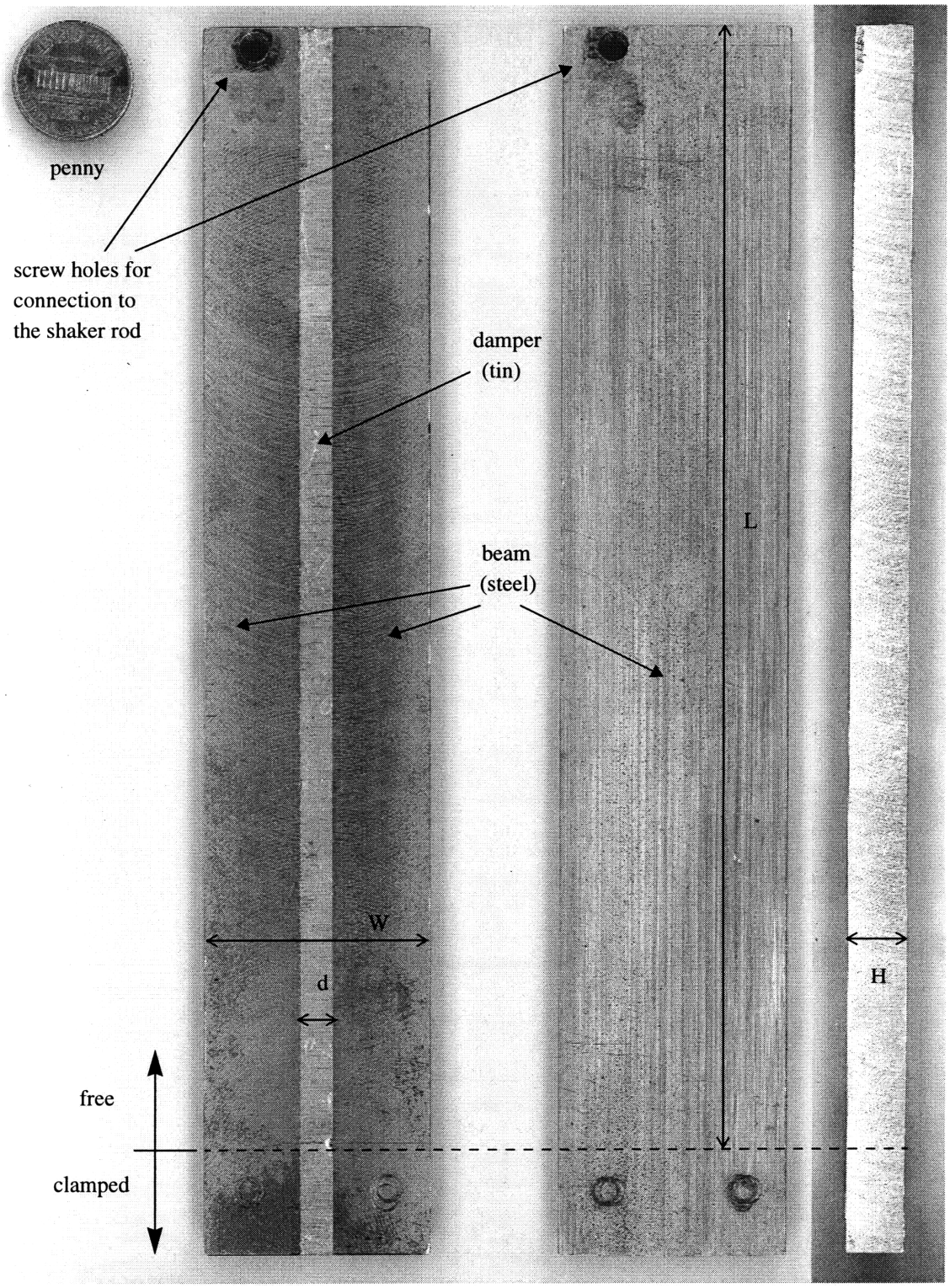

Figure D.1: Bimetallic Composite Beam and Steel Beam (Picture)

References

[1] K. Ariga, T. Abe, Y. Yokoyama and Y. Enomoto. "Reduction of Transaxle Gear Noise by Gear Train Modification". *ASME Journal of Automobile*, a.n. 922108, pp. 1537-1542, 1992

[2] M. G. Donley, T. C. Lim and G. C. Steyer, "Dynamic Analysis of Automotive Gearing Systems", *ASME Journal of Automobile*, a.n. 920762, pp. 958-968, 1992

[3] R. E. Smith, "Gear Tolerances", *Dudley's Gear Handbook*, ch. 7, McGraw-Mill, Inc., New York, second edition, 1992, pp. 7.8-7.9

[4] H. Opitz, "Noise of Gears", *Phil. Trans. of Royal Society*, vol. 263, pp. 369-380, 1969

[5] Raymoond J. Drago, "Gear Types and Nomenclature", *Dudley's Gear Handbook*, ch. 2, McGraw-Mill, Inc., New York, second edition, 1992, pp. 2.1-2.2

[6] M. J. Crocker, "The Generation of Noise in Machinery, Its Control, and the Identification of Noise Sources", *Encyclopedia of Acoustics*, vol. 2, ch. 83, John Wiley & Sons, Inc., New York, pp. 991-1024

[7] C. Jensen and J. D. Helsel, *Engineering Drawing and Design,* Glencoe, New York, fourth edition, 1990, pp. 463-464

[8] *Gears and Shaft Accessories Catalog*, Boston Gear, 1996

[9] D. Houser, "Gear Noise", *Dudley's Gear Handbook*, ch. 14, McGraw-Mill, Inc., New York, second edition, 1992, pp. 14.1-14.9,

[10] J. D. Smith, *Gears and Their Vibration*, Marcel Dekker, Inc., New York, 1983, pp. 10-11

[11] J. O. Smith and O.M. Sidebottom, *Elemetary Mechanics of Deformable Bodies*,The Macmillan Company, London, 1969, p. 359

[12] S. H. Crandall, N. C. Dahl, and T. J. Lardner, *An Introduction to the Mechanics of Solids*, McGraw-Mill, Inc., New York, second edition, 1978, p. 316

[13] S. S. Rao, *Mechanical Vibrations*, Addison-Wesley, Reading, Massachusetts, third edition, 1995, pp. 147-155, 201-205, 224

[14] L. E. Kinsler and A. R. Frey, *Fundamentals of Acoustics*, John Wiley & Sons, Inc., New York, second edition, 1962, pp. 125

[15] *Measuring Vibration,* Bruel and Kjaer, 1980

[16] *Electrical Products and Catalog*, Boston Gear, 1995